Few-body physics with ultracold potassium rubidium mixtures

Lars J. Wacker

PhD Thesis

Institute of Physics and Astronomy
Aarhus University

July 2015

Acknowledgments

I would like to take the opportunity to thank a number of people, who have been a great support during the work on this thesis.

First of all I will thank my supervisor Jan Arlt, for giving me the great opportunity to work with him in his group, the guidance during the time and especially for being always enthusiastic about the project.

I would like to thank the whole MIX-team. A special thanks to Nils Winter with whom I spent a lot of time inside and outside the lab and who became a great friend. Nils Byg Jørgensen not only for being the new Nils but especially for a great time. Special acknowledgments have to go to Nils^2, for having to cope with me and my discussions with the laser system, Danny Birkmose having the bad luck of always missing the cool physics moments, Theis Skalmstang for spreading infinite happiness in the lab and Georg Kleine-Bühning and Johannes Will for constructing this great scientific apparatus. Moreover I would like to thank Jacob Sherson for scientific support and many fruitful discussions.

I want to thank Miroslav Gajdacz, who wrote his thesis in parallel and thus was a great help, since he was coping with the same issues at the same time. A special thanks to Grete Flarup for being a pilot in the administrative fog. Moreover a big thanks to all the great people in the world of cold atoms in Aarhus. Probably I would forget one of you, so I will not start to try to name all of you.

Thanks to all the great people I met during my time in Aarhus, especially to Marija for making me a happier person.

Finally a huge thank you to my parents Jutta and Horst and my brother Thies. Your unlimited support was invaluable from long before my first day in school to now and will be in future.

Abstract

Since the first realization of Bose-Einstein condensates in dilute gases, the area of ultracold atomic physics made numerous contributions to many areas in physics. In particular Feshbach resonances allow for the investigation of interaction induced effects in macroscopic quantum systems and heteronuclear quantum gas mixtures enable investigations of e.g. molecular, few and many body physics.

Within the scope of this thesis two Bose-Einstein condensate mixtures with tunable interspecies interactions were realized. The mixture of ^{39}K-^{87}Rb is a novel mixture with tunable inter- and intraspecies interactions. Usually ^{39}K is not considered for the production of heteronuclear Bose-Einstein condensate mixtures, since a magnetic field is required to tune the background scattering length to positive values. However this is circumvented by employing three Feshbach resonances at the same time to realize dual condensates. This mixture features an interspecies Feshbach resonance, which was characterized to high precision, as well as very broad intraspecies resonances in ^{39}K. The control of the interaction between the species was demonstrated by investigating the quantum phase transition from the miscible to the immiscible phase of a condensate mixture. The second Bose-Einstein condensate mixture realized within the scope of this thesis, ^{41}K-^{87}Rb, allows for the precise tuning of the interspecies interaction, due to the availability of a number of broad and narrow resonances and, in combination with the ^{39}K-^{87}Rb mixture, allows for comparative studies.

These two mixtures were used to investigate the three-body problem, one of the outstanding problems in physics. The simplicity of this quantum mechanical few-body problem in combination with the resulting complexity make it a perfect model system to simulate with the two mixtures in this apparatus. One of the best known theoretical outcomes is the Efimov effect, predicting an infinite number of geometrically scaled three-body bound states for interactions where no two body bound state is present. While previous experiments with mixtures of ^{41}K-^{87}Rb observed an Efimov resonance, no resonance was observed in experiments with ^{40}K-^{87}Rb, despite the similarity of the system. We performed loss measurements for the detection of these resonances and no Efimov resonances could be observed for intermediate scattering lengths in both mixtures of ^{39}K-^{87}Rb and ^{41}K-^{87}Rb solving a longstanding controversy in the field of few-body physics.

Resumé

Siden Bose-Einstein-kondensater er blevet realiseret i en sky af atomer, er der blevet lavet talrige bidrag til mange områder i fysikken igennem ultrakolde kvantegasser. I særdeleshed har Feshbach-resonanser åbnet op for undersøgelser af interaktionseffekter i makroskopiske kvantesystemer, og heteronukleare kvantegasblandinger giver mulighed for at studere f.eks. molekylefysik, og kvantefysik med få og mange legemer.

Indenfor denne afhandling, er to blandinger af Bose-Einstein-kondensater med kontrolerbare interaktioner blevet realiseret. ^{39}K-^{87}Rb er en nyskabende blanding hvor interaktionen både kan kontroleres imellem ens og forskellige atomer. Normalt betragtes ^{39}K ikke som en mulighed til blandinger af Bose-Einstein-kondensater, da magnetfeltet er nødvendigt til at gøre spredningslængden positiv. Her udnyttes dog en unik kombination af to Feshbach-resonanser, der giver mulighed for kondensation af begge stoffer, sammen med at en tredje resonans, der giver mulighed for at styre interaktionen imellem stofferne. Denne resonans karakteriseres her til høj præcision, og bruges til at undersøge kvantefaseovergangen imellem den blandbare og ikke-blandbare tilstand. Den anden blanding, ^{41}K-^{87}Rb, giver, med både brede og smalle Feshbach-resonancer, mulighed for præcis kontrol af interaktionen imellem stofferne og i kombination med den første blanding, fås her et velgenet mulighed for at lave studier til sammenligning.

Disse to blandinger bruges til at undersøge trelegemeproblemet, der er et af fysikkens enestående problemer. Kombinationen af enkelthed og kompleksitet i et kvantemekanisk trelegemesystem, gør det et ideelt system at undersøge med de to tilgængelige blandinger. Et af de bedst kendte resultater er Efimov-effekten, der for bestemte interaktioner giver et uendeligt antal geometrisk skallerede, bundne tilstande for tre legemer, uden bundne tilstande for to legemer. I tidligere eksperimenter med blandinger af ^{41}K-^{87}Rb er der blevet observeret en Efimov-resonans, men i andre eksperimenter med ^{40}K-^{87}Rb kunne en sådan resonans ikke observeres, på trods af ligheden imellem systemerne. Igennem tabsmålinger af atomer har vi søgt efter disse resonancer, men ingen Efimov-resonanser blev observeret, hverken i ^{39}K-^{87}Rb eller ^{41}K-^{87}Rb. Dermed løses en vedvarende kontrovers indenfor fysik med få legemer.

Contents

1 Introduction

Atoms and their properties have always played a major role to gain insight into nature. While the Greek philosophers already discussed the concept of discrete units of matter, it was quantum mechanics that allowed for the complete description of atoms and the associated phenomena. In the middle of the 1920s, A. Einstein based on previous work by S. Bose predicted a striking quantum mechanical effect in non-interacting gases [1, 2]. When cooled below a certain temperature, a macroscopic fraction of the atoms will start populating the ground state, an effect now called Bose-Einstein condensation (BEC). Since the first realization in dilute sodium [3] and rubidium [4] vapors in 1995 this new field has made contributions to many areas of physics. The high degree of control of the inner and outer parameters of the samples and the isolation from external influences make BECs a powerful tool to investigate fundamental effects and to simulate quantum systems. One of the outstanding effects occurring in samples of ultra-cold gases are magnetic Feshbach resonances [5], since they allow for precise tuning of the interatomic two-body interaction and thus enable the production of BECs with tunable interactions [6].

Mixed Bose-Einstein condensates

The outlook to produce and investigate BEC mixtures with distinguishable components and tunable interactions triggered considerable interest, since they allow for the investigations of effects in wide scope ranging from molecular physics [7], impurity physics [8–11] and precision metrology [12] to few [13, 14] and many body physics [15].

Various approaches have been used to realize dual species Bose-Bose systems. The most common one uses different spin states of the same isotope [16]. This allowed

e.g. for the realization of spinor quantum gases [17] and the investigation of spin dynamics [18]. Another approach is to use different isotopes of the same element, which had been realized in mixtures of ^{85}Rb-^{87}Rb [19] and ^{168}Yb $-^{174}$ Yb [20] and used for example for observing miscible and immiscible BECs [19].

The approach presented in this theses uses two different atomic species allowing for species dependent trapping and tuning of the intra- and interspecies interaction. This choice allows for a number of investigations including e.g. the production of ground state molecules with a large electric dipole moment [21], tests of the equivalence principle due to different masses [22] or in quantum computation [23]. Typically sympathetic cooling with one atomic species with favorable properties is used for the production of BECs in another species with poor properties for evaporative cooling. This allowed e.g. the production of quantum degenerated Fermi gases [24], since s-wave scattering is forbidden for low temperatures due to the Pauli exclusion principle and thus does not permit evaporative cooling. Employing this technique it was possible to produce the first ^{41}K BECs [25] and further improvement of this technique allowed for the first production of dual-species condensates of ^{41}K-^{87}Rb [26] and for tuning of the interspecies interactions [27]. Since then dual species BECs of ^{87}Rb-^{133}Cs [28, 29], ^{23}Na $-^{87}$ Rb [30], ^{87}Rb-^{84}Sr and ^{87}Rb-^{88}Sr [31] have been realized.

The ability to tune the interactions between the different species with the help of Feshbach resonances make this system extremely interesting. In particular it allows to produce miscible condensates of different mass being a prime model system to test the equivalence principle with BECs allowing for long observation times [12]. The precise control of the two-body interaction allows for the investigation of few body physics in a many body environment, simulating a many body problem, which normally would be impossible to solve analytically [32] or by doping a majority component with a second component simulating the behavior of an impurity under the influence of tunable interactions [8–11]. Moreover interspecies Feshbach resonances allow for the association of loosely bound dimers and thus the study of heteronuclear molecular physics [33].

In the experimental apparatus described in this thesis a new BEC mixture with tunable interactions consisting of ^{39}K and ^{87}Rb was created. ^{39}K is an unusual species for dual species experiments since the magnetic field is needed to tune the background scattering length to positive values. By employing two Feshbach resonances at the same time the condensate was stabilized, while a third resonance was used to tune the interspecies scattering length. This allowed for the investigation of miscible and immiscible quantum phases and the determination of

the interspecies scattering properties with a novel method. Moreover mixtures of ^{41}K and ^{87}Rb have were realized in this apparatus. Since these two mixtures include the same isotope of rubidium and the masses of the potassium atom differ only by a small percentage these are the ideal candidates for experiments in few-body physics.

Few body bound states

The two body problem is one of the standard examples in scattering theory and is well described and understood. The transition from two to few body physics makes the system not only more complicated, but at the same time richer of interesting effects. It was V. Efimov, who realized in 1970 that three identical bosons, that do not support a two body bound state, support an infinite number of bound states, geometrically scaled by a constant factor in size and energy [34]. Although proposed to solve problems in nuclear physics, it turned out to be almost impossible to verify his predictions in nuclei [13].

Confirmation of the existence of this new effect came from the field of ultracold gases in 2006. A sample of ultracold ^{133}Cs showed increased three-body losses for certain interaction strengths, for parameters where no dimer states existed, the so called Borromean region [35]. Later it was moreover possible to provide evidence of an Efimov three-body bound state in non-Borromean regions by measuring the enhanced losses due to inelastic collisions of ^{133}Cs atoms and Feshbach dimers [36] and show the universality between loss maxima and minima on both sides of the Feshbach resonance [37] connected to the same Efimov state. A special interest arose in the investigation of mass imbalanced cases, since this changes the discrete scaling between the different Efimov states [32], which triggered experiments in ^{41}K-^{87}Rb observing both K-K-Rb and Rb-Rb-K resonances [38]. Moreover the effect was also observed in distinguishable Fermi gases [39–43] and the binding energy was determined with the help of RF-spectroscopy [44, 45]. More recently four [46, 47] and five body [48] Efimov like resonances were observed bound to the Efimov three-body resonances.

Demonstrating the discrete scaling between different states turned out to be more difficult. The first attempts showed clear indications only between the loss minima in the non-Borrromean region [47, 49], and it took until 2014 until it was possible to measure the discrete scaling between the first two states [50] and confirm the prediction of the existence of giant Efimov states made 44 years earlier. Work in the extreme mass imbalanced case showed even signs of the second excited resonance

confirming the geometric scaling between the Efimov states [51, 52].

An ongoing discussion concerns the position of the resonances. It turned out, that the position shows a universal relation to the van der Waals length across species [53] and Feshbach resonances [54, 55] in single species experiments. Nonetheless the prediction of the position of the Efimov resonances in the heteronuclear case is still not feasible from theory and has to be found experimentally, thus simulating the quantum mechanical three-body problem.

However the case of potassium and rubidium became inconclusive with the discovery of the absence of Efimov resonances in Bose-Fermi mixtures of ^{40}K-^{87}Rb [56, 57]. This was in contradiction to the earlier observation in ^{41}K-^{87}Rb, since the resonances were expected to be in the same position due to the small mass difference of the potassium atom. These surprisingly different results triggered the investigations of ^{39}K-^{87}Rb and ^{41}K-^{87}Rb mixtures presented in the last part of this theses.

Structure of the thesis

The thesis is structured as follows:

- In chapter two some of the underlying physical principles of interacting single and multi component quantum gases are discussed.
- The experimental apparatus, which was used in this thesis, is introduced in chapter three. Special focus is laid on some of the problems and solutions required for working with two component samples.
- In chapter four the production of ^{39}K BECs with tunable interactions, as well dual species BECs of ^{39}K-^{87}Rb and ^{41}K-^{87}Rb, is presented. The control of the interactions is demonstrated by high precision characterization of a ^{39}K-^{87}Rb Feshbach resonance and the observation and analysis of the quantum state transition from miscible to immiscible BECs.
- Chapter five presents the experimental work on heteronuclear few body physics. In mixtures of ^{39}K-^{87}Rb and ^{41}K-^{87}Rb the scattering length dependent loss coefficient was measured and no sign of observable Efimov resonances at intermediate scattering lengths was detected.

2 Interacting bosonic quantum gases

This chapter focuses on the theoretical background of the experimental work in this thesis. It starts with a description of the interaction of two level atoms with external electro-magnetic fields in section 2.1. Section 2.2 introduces the basic concepts of scattering between two particles and how magnetic Feshbach resonances can be used to manipulate the scattering properties of atoms. The introduced scattering concepts are used in subsection 2.2.2 to describe loss processes in two component samples, which can be used as a tool to detect Efimov resonances, as described in subsection 2.2.3. The chapter is concluded by a description of interacting Bose-Einstein condensates (BEC) with one and two components in section 2.3.

2.1. Two level dressed atom picture

Electromagnetic fields have an immediate effect onto the internal level structure of an atom. They can, for example, be used to manipulate the internal states of the atom as will be described in subsection 2.1.2 and subsection 2.1.3, or for trapping as described in subsection 2.1.1. To model the internal states we introduce the two eigenstates of our two level atom as $|e\rangle$ and $|g\rangle$ driven by an external quantized field to induce a change of the states. The dipole matrix element for a transitions between the two eigenstates for light polarized in the direction of the x-axis can be written as [58]

$$\mu_{ge} = -e\langle g|x|e\rangle, \tag{2.1}$$

with the charge of the electron e. The characteristic frequency connected to the rate at which the states change is defined as the Rabi frequency

$$\Omega_R = |\mu_{ge} E_0 \hbar| \tag{2.2}$$

with E_0 being the electric field amplitude, $\hbar$ the Planck constant. This system is well described by the Jaynes-Cummings model considering it a two level atom in a quantized field. The Hamiltonian of the system can be written as [59]

$$\mathbf{H}_{JC} = \mathbf{H}_a + \mathbf{H}_l + \mathbf{H}_{int}, \tag{2.3}$$

consisting of the Hamiltonian of the atom H_a, of the field H_l and the interaction between field and atom H_{int}. This Hamiltonian describes transitions between $|g\rangle$ and $|e\rangle$ as

$$|e\rangle|n-1\rangle \leftrightarrow |g\rangle|n\rangle, \tag{2.4}$$

with the bare states of the system defined as

$$\begin{aligned} |\psi_{1n}\rangle =& |e\rangle|n\rangle \\ |\psi_{2n}\rangle =& |g\rangle|n+1\rangle. \end{aligned} \tag{2.5}$$

For a detuning ($\Delta = \omega - \omega_0$), with the unperturbed atomic transition frequency ω_0 and the frequency of the light field ω, the Hamiltonian of this system can be expressed as [59]

$$\mathbf{H}^{(n)} = \hbar \begin{bmatrix} n\omega + \frac{\omega_0}{2} & \lambda\sqrt{n+1} \\ \lambda\sqrt{n+1} & (n+1)\omega - \frac{\omega_0}{2} \end{bmatrix}. \tag{2.6}$$

The detuning dependent Rabi frequency is obtained to $\Omega_n(\Delta) = \sqrt{\Delta^2 + 4\lambda^2(n+1)} = \sqrt{\Delta^2 + \Omega_R^2}$, which for zero detuning becomes the unpertubed Rabi frequency $\Omega_n(0) = 2\lambda\sqrt{(n+1)} = \Omega_R$.

2.1.1. Optical dipole trap

A strong laser beam, that is red detuned to an atomic transition, can be used to trap atoms in the intensity maximum. The underlying dipole force can be explained by the coupling of the internal states of the atoms onto the external field. From Equation (2.6) we get the energy eigenvalues as [59]

$$\begin{aligned} E_{(1n)}(\Delta,\mathbf{r}) &= \left(n + \frac{1}{2}\right)\hbar\omega + \frac{1}{2}\hbar\Omega_n(\Delta,\mathbf{r}) \\ E_{(2n)(\Delta,\mathbf{r})} &= \left(n + \frac{1}{2}\right)\hbar\omega - \frac{1}{2}\hbar\Omega_n(\Delta,\mathbf{r}). \end{aligned} \tag{2.7}$$

We assume that the Rabi frequency Ω_n may vary depending on the position in space and the detuning of the driving field. Figure 2.1 shows the general results of the state energy dependence on a position depending intensity, e.g. a Gaussian laser beam. Furthermore the eigenstates $|n,\pm\rangle$ can be written as the dressed states

$$\begin{aligned} |n,+\rangle &= \cos(\Phi_n/2)|\psi_{1n}\rangle + \sin(\Phi_n/2)|\psi_{2n}\rangle \\ |n,-\rangle &= -\sin(\Phi_n/2)|\psi_{1n}\rangle + \cos(\Phi_n/2)|\psi_{2n}\rangle, \end{aligned} \tag{2.8}$$

with $\Phi_n = \arctan\frac{\Omega_R}{\Delta}$. The force on an atom at rest can now be calculated as

$$\mathbf{F}_{dip} = -\Pi_1 \nabla E_1 - \Pi_2 \nabla E_2, \tag{2.9}$$

by calculating the reduced state populations Π. It has been shown that the force on the atoms is [60]

$$\mathbf{F}_{dip} = -\hbar\Delta \frac{\omega^2}{\omega^2 + 2\Delta^2}\boldsymbol{\alpha} = -\nabla\left[\frac{\hbar\Delta}{2}\log\left(1 + \frac{\omega^2}{2\Delta^2}\right)\right], \tag{2.10}$$

with $\boldsymbol{\alpha} = \frac{\nabla\omega}{\omega} = \frac{\Omega_n}{\omega}\nabla\Omega_n$.

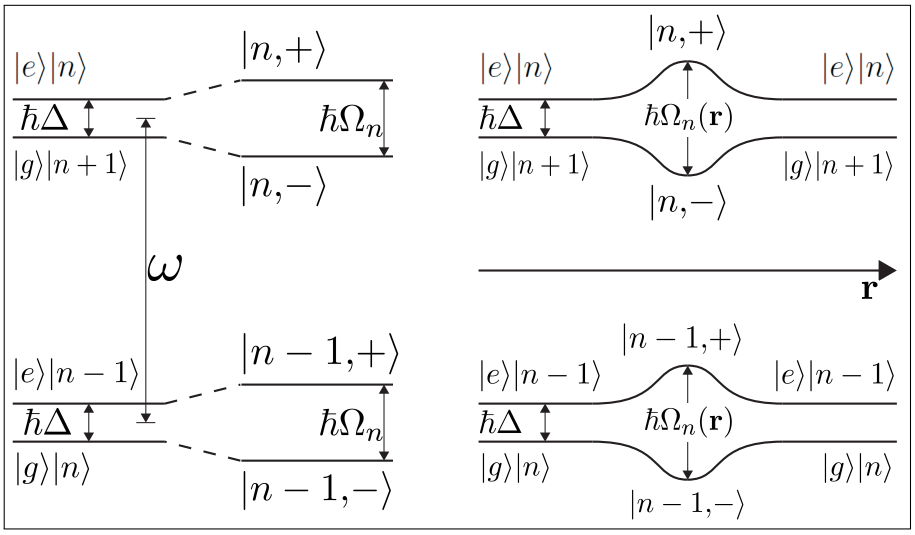

Figure 2.1.: (left) Diagram for the level energy shift from the bare atomic transition without coupling to the dressed states. (right) Dressed level energy shift depending on the intensity variation across a Gaussian laser beam for $\Delta < 0$.

From this it follows that an atom experiences an intensity and detuning dependent force. Assuming a strongly focused laser beam this force attracts atoms in the ground state to the center of the beam for $\Delta < 0$ and repels them for $\Delta > 0$.

2.1.2. Rabi oscillations

Working with cold atomic systems often involves the manipulation of the internal states of an atom. This includes the change of the hyperfine levels as well as the magnetic sub states. Detailed descriptions of the manipulation with resonant or non-resonant time-depending fields can be found in the books of L. Allen and J. H. Eberly [61] or H. Metcalf and P. van der Straten [62]. Assuming an atom is in a driving field, the probability of finding the atom in state $|1\rangle$ and $|2\rangle$ changes in time according to

$$\begin{aligned} |c_1(t)|^2 =& \frac{\Omega_R^2}{\Omega_n^2} \sin^2(\Omega_n t/2) \\ |c_2(t)|^2 =& \frac{\Omega_R^2}{\Omega_n^2} \cos^2(\Omega_n t/2). \end{aligned} \tag{2.11}$$

We assume that the radiation is resonant and thus Equation (2.11) simplifies to

$$\begin{aligned} |c_1(t)|^2 =& \sin^2(\Omega_R t/2) \\ |c_2(t)|^2 =& \cos^2(\Omega_R t/2). \end{aligned} \tag{2.12}$$

It is obvious that the occupation probability of the two states changes in time with the Rabi frequency as illustrated in Figure 2.2. The maximum occupation transfer to the other state is only achieved for a resonant driving field and goes down for a detuning $|\Delta| > 0$. Starting with a system prepared in state $|2\rangle$ at $t = 0$, a pulse with $\Omega_R t$ equal to π fully transfers the population to state $|1\rangle$ and is referred to as a π pulse. Since the first derivative of $|c_1(t)|^2$ at this time is zero the timing is inherently robust to small variations and can be used for controlled state preparation. One of the fundamental issues is the decoherence inherently occurring in experimental systems, leading to the damping of the oscillation as well as a loss in contrast. Experiments improving the coherence times have been previously performed on the apparatus described here [63]. A pulse with half this duration is referred to as a $\pi/2$-pulse and prepares the sample in a superposition of the two states. Though less robust to produce, the superposition of the two states allows for other applications such as inertial sensing [64, 65], optical lattice clocks [66] or to explore fundamental quantum physics [67, 68].

2.1.3. Adiabatic passages

Another way to change the internal state of an atom with high efficiency is to use rapid adiabatic passages. A non resonant field is coupling to two states and

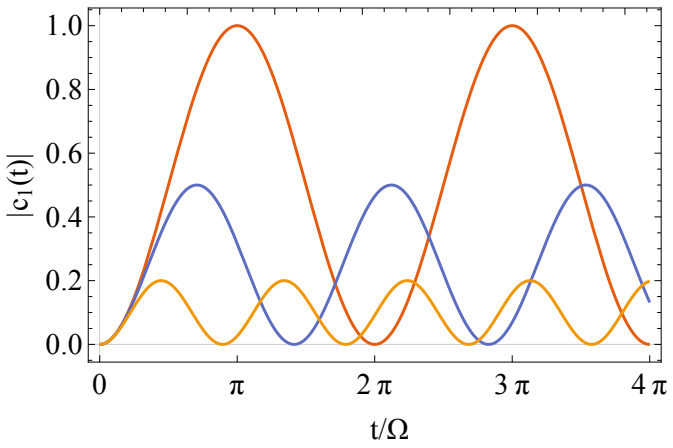

Figure 2.2.: The probability to find an atom in the $|2\rangle$ state after undergoing Rabi oscillations. The driving field is detuned by $\Delta = 0$ (red), $\Delta = \Omega_R$ (blue) and $\Delta = 2\Omega_R$ (orange).

is swept across the resonance. This transfers the atoms from one state into the other. This procedure is normally more robust than π-pulses due to an inherent insensitivity for small deviations in the magnetic field [61].

To transfer the sample from one state to another the process has to be fast compared to the relaxation time of the system T_{dec}. In the same way, the process has to be slow enough for the system to follow the perturbation meaning

$$\frac{\Omega_R}{T_{dec}} << \frac{\partial\omega}{\partial t} << \Omega_R^2. \tag{2.13}$$

We consider the Hamiltonian described in Equation (2.6) with two coupled states $|1\rangle$ and $|2\rangle$ perturbed by an electromagnetic field with frequency ω. The energy diagram of theses states close to resonance is shown in Figure 2.3.

A transfer from state $|1\rangle$ into $|2\rangle$ starts on the left side of the figure. The states are uncoupled and the coupling is applied by the external field ω. The states are almost degenerate and by sweeping the frequency to the right side the resonance the state follows the avoided crossing. The sweep has to fulfill the conditions from Equation (2.13) meaning it has to be rapid compared to the decoherence of the system but the change in frequency has to be slow enough for the system to follow adiabatically. By turning off the perturbing electromagnetic field and thus the coupling, the atom is projected into an eigenstate leading to the transfer of the population into state $|2\rangle$.

An example for such an energy splitting is the Zeeman splitting. In the low-field

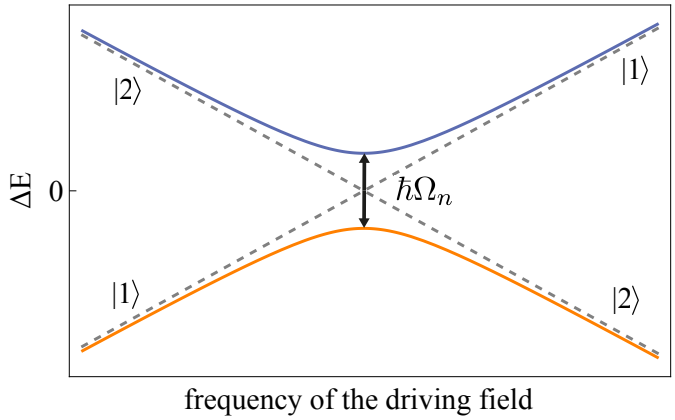

Figure 2.3.: Example for the energy of two dressed states. The uncoupled energies are drawn in dashed lines, while the eigenstates $|1\rangle(|2\rangle)$ for the coupled system are drawn in orange (blue).

region this can be calculated by the Breit-Rabi formula [69]

$$E_B^{HFS}(F = I + -\frac{1}{2}, m_F) = -\frac{A}{4} + m_F g_K \mu_K B \pm \frac{\Delta E_0}{2}\left(1 + \frac{4m_F}{2I+1}x + x^2\right)^{\frac{1}{2}}, \quad (2.14)$$

with

$$x = \frac{g_J \mu_B - g_K \mu_K}{\Delta E_0} B, \quad (2.15)$$

where g_J is the fine structure g-factor, μ_B the Bohr magneton, g_K is the nuclear g-factor, m_F the magnetic substate, I is the nuclear angular momentum, B is the magnetic field strength and $\Delta E_0 = A(I + \frac{1}{2})$ is the hyperfine splitting at zero field. The relevant constants for potassium and rubidium can be found in references [70, 71].

2.2. Scattering in ultracold gases

For scattering in ultracold gases, the wave nature of the particles and their species has to be taken into account. We consider a two body scattering problem of an incoming and a stationary atom with masses m and the total kinetic energy of $E_{kin} = \hbar^2 k^2/m$, where k denotes the wave number. The scattering problem is described by the Schrödinger equation

$$\left[\frac{\mathbf{p}^2}{2m} + V(r)\right]\varphi(\mathbf{r}) = E\varphi(\mathbf{r}), \quad (2.16)$$

assuming

$$\varphi(\mathbf{r}) = \varphi_0(\mathbf{r}) + \varphi_s(\mathbf{r}), \tag{2.17}$$

for $E > 0$ and a spherical-symmetric scattering potential [72]. The incoming wave

$$\varphi_0(\mathbf{r}) = e^{ikz}, \tag{2.18}$$

is assumed to be a plane wave in the z-direction generating a scattered wave $\varphi_s(\mathbf{r})$. For the case of $r \to \infty$ the outgoing wave can be described as a spherical wave

$$\varphi_s(\mathbf{r}) \xrightarrow[r\to\infty]{} f(\theta)\frac{e^{ikr}}{r}, \tag{2.19}$$

with scattering amplitude $f_k(\theta)$ depending on the angle θ. The differential scattering cross section is defined as

$$\frac{d\sigma}{d\Omega} = |f_k(\theta)|^2, \tag{2.20}$$

for the case of two distinguishable atoms [73]. The elastic cross section σ can be obtained by integrating over all solid angles

$$\sigma = \oint_{4\pi} \frac{d\sigma}{d\Omega} d\Omega. \tag{2.21}$$

Assuming azimuthal symmetry and using a partial-wave expansion the scattering amplitude can be written as

$$f_k(\theta) = \sum_{L=0}^{\infty} \frac{2L+1}{k\cot\delta(k) - ik} P_L(\cos\theta), \tag{2.22}$$

by expanding the scattering amplitude f_k in terms of the Legendre polynomials P_L, the scattering phase shift $\delta(k)$ and the angular momentum quantum number L [73, 74].

Assuming the low energy regime with $k \to 0$ and $L = 0$, the scattering length a is well approximated by

$$k\cot\delta(k) = -\frac{1}{a} + 1/2 r_0 k^2, \tag{2.23}$$

with the s-wave effective range r_0 [75]. Since only scattering with $L = 0$ is considered, this type of scattering is referred to as s-wave scattering, following the naming scheme for atomic orbitals.

The scattering cross section in terms of the scattering length is given by

$$\sigma \cong 4\pi a^2. \tag{2.24}$$

In the case of two indistinguishable bosons the scattering cross section will be larger by a factor 2, while it vanishes for identical fermions [75].

The van-der Waals range

The interatomic potential can be well described by the Lennard-Jones potential [76] as

$$V(r) = \epsilon \left[\left(\frac{C_{12}}{r} \right)^{12} - \left(\frac{C_6}{r} \right)^{6} \right]. \tag{2.25}$$

It consists of a strong repulsive component determined by the C_{12} coefficient and the long range tail determined by the C_6 coefficient, while ϵ describes the depth of the potential well. The length scale connected to the C_6 coefficient is the van der Waals radius

$$R_{vdW} = \frac{1}{2} \left(\frac{2\mu C_6}{\hbar^2} \right)^{1/4}, \tag{2.26}$$

with the reduced mass μ of the two atoms. The van der Waals length $l_{vdW} = 2R_{vdW}$ defines the length scale at which interactions between atoms for small energies take place and thus defines an important boundary. Values for the C_6 coefficient in potassium and rubidium mixtures have been determined by Simoni et al.[77]. Assuming a very low energy scale, the thermal de-Broigle wavelength from Equation (2.57) might become larger than the spacial extend of the potential. In this case it will be impossible to resolve the internal structure of the two atoms by scattering [73]. By exploiting Feshbach resonances, as described in subsection 2.2.1, one can tune the scattering length a to larger values than l_{vdW} and thus make the scattering independent from the internal structure of atoms.

The alkali atoms used in this thesis have van-der Waals lengths of about $65\,a_0$ in potassium [70], about $83\,a_0$ in ^{87}Rb [78] and about $72\,a_0$ between potassium and rubidium [77, 79], with a_0 being the Bohr radius.

2.2.1. Magnetic Feshbach resonances

From the first observation of magnetic Feshbach resonances in atomic clouds by Inouye et al. [6] in 1998, it has evolved to a versatile tool in ultracold quantum gases. Besides changing the scattering length this effect can also be used for the association of weakly bound molecules. A basic explanation is given here, while a detailed treatment of this extensive topic can be found in C. Chin et al. [79].

Assuming the interatomic potential V_0 as shown in Figure 2.4, which for large distances approaches the potential for two unbound atoms. This 'open channel' does not support any bound states for the incoming atom with energy E_s. Note that scattering in ultracold atoms takes place close to $E_s \to 0$. Another molecular potential V_c close to the open channel shall support bound states and is thus called

'closed channel'. The relative energy difference between the two channels is tunable with an external magnetic field. A Feshbach resonance arises when a bound state in the closed channel with energy E_c energetically approaches the scattering state with energy E_s in the open channel. In this case strong mixing between the states take place leading to a shift in the scattering phase. As shown in Equation (2.23) a change in δ is equivalent to a change in the scattering length, which can in return be controlled by the magnetic field.

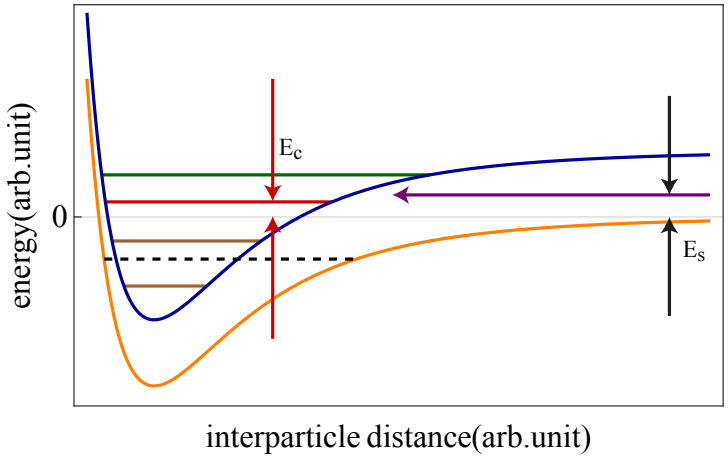

Figure 2.4.: Simple two channel picture of a Feshbach resonance. Depicted are the open channel $V_o(r)$ (orange) and the closed channel $V_c(r)$ (blue) potential. The horizontal arrow depicts the incoming state with the energy E_s (purple) and possible bound states for the open channel (dashed) and the closed channel (brown and green). Possible coupling can happen to a bound state with similar energy E_c as the incoming particle (red).

Close to the resonances the asymptotic behavior of the scattering length can be approximated by

$$a(B) = a_{ab}\left(1 - \frac{\Delta}{B - B_0}\right), \tag{2.27}$$

and for multiple overlapping Feshbach resonances by

$$a(B) = a_{ab}\left(1 - \sum_{n=1}^{i} \frac{\Delta_i}{B - B_{0,i}}\right), \tag{2.28}$$

while a_{bg} is the background scattering length, B the magnetic field strength, B_0

the magnetic field at the resonance center and Δ the width of the resonance [80]. An example for this dispersive behavior is shown in figure 2.5.

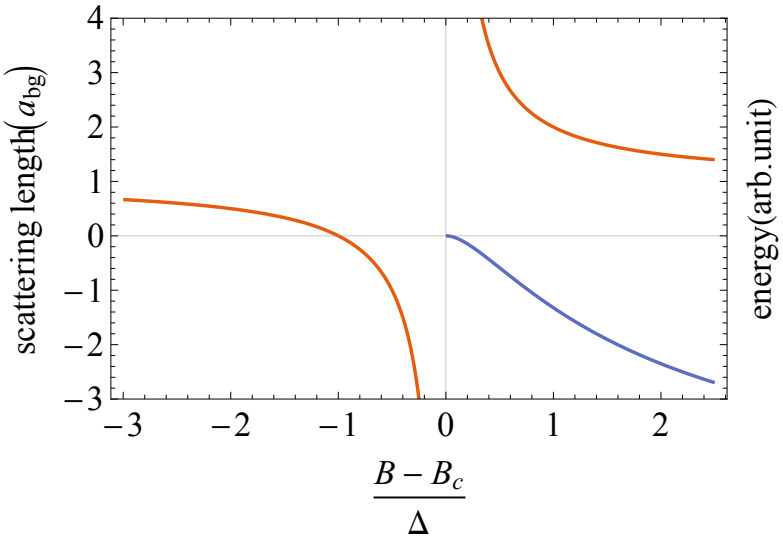

Figure 2.5.: Example of the magnetic field dependent scattering length from Equation (2.27) (red) and the associated dimer state from Equation depending on the magnetic field (2.29) (blue).

Dimer states

The presence of another state with possible bound states is leads to the existence of a weakly bound dimer state on the positive side of a Feshbach resonance. The binding energy close to the resonance can be calculated using

$$E_D = \frac{\hbar^2}{2\mu a^2}, \tag{2.29}$$

with μ denoting the reduced mass [79]. The corresponding molecular level is shown in Figure 2.5. This makes it possible to associate molecules by e.g. magnetic field sweeps [81, 82] or radio frequency association [83, 84]. These molecules are weakly bound and in a highly excited state. Different techniques have been developed to transfer them into the absolute ro-vibrational ground state [85, 86]. Since recombination into the bound state is energetically possible for two atoms, this state also adds another loss channel not present on the side of negative scattering length.

Resonance strength

To characterize the nature of different Feshbach resonances further, Gribakin and Flambaum introduced the mean scattering length

$$\bar{a} = \frac{4\pi}{\Gamma(\frac{1}{4})^2} R_{vdW} = 0.955978... R_{vdW}, \tag{2.30}$$

with Γ defined as the gamma function [87]. The corresponding energy scale [79] is given by

$$\bar{E} = \frac{\hbar^2}{2\mu\bar{a}}. \tag{2.31}$$

This allows to set the magnetic width of the resonance in relation to the potential width and thus to define the resonance strength parameter

$$s_{res} = \frac{a_{bg}}{\bar{a}} \frac{\delta\mu\Delta}{\bar{E}}, \tag{2.32}$$

with $\delta\mu$ the differential magnetic moment between the separate atoms and the bound state. This dimensionless parameter can be used to characterize the resonance [79, 88, 89]. For $s_{res} >> 1$ the resonance is considered as an open channel dominated resonance, where the near threshold scattering and spin character are dominated by the entrance channel. The scattering properties are very well described by Equation (2.28). For the case of $s_{res} << 1$ the resonance is dominated by the properties of the closed channel. The modeling of the interaction can be more complicated and a coupled channel analysis can be in place [79]. Sometimes the open channel dominated resonances are referred to as "broad" resonances and vice versa the closed channel dominated as "narrow" resonances, although this strictly speaking refers to the magnetic width Δ.

2.2.2. Losses in scattering

One of the fundamental processes in ultracold gases is scattering between two particles. It is mostly motivated to be elastic, as it is a fundamental part of rethermalization and hence in evaporative and sympathetic cooling. Only a favorable ratio of elastic to inelastic collision opens a "BEC-window" [90] allowing the production of Bose-Einstein condensates in dilute gases. The occurrence of inelastic scattering leads in most cases to heating and atom losses from the trap. These are relatively simple to determine at the end of the experiment and hence

are a good to measure. For a single species system the time dependent losses can be described by [79]

$$\dot{N}(t) = -\frac{N(t)}{\tau} - \int [\alpha_2 n^2(\mathbf{r},t) + \alpha_3 n^3(\mathbf{r},t)] d^3r, \tag{2.33}$$

with the system dependend loss coefficients α for two and three-body processes, the one body lifetime τ and the time and position dependent densities $n(\mathbf{r},t)$.

The one body processes described by the first term can be mainly appointed to collisions with the background gas or for example absorption of photons from a dipole trap beam. The two and three-body processes on the other hand are sample dependent.

Two body losses

The second term in Equation (2.33) describes two body losses. They often involve very unlikely processes, e.g. atoms not in the absolute magnetic ground state, like the $|1,-1\rangle$ state, decaying into lower lying m_F-states. The occurrence of this process in polarized samples is small as it involves a spin changing collision but at the same time a conservation of spin, i.e. a change of the total m_F. Differing from one body processes the two body loss coefficient α_2 is proportional to the scattering length as $\alpha_2 \propto a^2$ as shown in Equation (2.24) for the scattering cross section [55].

Three-body losses

The event of three-body recombination can be understood as a two body scattering event which has to scatter another particle. It follows, that the rate of this process must be proportional to the cube of the atom density. It was shown [91], that the general loss of this process follows an a^4 dependence as

$$\alpha_3(a) = C\frac{\hbar a^4}{m}, \tag{2.34}$$

where C is a dimensionless factor depending on the system and α_3 is the three-body loss coefficient. Often these events form a molecule of two atoms, while most of the kinetic energy is carried away by the third atom, which might be lost from the trap. The molecule might decay into more deeply bound states and by this release the binding energy in form of kinetic energy, which leads to further losses.

The dual species case

By changing the one species case described in Equation (2.33) to a two species case all possible combinations have to be considered. The different combinations can have largely differing recombination probabilities and are characterized by different ratios in the number of lost atoms from each species. This may be caused by e.g. more likely molecule formation in some of the combinations. Since all of the three-body events are expected to follow Equation (2.34), their dependence is expected to be proportional to a^4. Due to their low probability we neglect two-body losses and hence the dual species case is described by the coupled differential equations

$$\begin{aligned}
\dot{N}_a = &-\frac{2}{3}\alpha_{baa}\int n_b n_a^2 \mathrm{d}^3r \\
&-\frac{1}{3}\alpha_{bba}\int n_b^2 n_a \mathrm{d}^3r \\
&-\alpha_{aaa}\int n_a^3 \mathrm{d}^3r \\
&-\frac{1}{\tau}\int n_a \mathrm{d}^3r, \qquad (2.35)\\
\dot{N}_b = &-\frac{1}{3}\alpha_{baa}\int n_b n_a^2 \mathrm{d}^3r \\
&-\frac{2}{3}\alpha_{bba}\int n_b^2 n_a \mathrm{d}^3r \\
&-\alpha_{bbb}\int n_b^3 \mathrm{d}^3r \\
&-\frac{1}{\tau}\int n_b \mathrm{d}^3r. \qquad (2.36)
\end{aligned}$$

Heating effects of three-body recombinations

Besides atom loss, three-body processes involve two heating mechanisms. The density dependence in Equation (2.33) and Equation (2.36) lead to higher losses in regions with higher densities, corresponding to positions of lower energy. This leads to a loss of colder atoms or "anti"-evaporation. As described in subsection 2.2.1 for positive scattering lengths a molecular bound state exists, which products might remain trapped. When the binding energy is released, the sample might be heated by this process. This process turned out to be neglectable as it is of almost no relevance [49].

Looking at a single species sample, the mean kinetic energy U of a lost atom is

$$\frac{\int n^3 U d^3r}{\int n^3 d^3r} = \frac{1}{2} k_B T, \tag{2.37}$$

with k_B being the Boltzmann constant. The average kinetic energy of an atom in the sample is $\frac{3}{2}k_B T$, leading to an excess heat corresponding to $1k_B T$ per lost atom [91]. The total energy of the atoms in the sample is on average $3k_B T$. Using the three-body rate from Equation (2.33), the change in temperature can be obtained as

$$\dot{T} = \frac{\alpha T}{3N} \int n^3 d^3r. \tag{2.38}$$

Considering a two component process characterized by α_{aab}, the mean potential energy for an atom lost in an a-a-b recombination is $\beta_{aab} = \frac{2}{3}\beta_a + \frac{1}{3}\beta_b$, with the corresponding species potential energies

$$\beta_a = \frac{\int n_a^2 n_b U d^3r}{\int n_a^2 n_b d^3r} \quad \text{and} \quad \beta_b = \frac{\int n_b^2 n_a U d^3r}{\int n_b^2 n_a d^3r}. \tag{2.39}$$

The average total excess energy is then given by $\frac{3}{2}k_B T - \beta_{aab}$. Comparing to the total average energy of $3k_B T$ of a sample with a total number of atoms $N_a + N_b$, the change in temperature becomes

$$\dot{T} = \alpha_{aab} \frac{\frac{3}{2}k_\mathrm{B} T - \beta_{aab}}{3k_\mathrm{B}} \frac{\int n_a^2 n_b \mathrm{d}^3 r}{N_a + N_b}. \tag{2.40}$$

The different strengths of the combinations described in Equations (2.36) have a major effect on the decay and will be covered for our case of K-Rb in chapter 5.

2.2.3. Efimov effect

Though two bosonic particles may not feature a bound state in a certain set of parameters, adding a third particle might give rise to a possible bound state. V. Efimov realized that this is not only the case for one state, but for an infinite number of states, all scaled by the same factor [34]. This is illustrated in Figure 2.6 for the first three states. These sates are most easily detected by measuring the three-body recombination. We consider the region with negative scattering length as the Borromean region, as it does not provide a two body bound state. The first trimer state (red) approaches the continuum at a characteristic scattering length $a_-^{(0)}$ and gives rise to a peak in the three-body recombination coefficient. The position of the next trimer state is scaled by a factor $e^{\frac{\pi}{s_0}}$ for the resonance

position. For identical bosons this factor is ≈ 22.7, but can vary due to mass scaling. The trimer states cross the unitary region with an energy scaling of $e^{\frac{2\pi}{s_0}}$. On the positive side the states are limited by the dimer state, leading to an atom dimer resonances (a_*) and recombination minima (a_+) [32] in the scattering dependent three-body coefficient.

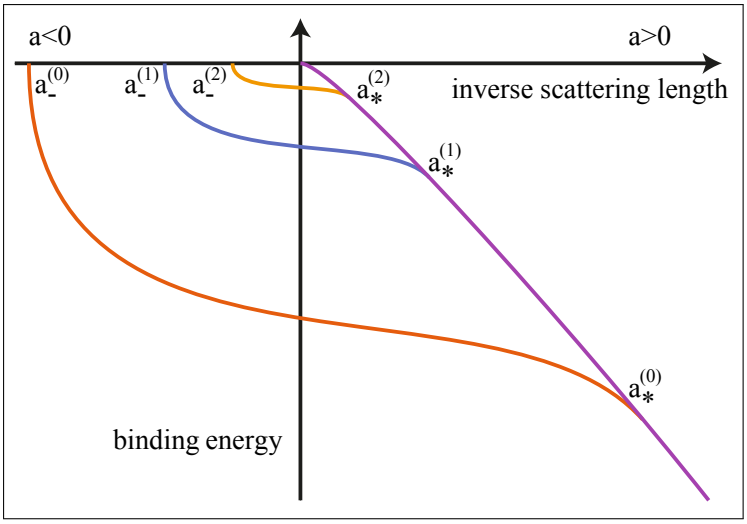

Figure 2.6.: Drawing of possible Efimov states around the pole of a Feshbach resonance at $1/a = 0$ approaching $E = 0$ and the dimer state (purple). The positions of the Efimov resonances a_- and the Efimov dimer resonances a_* are marked. For illustrative purposes the distance between the states is not to scale.

Hyperspherical coordinates

The universality of three-body physics is most easily understood in terms of the hyper-spherical formalism. The following arguments concerning Efimov resonances have been given in [32, 73] with excepts from [92] for the hyper spherical formalism.

The main problem in three-body physics is to solve three-body Schrödinger equation

$$\left(-\frac{\hbar^2}{m}\sum_{i=1}^{3}\nabla_i^2 + V(\mathbf{r}_1,\mathbf{r}_2,\mathbf{r}_3)\right)\Psi = E\Psi. \tag{2.41}$$

To consider an N body problem Jacobi-coordinates can be used. In the case of

three particles we use

$$\mathbf{r}_{ij} = \frac{1}{\sqrt{2}}(\mathbf{r}_i - \mathbf{r}_j), \quad \mathbf{r}_{k,ij} = \sqrt{\frac{2}{3}}(\mathbf{r}_k - \frac{1}{2}(\mathbf{r}_i + \mathbf{r}_j)). \tag{2.42}$$

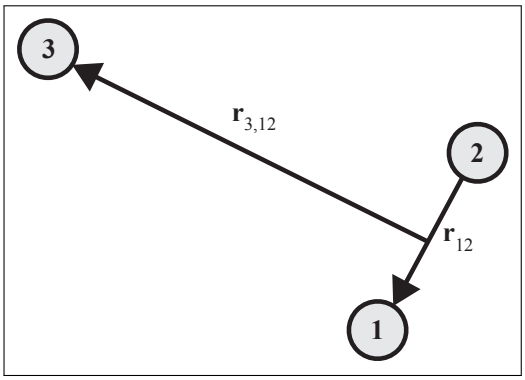

Figure 2.7.: A possible set of Jacobi coordinates defined by Equation (2.42).

The hyperradius R is defined as the root-mean-square separation of the three particles

$$R^2 = \frac{1}{3}(r_{12}^2 + r_{23}^2 + r_{31}^2) = |\mathbf{r}_{ij}|^2 + |\mathbf{r}_{k,ij}|^2. \tag{2.43}$$

If the particles are close together, the hyperradius is small, while it becomes large if one of the atoms is far from the other two. We define the Delves hyperangle [93] α_K as

$$\alpha_k = \arctan\left(\frac{|\mathbf{r}_{ij}|}{|\mathbf{r}_{k,ij}|}\right), \tag{2.44}$$

with (i, j, k) being a permutation of $(1, 2, 3)$. The hyperangle α_k has a range of 0 to $\frac{\pi}{2}$. When atom k is close to the atoms i and j the angle is close to $\frac{\pi}{2}$ and close to 0 when it is far away as shown in Figure 2.8. Thus the magnitudes of the separation vectors $\mathbf{r}_{k,ij}$ and $\mathbf{r}_{ij}$ are

$$\mathbf{r}_{ij} = R\sin\alpha_k, \quad \mathbf{r}_{k,ij} = R\cos\alpha_k. \tag{2.45}$$

The wavefunction can be expressed by using the hyperspherical expansion [94]. For every value of R the wavefuction can be expanded into a complete set of functions of the hyperangles Ω to

$$\psi\,(R,\alpha) = \frac{1}{R^{5/2}}\sum_n f_n(R)\phi_n(R,\Omega). \tag{2.46}$$

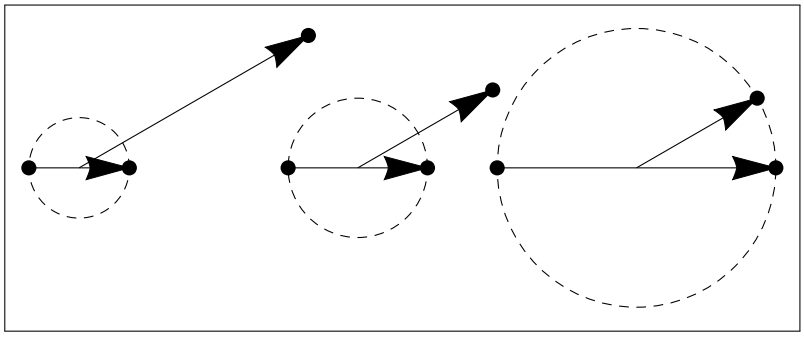

Figure 2.8.: Three examples for different hyperangles, while keeping the hyperradius contstant.

$\phi_n(R,\Omega)$ are solutions to the hyperangular equation [92]

$$\left(\Lambda + \frac{2mR^2}{\hbar^2}V_n\right)\phi_n(R,\Omega) = \lambda_n(R)\phi_n(R,\Omega), \tag{2.47}$$

where Λ denotes the grand angular momentum operator in hyperradial coordinates and λ_n the eigenvalue.

The hyperradial wavefunctions $f_n(R)$ defined in Equation (2.46) fulfill an infinite set of coupled differential equations. Applying the adiabatic hyperspherical approximation [95], the coupling terms are neglected and the equations decouple. They reduce to the independent hyperradial equations

$$\left[\frac{\hbar^2}{2m}\left(-\frac{\partial^2}{\partial R^2} + \frac{15}{4R^2}\right) + V_n(R)\right] f_n(R) \approx E f_n(R), \tag{2.48}$$

for every one of the hyperspherical potentials.

The channel potentials for the hyperradial variable

$$V_n(R) = [\lambda_n(R) - 4]\frac{\hbar^2}{2mR^2}, \tag{2.49}$$

are defined by the eigenvalues $\lambda_n(R)$. To find f_n the hyperradial wave equation is defined as [96]

$$\left(-\frac{\partial^2}{\partial R^2} + \frac{\nu^2(R) - \frac{1}{4}}{R^2} - \frac{2mE}{\hbar^2}\right) f_n(R) = 0, \tag{2.50}$$

where ν is a function of the hyperradius R. The solving of this problem is described in [92]. For three identical Bosons the solution is [97, 98]

$$\nu\cos\left(\frac{\nu\pi}{2}\right) - \frac{8}{\sqrt{3}}\sin\left(\frac{\nu\pi}{6}\right) = \sqrt{2}\frac{R}{a}\sin\left(\frac{\nu\pi}{2}\right), \tag{2.51}$$

where a the interparticle scattering length. The calculations for one distinguishable and two identical particles can be found in [99]. Assuming the extreme case of $a \to \infty$ the imaginary solutions of $\nu = \nu_0$ become independent of R and the radial equation of Equation (2.50) has infinitely many solutions, that are related by

$$\frac{E_{n+1}}{E_n} = e^{-2\pi/|\nu_0|} \equiv \frac{1}{s_0^2}, \tag{2.52}$$

which is also referred to as the Efimov scaling. An example can be seen in Figure 2.6, where the energies of the different Efimov states scale with a constant ratio.

Mass dependend scaling

The number ν_0 is a system dependent constant. A more common value is the scaling of the relative positions in scattering length of the Efimov resonances denoted here with s_0. For identical bosons this value is $s_0 = 22.7$. By choosing a dual species mixture with mass imbalance this ratio changes [32]. Some exemplary values are given in Table 2.1. While the combination of two rubidium and one potassium atom has an unfortunate scaling of > 100, the case of two potassium and one rubidium atom is even more unfavorable. Recent experiments on extreme mass imbalanced mixtures of ^{7}Li-^{133}Cs were able to make use of a more favorable scaling and resolve higher excited Efimov states [51, 52].

system	s_0	$e^{(\pi/s_0)}$
3 identical bosons	1.00624	22.7
^{39}K^{39}K^{87}Rb	≈ 0.2358	$\approx 613\,000$
^{39}K^{87}Rb^{87}Rb	≈ 0.670	$\approx$109
^{40}K^{87}Rb^{87}Rb	0.6536	122.7
^{41}K^{87}Rb^{87}Rb	0.644	131.0
^{41}K^{41}K^{87}Rb	0.2462	348 000
^{7}Li^{133}Cs^{133}Cs	1.850	5.465

Table 2.1.: Efimov scaling factors for different three-body systems. Precise values are adopted from [97]. Values for the ^{39}K-^{87}Rb system have been estimated from [32].

Optical potential

To describe a three component scattering event, one strives to achieve all information about the incoming as well as the outcoming states. The main interest of the work in chapter 5 is to explain losses, since the outgoing states cannot be detected and thus the details of the outgoing channels are not relevant. The model described here makes use of this simplification and takes only absorption processes into account such as light in an optical medium and thus cannot provide information about the products of the recombination. It was proposed by collaborators for three-body recombination in hetero-nuclear systems [99] and will be used to analyze the data in chapter 5.

Starting from Equation (2.50) for negative scattering lengths the potential is defined as

$$V(R) = \frac{\nu^2(R) - \frac{1}{4}}{R^2}, \tag{2.53}$$

which is illustrated in Figure 2.9. A barrier region shields the short distance attractive region from incoming particles. For short distances an imaginary part is added to account for particle loss, which is caused by a loss of probability modeling e.g. absorption processes.

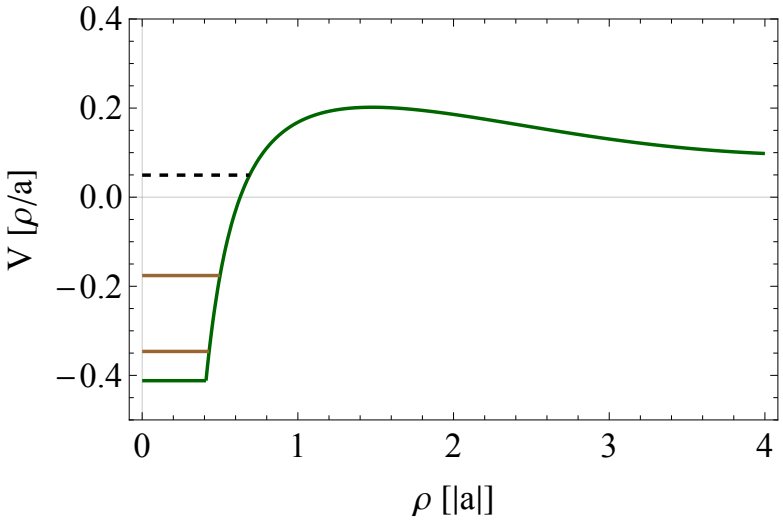

Figure 2.9.: Illustration of the real part of the optical potential defined in Equation (2.54). The brown lines correspond to some possible bound state while the dotted line corresponds to a resonant state for positive energy.

By introducing the imaginary potential V_{imag} and the cut off radius R_{cut} the

potential becomes

$$\frac{2m}{\hbar^2}V(R) = \begin{cases} \dfrac{\nu^2(R) - \frac{1}{4}}{R^2} & \text{if } R > R_{cut} \\ \dfrac{\nu^2(R) - \frac{1}{4}}{R^2} - V_{imag} \cdot i & \text{if } R < R_{cut}. \end{cases} \tag{2.54}$$

The resulting potential is characterized by the barrier around $R/a = 1.46$ going over into a decreasing potential as $15/(4R^2)$ for long distances and the short range attractive region similar to a complex square well. Within the square well a number of bound states exist, which scale through Equation (2.52). When one of these states is equal to the total energy of the three particles the tunnel probability is enhanced and thus the absorption probability. The according negative scattering length for such resonant behavior can be associated with the observable position of a scattering dependent loss maximum as a_- [99].

Detection of Efimov resonances

In subsection 2.2.2 the different loss processes occurring in an ultracold gas due to collisions have been introduced. In this section the focus will lie on three-body losses due to the three-body nature of the Efimov effect. The general scattering length dependence of the loss coefficient is a^4. This is illustrated as red lines in Figure 2.10. The resonant behavior of the Efimov effect at certain scattering lengths adds observable features. The expression for these have been calculated using effective field theory to be [97]

$$\alpha_{122}(a) = \begin{cases} C_\alpha \left(\dfrac{\sin^2[s_0 \ln[a/a_+]] + \sinh^2[\eta_*] \sinh[\eta_*]}{\sinh^2[\pi s_0 + \eta_*] + \cos^2[[s_0 \ln[a/a_+]]} \right. \\ \left. + \dfrac{\coth[\pi s_0] \cosh[\eta_*] \sinh[\eta_*]}{\sinh^2[\pi s_0 + \eta_*] + \cos^2[[s_0 \ln[a/a_+]]} \right) \dfrac{\hbar^2 a^4}{m_1} & \text{if } a > 0 \\ \dfrac{C_\alpha}{2} \dfrac{\coth[\pi s_0] sinh[2\eta_*]}{\sin^2[s_0 \ln[a/a_-]] + \sinh^2[\eta_*]} \dfrac{\hbar^2 a^4}{m_1} & \text{if } a < 0, \end{cases} \tag{2.55}$$

with m_1 being the mass of the minor component denoted by 1 and η_* as a constant related to the lifetime of the Efimov trimer. An exemplary spectrum is plotted in Figure 2.10. The side of negative scattering length shows the characteristic loss peaks at the resonance positions a_-. On the side of positive scattering length a spectrum of recombination minima a_+ can be seen. Since a gas of ultracold atoms is considered here, the corresponding peaks for the atom dimer resonances a_* would

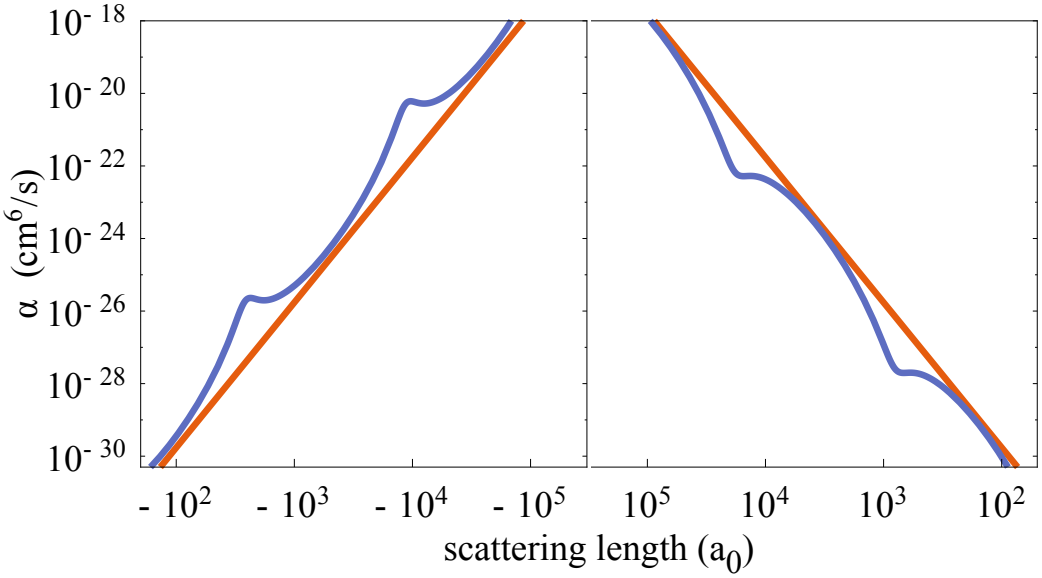

Figure 2.10.: Illustration for a possible Efimov spectrum according to Equation (2.55) in blue and the expected a^4 dependence in the absence of Efimov resonances.

be either non existend or very small and have thus been neglected. In a mixture of dimers and atoms they would show up as prominent loss peaks between the different loss minima on the side of positive scattering length.

2.3. Bosonic atomic gases near zero temperature

A classical gas at high temperatures can be well described by the Maxwel-Boltzman distribution given the average number of particles n of the i-th energy state ϵ_i as

$$n(\epsilon_i) = \frac{1}{e^{(\epsilon_i - \mu)/k_B T}}, \tag{2.56}$$

with the temperature of the gas T and the Boltzmann constant k_B. The chemical potential μ is considered to be well below the particle energy. The quantum statistics of the particles are not significant at higher temperatures. These become relevant when the thermal de Broglie wavelength, given by

$$\lambda_{dB} = \frac{2\pi\hbar}{\sqrt{3mk_B T}}, \tag{2.57}$$

becomes comparable with the interparticle spacing [58].

2.3.1. The ideal Bose gas

For a gas of indistinguishable non-interacting bosons in thermal equilibrium the average number of atoms in every state ϵ_i is given by the Bose-Einstein distribution [100]

$$n(\epsilon_i) = \frac{1}{e^{(\epsilon_i - \mu)/k_B T} - 1}. \tag{2.58}$$

For atoms trapped in a harmonic potential of the form

$$V(\mathbf{r}) = \frac{1}{2} m(\omega_x^2 x^2 + \omega_y^2 y^2 + \omega_z^2 z^2), \tag{2.59}$$

with the trapping frequencies ω, the corresponding energy levels are given by

$$\epsilon(n_x,n_y,n_z) = (n_x + \frac{1}{2})\hbar\omega_x + (n_y + \frac{1}{2})\hbar\omega_y + (n_z + \frac{1}{2})\hbar\omega_z. \tag{2.60}$$

Here n_i are positive integer numbers greater or equal zero. The density of states for this system is given by

$$g(\epsilon) = \frac{\epsilon^2}{2\hbar^3 \omega_x \omega_y \omega_z}. \tag{2.61}$$

In terms of thermodynamical properties this can be written in the form

$$g(\epsilon) = C_\alpha \epsilon^{\alpha - 1}, \tag{2.62}$$

where the coefficient C_α is defined as $C_3 = \frac{1}{2\hbar^3 \omega_x \omega_y \omega_z}$ with $\alpha = 3$ for a harmonic trap. We define the average trapping frequency $\bar{\omega} = (\omega_x \omega_y \omega_z)^{1/3}$ as the geometric mean of the three trapping frequencies. For a large number of non-interacting particles N and low temperatures a good assumption is $\mu \to 0$. We define the critical temperature T_c as the temperature at which the ground state becomes macroscopically occupied. The number of particles in excited states at this temperature is determined by

$$N_{ex}(T_c, \mu = 0) = \int_0^\infty g(\epsilon) n(\epsilon) d\epsilon = \int_0^\infty g(\epsilon) \frac{1}{e^{\epsilon/(k_B T_c) - 1}} d\epsilon, \tag{2.63}$$

which in terms of Equation (2.62) becomes

$$N_{ex} = C_\alpha (k_B T_c)^\alpha \int_0^\infty dx \frac{x^{\alpha - 1}}{e^x - 1} = C_\alpha \Gamma(\alpha) \zeta(\alpha) (k_B T_c)^\alpha. \tag{2.64}$$

Here we make the replacement $x = \epsilon / k_B T_c$, $\Gamma(\alpha)$ for the gamma function and $\zeta(\alpha)$ for the Riemann zeta function. From Equation (2.64) one obtains the value of the critical temperature as

$$k_B T_c = \frac{N^{1/\alpha}}{[C_\alpha \Gamma(\alpha) \zeta(\alpha)]^{1/\alpha}}. \tag{2.65}$$

Since for $\alpha = 3$ the Riemann zeta function is $\Gamma(3) = 1.202$ and the gamma function is $\zeta(3) = 2$ one obtains for the critical temperature the expression

$$k_B T_c = \frac{\hbar\bar{\omega} N^{1/3}}{[\zeta(3)]^{1/3}} \approx 0.94\hbar\bar{\omega} N^{1/3}. \tag{2.66}$$

Another useful quantity derived from the de Broglie wavelength and the atomic density is the phase-space density (PSD)

$$\rho = \frac{N}{V}\lambda_{dB}^3 = n\left(\frac{2\pi\hbar^2}{m k_B T}\right)^{3/2}. \tag{2.67}$$

It is a measure of the overlap of the single particle wavefunctions in the trap. Bose-Einstein condensation occurs when the condition $\rho \geq \zeta(\alpha)$ fulfilled. In a harmonic potential this is the case for $\zeta(3) = 1.202$ and for bosons in a uniform potential for $\zeta(3/2) = 2.612$ [100].

2.3.2. The Gross-Pitaevskii equation

While the statistical description of the non-interacting Bose gas in the previous section makes it possible to predict many effects, e.g. the occurrence of a phase transition to a Bose-Einstein condensate, it does not take into account the interactions between the particles in the ground state and the implications arising from this.

We consider N interacting bosons within an external potential $V_{ext}(\mathbf{r})$ with a point like contact interaction described by the interaction strength g and the Dirac delta function $\delta(\mathbf{r}_i - \mathbf{r}_j)$. Defining the boson field creation and annihilation operators with $\hat{\Psi}$ and $\hat{\Psi}^\dagger$ respectively, the many body Hamiltonian is [101]

$$H = \int d\mathbf{r}\hat{\Psi}^\dagger(\mathbf{r})\left[-\frac{\hbar^2}{2m}\nabla^2 + V_{ext}(\mathbf{r})\right]\hat{\Psi}(\mathbf{r}) + g\sum_{i<j}\delta(\mathbf{r}_i - \mathbf{r}_j), \tag{2.68}$$

consisting of terms for the kinetic energy, potential energy and the interaction of the bosons. Let $\Phi(\mathbf{r},t) = \langle\hat{\Psi}(\mathbf{r},t)\rangle$ be a complex function defined as the expectation value of the field operator. This allows a decomposition to

$$\hat{\Psi}(\mathbf{r},t) = \Phi(\mathbf{r},t) + \hat{\Psi}'(\mathbf{r},t). \tag{2.69}$$

Bogoliubov [102] developed his first order theory by treating $\hat{\Psi}'(\mathbf{r},t)$ as a small variation of the field operator $\hat{\Psi}(\mathbf{r},t)$.

Using the Heisenberg equation with the many body Hamiltonian from Equation (2.68) [101], one obtains

$$\begin{aligned} i\hbar\frac{\partial}{\partial t}\hat{\Psi}(\mathbf{r},t) &= \left[\hat{\Psi}(\mathbf{r},t),\hat{H}\right] \\ &= \left[-\frac{\hbar^2}{2m}\nabla^2 + V_{ext}(\mathbf{r}) + \int d\mathbf{r}'\hat{\Psi}^\dagger(\mathbf{r}',t)V(\mathbf{r}'-\mathbf{r})\hat{\Psi}(\mathbf{r}',t)\right]\hat{\Psi}(\mathbf{r}). \end{aligned} \tag{2.70}$$

The effective interaction between two atoms at low energies can be described as point like interaction and thus as

$$V(\mathbf{r}'-\mathbf{r}) = g\delta(\mathbf{r}'-\mathbf{r}), \tag{2.71}$$

where δ denotes the Dirac delta function. The coupling constant g describes the interaction strength for two interacting bosons and is related to the scattering length defined in section 2.2 as $g = \frac{4\pi\hbar^2 a}{m}$.

Replacing the operator $\hat{\Psi}$ by the classical field Φ in Equation (2.70) leads to the Gross-Pitaevskii equation [101]

$$i\hbar\frac{\partial}{\partial t}\Phi(\mathbf{r},t) = \left[-\frac{\hbar^2}{2m}\nabla^2 + V_{ext}(\mathbf{r},t) + g|\Phi(\mathbf{r},t)|^2\right]\Phi(\mathbf{r},t). \tag{2.72}$$

Separating the time dependent part of the wave function as $\Phi(\mathbf{r},t) = \phi(\mathbf{r})\exp(-i\mu t/\hbar)$, the ground state of the system can be obtained as

$$\left(-\frac{\hbar^2}{2m}\nabla^2 + V_{ext}(\mathbf{r}) + g\phi(\mathbf{r})^2\right)\phi(\mathbf{r}) = \mu\phi(\mathbf{r}), \tag{2.73}$$

with μ denoting the chemical potential. The first two terms describe the kinetic and potential energy contributions, while the last one takes the interactions between the atoms into account. In the case of a large number of atoms and strong repulsive interactions we can use the Thomas-Fermi approximation [103]. These condition are normally met in experiments and thus the particle density distribution can be written as

$$n(\mathbf{r}) = \phi^2(\mathbf{r}) = \frac{\mu - V_{ext}(\mathbf{r})}{g}. \tag{2.74}$$

2.3.3. The two component Gross-Pitaevskii equation

Up to this point the considered systems have only consisted of one component. Mixed systems offer a wealth of new possibilities and complications, both experimentally as well as in the theoretical description. Possible realizations include

mixtures of two different species, as described in chapter 4, different isotopes of the same bosonic species or of spin mixtures. To describe the equilibrium state the time independent two component Gross-Pitaevskii equations can be used. These are similar to Equation (2.73) [100]

$$\mu_1\psi_1 = -\frac{\hbar^2}{2m_1}\nabla^2\psi_1 + V_1(\mathbf{r})\psi_1 + g_{11}|\psi_1|^2\psi_1 + g_{12}|\psi_2|^2\psi_1, \tag{2.75}$$

and

$$\mu_2\psi_2 = -\frac{\hbar^2}{2m_2}\nabla^2\psi_2 + V_2(\mathbf{r})\psi_2 + g_{22}|\psi_2|^2\psi_2 + g_{12}|\psi_1|^2\psi_2. \tag{2.76}$$

Here the interaction is defined as $g_{ij} = \frac{2\pi\hbar^2 a_{ij}}{\mu_{ij}}$ for the two components i and j with the reduced mass $\mu_{ij} = m_i m_j/(m_i + m_j)$. The interspecies scattering length is $a_{21} = a_{12}$.

Stability

Assuming a homogeneous gas with constant densities $n_i = |\Psi_i|^2$ and choosing the phase to be independent of space, the two Gross-Pitaevskii equations simplify to [100]

$$\begin{aligned}\mu_1 =& g_{11}n_1 + g_{12}n_2\\ \mu_2 =& g_{12}n_1 + g_{22}n_2.\end{aligned} \tag{2.77}$$

It can be shown that stability conditions in this case are [100]

$$g_{11} > 0, \quad g_{22} > 0 \quad \text{and } g_{11}g_{22} > g_{12}^2. \tag{2.78}$$

Since the interaction g is connected to the scattering length, the condition of the positive sign of the interaction parameter expressed as the requirement of positive scattering lengths in single and dual condensates. This holds also true for single species experiments for the production of Bose-Einstein condensates with a large number of atoms. The maximum number of atoms in a Bose-Einstein condensate with negative scattering length is determined by

$$\frac{N_{cr}|a|}{a_{ho}} = 0.575, \tag{2.79}$$

at which the condensate collapses [101]. Here the harmonic oscillator length is given by $a_{ho} = \left(\frac{\hbar}{m\bar{\omega}}\right)^{1/2}$.

Density Profiles

To gain an insight into the density distributions of mixed trapped gases, we assume the Thomas-Fermi approximation and thus neglect the kinetic energy in the dual species Gross-Pitaevskii equation (2.75) and (2.76). The result becomes

$$\begin{aligned}\mu_1 =& V_1 + g_{11}n_1 + g_{12}n_2 \\ \mu_2 =& V_2 + g_{12}n_1 + g_{22}n_2,\end{aligned} \tag{2.80}$$

which can be expressed as

$$\begin{aligned}n_1 =& \frac{g_{22}(\mu_1 - V_1) - g_{12}(\mu_2 - V_2)}{g_{11}g_{22} - g_{12}^2} \\ n_2 =& \frac{g_{11}(\mu_2 - V_2) - g_{12}(\mu_1 - V_1)}{g_{11}g_{22} - g_{12}^2}.\end{aligned} \tag{2.81}$$

It was shown, that depending on the ratios of the parameters, the two samples may coexist in the same space or will separate [104].

The state of miscible and immiscible condensate can be characterized by the miscibility parameter for trapped gases [105–107], as used in subsection 4.7.1, defined as

$$\Delta = \frac{g_{ii}g_{jj}}{g_{ij}^2} - 1. \tag{2.82}$$

In case of positive Δ the two condensates are miscible and can coexist in the same region. At $\Delta = 0$ a phase transition occurs to an immiscible phase in which the samples repel each other and separate except for an interface region. The stability conditions in Equation (2.78) predict an unstable mixture for $\Delta < -1$.

mixture	$a_K(a_0)$	$a_{Rb}(a_0)$	$a_{KRb}(a_0)$	Δ
^{39}K^{87}Rb	$\approx$ 25 (-35)	100	28.5	1.63(-2.68)
^{41}K^{87}Rb	60.54	100	284	-0.93

Table 2.2.: Overview of the corresponding background scattering lengths to detemine the missibility parameter. The value for ^{39}K is chosen for realistic experimental conditions due to the stability criteria. Values in parenthesis are for background values. Values for ^{41}K from [108], ^{39}K-^{87}Rb mixture subsection 4.7.1. All other from [79].

An overview of realistic experimental conditions as described in chapter 4 is given in Table 2.2, showing that the basic experimental conditions can vary greatly.

3 Experimental apparatus

Since the experimental apparatus has previously been described in great detail [109–111] the focus of this section lies on describing the new experimental techniques implemented for the production of dual-species BECs.

An overview of the vacuum system is shown in Figure 3.1. The collection region on the left side consists of a large glass cell to enable efficient loading of a magneto-optical trap (MOT) for potassium and a dark spontaneous optical force trap (dark-SPOT) [112] for ^{87}Rb. The potassium and rubidium atoms are provided by two commercial not isotope enriched dispenser sources (*SAESGetters*). In addition, light-induced atom desorption [113] is used to desorb atoms from the surface of the glass cell.

Subsequent experiments on dual-condensates are performed in a small L-shaped glass cell (science cell), allowing for good optical access from all six spatial directions. The two cells are separated by a differential pumping stage assuring pressures of $1\times10^{-}11\,\mathrm{mbar}$ in the science chamber. This allows for long lifetimes of the atomic samples in the science cell. The transport of the atoms between the cells is realized with a movable magnetic quadrupole trap described in subsection 3.3.2.

This chapter is structured as follows. In general the focus lies on the production of ^{39}K and ^{87}Rb dual species condensates. First a general overview of the laser systems used for the cooling of potassium and rubidium is given in section 3.1, including the performance of the dark spontanious optical force trap and the optical molasses. In section 3.3 the procedures for magnetic trapping and transport are introduced. In section 3.4 the focus lies on the performance of evaporative cooling in the magnetic trap in dual species experiments. A short introduction into the detection of ultracold gases and the experimental control is given in section 3.5.

The chapter finishes with the description of the production of rubidium BECs in the magnetic trap in section 3.7. Parts of this chapter have been included in a parallel publication [114]. [1]

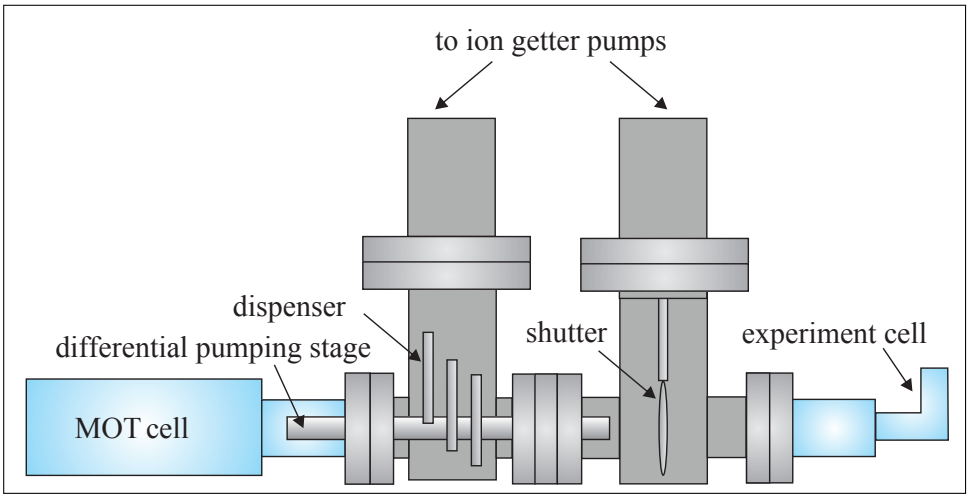

Figure 3.1.: Overview of the vacuum system. Adopted from [110, 111].

3.1. Laser system for trapping and cooling

The laser system can be divided into the rubidium part as described in subsection 3.1.1 and the potassium part described in subsection 3.1.2. Since a detailed description of the laser system has been given in previous PhD-theses [109–111] the focus in this section is to describe the relevant changes. A general overview of the involved frequencies is shown in Figure 3.2.

Both systems deliver light for the following purposes:

- Light for trapping and cooling in a MOT, red detuned from the $F = 2 \rightarrow F' = 3$ transition at 780 nm for rubidium and 767 nm for potassium.
- Light resonant to the $F = 1 \rightarrow F' = 2$ transition refered to as repumper, since it is used to transfer atoms from the $F = 1$ state back into the cooling cycle.

[1] For the internal states of the atoms the notation $|F,m_F\rangle$, where F denotes the hyperfine state and m_F the magnetic substate is used.

- Light resonant to the $F = 2 \rightarrow F' = 2$ transition. This is used to polarize the samples by optically pumping the atoms into magnetically trappable states for magnetic transport.

- Resonant light to the $F = 2 \rightarrow F' = 3$ transition for detection of the atoms.

The experimental apparatus is divided into two parts on two different optical tables to improve decoupling from vibrations. One table hosts the laser system, while the other one hosts the vacuum system. The light is guided via optical fibers to the experiment table which allows for readjusting only parts of the beam path. Light fulfilling the same purpose used in both species, e.g. the cooling light for the MOT in ^{39}K and ^{87}Rb, is superimposed on dichroic mirrors and coupled into the same optical fiber to ease alignment on the experiment table.

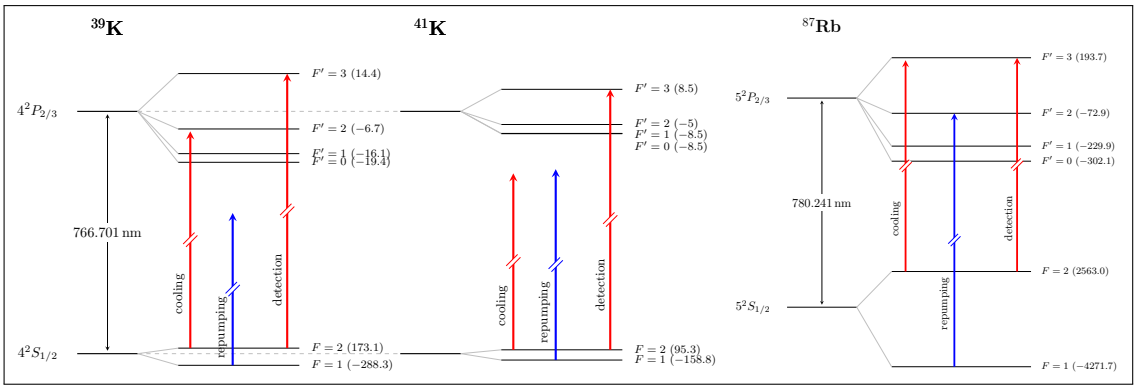

Figure 3.2.: Overview of the relevant levels for the laser cooling for ^{39}K, ^{41}K and ^{87}Rb. Adopted from [110].

3.1.1. Rubidium laser system

An overview of the system is shown in Figure 3.3. The master laser is a grating stabilized diode laser (*DLpro* from *Toptica*) [115], while the repumper laser is a stabilized linear cavity laser (*NarrowDiode* from *RadiantDyes*) [116].

The master laser is stabilized via saturated absorption spectroscopy [117] to the crossover resonance between the $F = 2 \rightarrow F' = 2$ and the $F = 2 \rightarrow F' = 3$ transitions. The spectroscopy light is shifted upwards in frequency by 300 MHz by an acousto optical modulator (AOM) to allow for broad frequency tuning.

The light of the repumper laser is overlapped with the light of the master laser on a fast photo diode. The beat signal is stabilized via a trombone lock scheme [118] (see Figure 3.2).

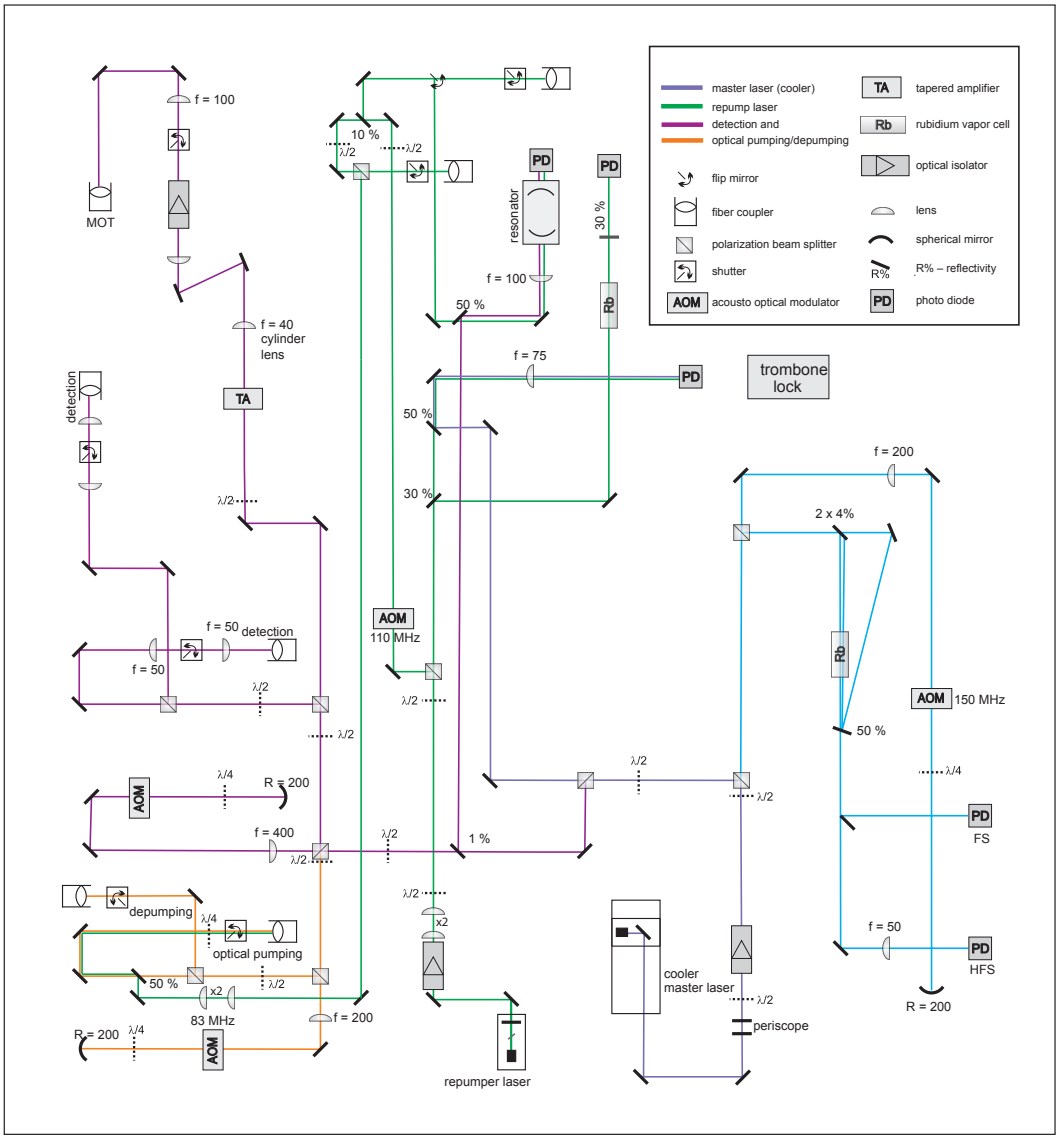

Figure 3.3.: Sketch of the rubidium laser system. Adopted from [109].

The frequency of the light from the master laser is shifted by an AOM by around 410 MHz for cooling and imaging. For cooling in the MOT, the cooling light is amplified up to 800 mW by a tapered amplifier (TA) [119]. For optical pumping and the depumping in the dark-spot MOT the light is shifted by 2×83 MHz in a

double pass AOM. The repumping light is sent through an AOM and shifted by a frequency of 110 MHz before being coupled into fibers for repumping during the MOT-phase, optical pumping and before imaging.

3.1.2. Potassium laser system

The laser system for the generation of the light for potassium is depicted in Figure 3.4. We use grating stabilized diode lasers (*DLpro* from *Toptica*) [115] with an output exceeding 90 mW. The spectroscopy light is shifted with a double pass AOM by 320 MHz and then stabilized to the $F = 2 \rightarrow F' = 2/3$ crossover resonance in ^{39}K [120].

The beat frequencies of the repumping laser and the cooling laser with respect to the reference laser are recorded on two fast photo diodes. A phase locked loop is comparing the beat frequency with a reference frequency from a frequency generator and the beat frequency is stabilized to a multiple of the reference frequency, thus this stabilization scheme allows for a convenient change between the different isotopes by changing the reference frequencies.

The light from the repumping laser is sent through a single pass AOM to allow for fast switching and frequency adjustment for MOT, Molasses, optical pumping and repumping before imaging. The light from the cooling laser is sent through a double pass AOM for the same reasons. The light is then split into imaging, optical pumping and MOT light. The imaging and optical pumping light are combined and sent into optical fibers together with the light for rubidium. The MOT light from the cooling and repumping lasers are overlapped and coupled jointly into the same TA amplifying the light up to 1 W. The TA shows a highly nonlinear behavior for different frequencies, therefore the relative powers have to be adjusted in a fixed ratio (see section 3.2) using a Fabry-Perot cavity.

3.2. Dark spontaneous force optical trap

The simultaneous collection of potassium and rubidium in spatially overlapping magneto-optical traps poses two interrelated problems. First of all, ^{39}K is not particularly well suited for laser cooling due to its small excited state hyperfine splitting [121–123]. Thus, only relatively small samples can be collected and special strategies have to be employed to reach low temperatures [124]. This problem is aggravated by the interaction of the large rubidium samples with smaller potassium samples. In particular two processes are involved. Hyperfine changing collisions

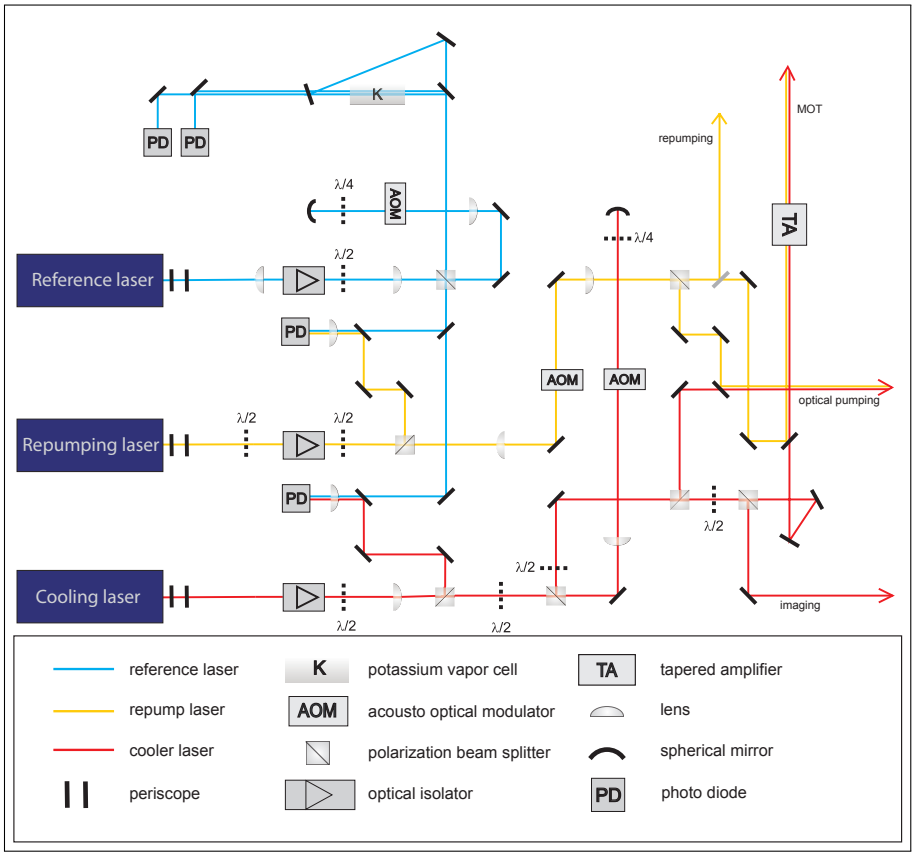

Figure 3.4.: Sketch of the potassium laser system. Adopted from [110, 120]

occur when a the collision of two atoms can exchange the hyperfine state, which can lead to the release energy of kinetic energy. The second process are light assisted collisions, where one or both atoms are excited into an attractive molecular potential. Deexcitation may emit a red detuned photon compared to the one exciting the system. The excess energy will again be released as kinetic energy and thus lead to losses and heating. Both processes lead to similar atom losses from both samples [125], which have a larger relative effect on the small potassium samples.

We overcome these problems by using a potassium MOT with large cooling laser beams in combination with a dark-SPOT [112] for ^{87}Rb as shown in Fig. 3.5. Due to the dark-SPOT, ^{87}Rb atoms at the center of the dual trap accumulate in the $|F = 1\rangle$ state and hence light-assisted collisions are avoided. This dark-SPOT technique has only been used in ^{7}Li-^{85}Rb mixtures before [126], contrary to the more common goal to increase the phase-space density in single species

experiments [112, 127–129].

Dual species MOT

To operate the ^{39}K MOT, a single optical fiber delivers approximately 260 mW of light detuned 24 MHz below the transition from the ground state $|F = 2\rangle$ to the excited state $|F' = 3'\rangle$ and approximately 140 mW detuned 32 MHz below the $|1\rangle \rightarrow |2'\rangle$ transition. These are called cooling and repumping light respectively, despite the fact that their roles are not clearly distinct.

This ratio between the amount of repumping and cooling light was chosen, according to the probability of an atom undergoing a decay to the $|F = 1\rangle$ state during cooling, requiring a 2:1 ratio of cooling to repumping light for ^{39}K.

The same fiber delivers 280 mW of cooling light for ^{87}Rb tuned 24 MHz below the $|2\rangle$ to $|3'\rangle$ transition. About 4 mW of repumping light for ^{87}Rb resonant to the $|1\rangle \rightarrow |2'\rangle$ transition is sent through a special fiber to realize a dark-SPOT (see Figure 3.2)

If experiments with ^{41}K are conducted we use 200 mW of light detuned 17 MHz below the transition from the ground state $|F = 2\rangle$ to the excited state $|F' = 3'\rangle$ and 200 mW of light detuned 32 MHz below the $|1\rangle \rightarrow |2'\rangle$ transition is used. Note that his corresponds to a detuning of both frequencies below the whole upper hyperfine manifold. Due to the lower detuning of the cooling light the probability of an atom undergoing a decay to the $|F = 1\rangle$ state is higher, requiring a 1:1 ratio of cooling to repumping light.

This light is split into six beams using achromatic beam splitters as shown in Figure 3.5. Galilean telescopes are used to magnify the beams to a $1/e^2$ diameter of 34 mm before intersecting in the MOT region. These large beams allow for the efficient accumulation of atoms from the background vapor. To adjust the relative number of atoms in the different species, different loading times are used. In practice e.g. the ^{87}Rb MOT is fully loaded and ^{39}K is loaded for a short time in parallel. Since the number of ^{41}K atoms is lower the procedure is reversed in this case.

Dark Spot MOT

The experimental realization of the dark spot MOT for ^{87}Rb is shown in Figure 3.5. The repumping light on the $|1\rangle$ to $|2'\rangle$ transition and depumping light on the $|2\rangle$ to $|2'\rangle$ transition are delivered in separate fibers. The repumping light is first

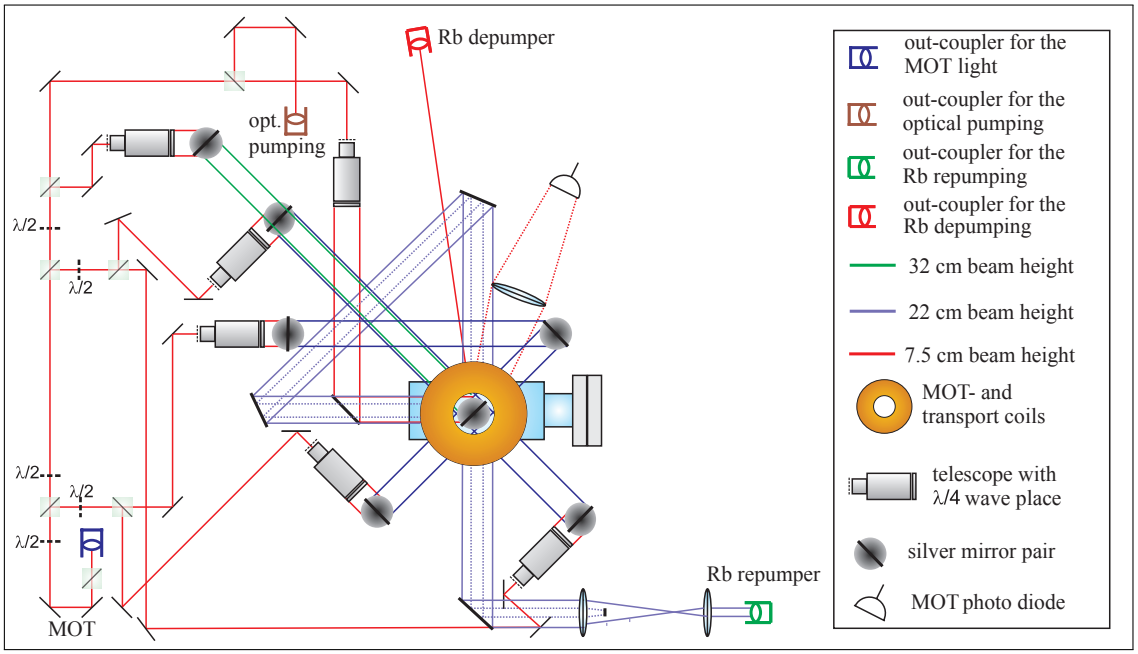

Figure 3.5.: Overview of the laser beams used in the dark-SPOT. Adopted from[110].

collimated and then magnified to a $\frac{1}{e^2}$ beam diameter of 22 mm in a 2:1 telescope. The dark spot in the beam is realized by placing a small opaque disk of 6 mm diameter within this telescope. Thus the effective spot size in the collection region can be varied by translating the disk in the telescope. Due to its large size, the beam and the imprinted dark spot propagate without considerable diffraction over the distance required in the experiment. To obtain a central dark region of the trap surrounded by regions with repumping light, the beam is recycled and passes the trap for a second time in an orthogonal direction (see Figure 3.5). Additional depumping light is required in the dark region, since most atoms would otherwise remain in the cooling cycle while traversing it.

To quantify the number of atoms acquired in the MOT, the fluorescence light is collected with a lens (focal length 80 mm) on a photo diode. The power of the emitted light is given by

$$P = N\hbar\omega_0\Gamma_{sc}, \tag{3.1}$$

where N is the number of atoms, ω_0 is the frequency of the emitted photons and

Γ_{sc} is the photon scattering rate

$$\Gamma_{sc} = \frac{I}{2I_{sat}} \frac{\Gamma}{1 + I/I_{sat} + (\frac{2\Delta}{\gamma})}, \tag{3.2}$$

with the intensity of the light field I, the saturation intensity I_{sat}, the detuning Δ and the natural linewidth γ [62]. The according values for potassium can be found in [70] and for rubidium in [71]. Hence the total number of atoms in the MOT depending on the voltage on the photodiode U_{diode} is

$$\begin{aligned} N_{Rb} &\approx 1.54 \times 10^9 \,\text{atoms/V} \cdot U_{PD} \\ N_{^{39}\text{K}} &\approx 3.60 \times 10^8 \,\text{atoms/V} \cdot U_{PD}. \end{aligned} \tag{3.3}$$

These values assume a detuning of 24 MHz for ^{87}Rb and no detuning for ^{39}K and an I_{Rb} of $\approxeq$ 70 mW for ^{87}Rb and I_K of $\approxeq$ 70 mW for ^{41}K. This is due to the fact that the ^{39}K light is tuned to resonance for atom number measurements. Three experiments

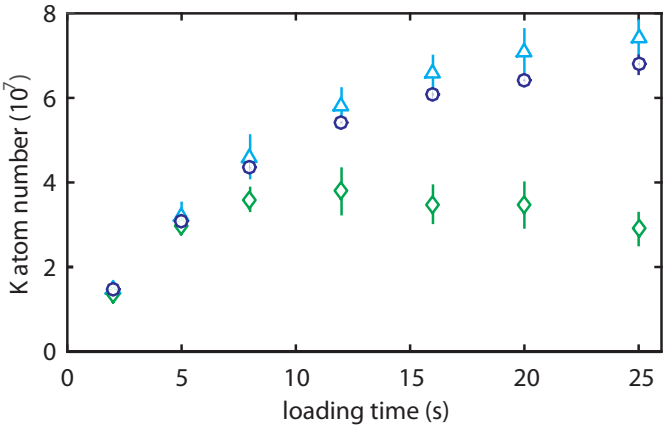

Figure 3.6.: Number of ^{39}K atoms in the dark-SPOT as a function of time in the presence of no ^{87}Rb (triangles), a bright ^{87}Rb MOT (diamonds) and Dark-Spot ^{87}Rb MOT (circles).

are performed to characterize the performance of the dual-species optical trap for mixtures of ^{39}K and ^{87}Rb. Figure 3.6 shows the ^{39}K atom number during MOT loading under different experimental conditions. The maximum number of ^{39}K atoms is obtained by loading a single species MOT. In the presence of a bright ^{87}Rb MOT (realized by removing the opaque disk) severe losses lead to an inferior steady state of about 3×10^7 ^{39}K atoms equivalent to less than half of the number of atoms compared in the single-species case. By using the dark-SPOT for ^{87}Rb

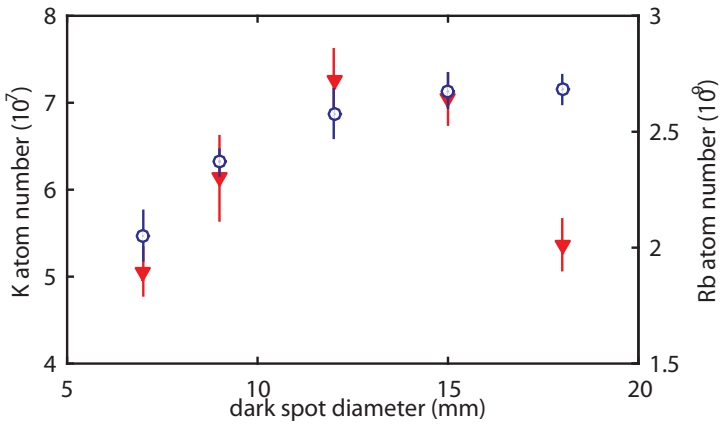

Figure 3.7.: Number of ^{87}Rb atoms (triangles) and ^{39}K atoms (circles) as a function of the dark spot diameter.

these losses are avoided and one obtains almost the same number of ^{39}K atoms as in the single species MOT.

The size of the dark spot was optimized with respect to both species by measuring the atom numbers after 25 s loading time as a function of the spot size (see Figure 3.7). Thus an effective spot diameter of 12 mm was chosen. For smaller sizes, the ^{87}Rb atoms are not depumped properly in the area of the ^{39}K MOT, resulting in losses. Larger sizes lead to a lower number of ^{87}Rb atoms, while no further gain of ^{39}K atoms is obtained. Contrary to previous experiments [129], no decrease in the ^{87}Rb loading rate was observed for this dark spot size. Thus, up to 7×10^7 ^{39}K and 2.7×10^9 ^{87}Rb atoms are collected.

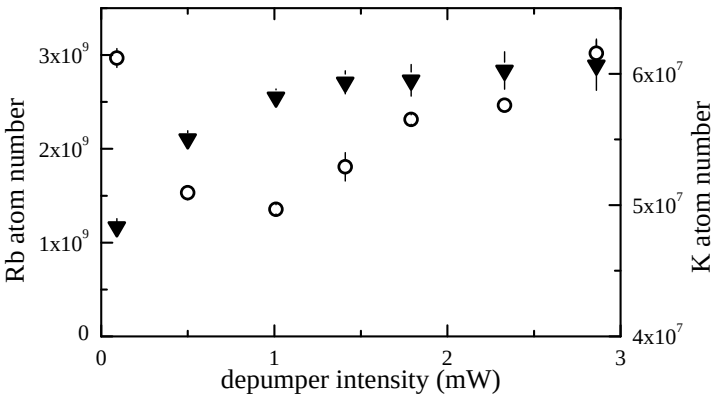

Figure 3.8.: Number of atoms in the dark-SPOT depending on the depumper intensity for ^{87}Rb (triangles) and ^{39}K (circles).

For an effective spot diameter of 12 mm the intensity of the depumping beam was varied (see Figure 3.8) and the number of atoms in the trap was recorded after 25 sec. It shows that the number of ^{39}K atoms increases with the intensity of the depumping beam and stays constant above 1.5 mW showing an efficient decrease in light assisted collisional losses. The ^{87}Rb sample shows an initial decrease in the number of atoms for lower intensities hinting towards an inefficient depumping and hence induced losses without an increase in atom density in the trap center. The number of atoms rises and approaches a value close to the initial one for intensities higher than 2.5 mW. In practice, the loading times of ^{39}K/^{41}K and ^{87}Rb are adjusted to obtain an appropriate relative atom number for subsequent sympathetic cooling.

Optical molasses

After loading sufficient atoms in the dual-species optical trap, an optical molasses is applied to cool the atoms below the Doppler limit. A typical optical molasses works efficiently, if the excited state hyperfine splitting is much larger than the natural linewidth γ, which is the case for rubidium but not for potassium.

The molasses for ^{87}Rb atoms is realized by turning off the magnetic field gradient and detuning the cooling light by $-7\ \gamma$ for a duration of 9 ms.

For potassium, the situation is considerably different. Since the hyperfine splitting is on the same order as the linewidth, a standard molasses procedure is not efficient. However, it has been shown that sub-Dopper cooling is possible when using a more advanced scheme [122, 123]. These schemes rely on the fact, that the neighbouring states lead to a strong depumping into dark states. The population in the bright state and thus the photon scattering can be controlled precisely by the intensity of the repumping light. This reduces the photon reabsorption and allows for lower temperatures

For the case of ^{39}K, this is realized as follows: At the beginning of the molasses phase, the repumping light power is abruptly lowered to 5% of its initial value and tuned on resonance. At the same time the cooling light is detuned to $-0.5\ \gamma$. Within the following 9 ms, its power is linearly ramped down by 50% and the detuning is simultaneously increased to $-2.3\ \gamma$.

In experiments with ^{41}K the molasses is performed with repumping light turned to resonance and lowered to 5% of the initial power. The cooling light is ramped from $-1\ \gamma$ to $-1.5\ \gamma$ within 9 ms while the molasses for ^{87}Rb is performed in parallel.

3.3. Magnetic trapping and transport

For small magnetic fields the energy of the quantum states used in our experiments changes according to the linear Zeeman effect $E(m_F,B) = g\mu_B m_F B$ [90]. Here g is the Landé g-factor, μ_B is the Bohr magneton, m_F the magnetic substate and B the magnetic field magnitude. Since it is impossible to create a local magnetic field maximum, a trap has to be designed to provide a magnetic field minimum. Therefore the states $|F = 2, m_F = 2\rangle$, $|F = 2, m_F = 2\rangle$ and $|F = 1, m_F = -1\rangle$, which reduce their energy for lower magnetic field strengths, are available for magnetic traps. Both K and Rb atoms in the $4^2S_{1/2}$ manifold have a magnetic field splitting of $|E/(h \cdot m_F)| = 700kHz/G$.

3.3.1. Optical pumping

After the optical molasses the atoms are distributed over all magnetic substates. Since only distinct states are magnetically trappable and a fully polarized sample is favorable for further experiments both species are optically pumped into the $|2,2\rangle$ state. For this purpose, a homogeneous offset field of 15 G is applied and σ_+ polarized light close to the $|2\rangle$ to $|2'\rangle$ transition is applied to both atomic species for a duration of 1 ms. Additionally, repumper light is applied to prevent atom loss to the ground state $|1\rangle$ manifold. The optical pumping increases the number of transferred atoms by 50%.

This process is of particular importance for the work with potassium, as collisions with other spin states induce spin changing collisions that may release energy and lead to atom loss and heating. Due to the low number of atoms available, already small losses compared to the other species, would make it impossible to achieve cold and large enough samples.

3.3.2. Magnetic transport

To obtain an efficient loading of the MOT the background pressure of alkali atoms has to be high. Since this is contrary to long sample lifetimes, the samples are mechanically transported from the MOT cell to the science cell (see Figure 3.1). After optical pumping, both species are transferred into a magnetic quadrupole trap mounted on a transport stage (*404XR* from *Parker*) as depicted in Figure 3.9a. The current through the quadrupole coils is abruptly increased to 15 A to catch the atoms and then ramped up in 50 ms to 45 A. The coils produce a magnetic field

gradient of B'/I =4.35 G/(cm· A) resulting in a gradient of 196 G/cm in the vertical direction. During this procedure the atoms change their spatial spin orientation while maintaining their spin state. The procedure was optimized empirically to obtain maximal transfer with minimal additional heating.

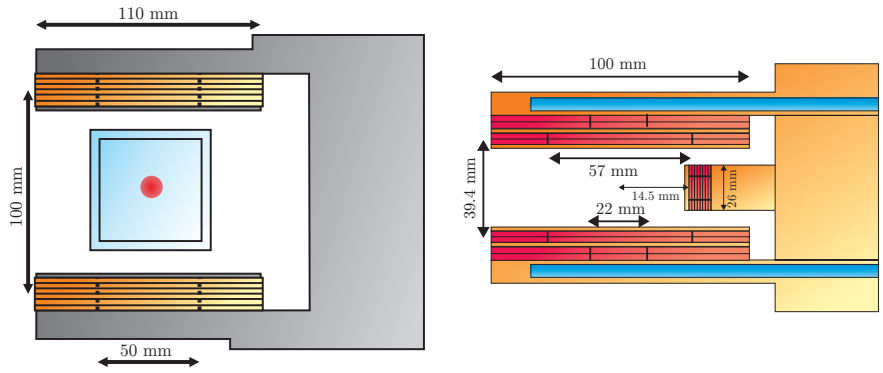

(a) MOT and transport coils (b) Quadrupole and QUIC coils

Figure 3.9.: (a) MOT cell with surrounding MOT and transport coils. (b) Water cooled magnetic quadrupole, QUIC and homogeneous magnetic field generating coils around the science cell. Adopted from [109, 110].

The atoms are then moved to the science chamber within 1.2 s by mechanically moving the quadrupole coils. There they are loaded into a stationary magnetic quadrupole potential shown in Figure 3.9b. This is achieved by lowering the transport gradient to 152 G/cm, while increasing the stationary coil gradient within 800 ms to 309 G/cm. During this transfer, the atomic clouds move a transverse distance of 4.5 cm into the L-shaped science cell.

3.3.3. Quadrupole and QUIC trap

The quadrupole trap is shown in Figure 3.9b. It consists of two sets of coils with 40 windings with 36.4 mm separation on the inner pair and 32 windings with 46.8 mm separation on the outer one. For the use as a magnetic trap they are connected in an anti-Helmholtz configuration as shown in Figure 3.10 producing a magnetic field gradient of 8.83 G/(A·cm). Since the trap is sensitive to temperature fluctuations the coils are mounted on a water cooled copper holder. The cooling water is temperature stabilized to 19±0.1 °C by a chiller (*HIB*).

After initial evaporative cooling in the quadrupole (QP) trap (see section 3.4) the samples are transfered into a Quadrupole Ioffe-Pritchard configuration (QUIC)

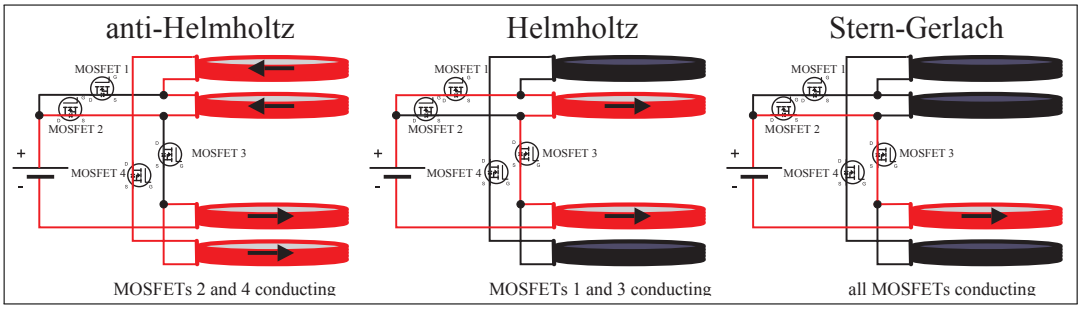

Figure 3.10.: Switching circuit used to switch between quadrupole trap (anti-Helmholtz), homogeneous field (Helmholtz) and inhomogeneous fields for Stern-Gerlach type experiments (Stern-Gerlach). Adopted from [109].

trap [130] since the sample cannot be cooled to lower temperatures and atoms in the wrong state cannot be removed in the quadrupole trap (see Figure 3.4) [110].

The trap consist of an additional Ioffe-coil with 60 windings between the quadrupole coils at a distance of 14.5 mm from the geometric axis as shown in Figure 3.9b. By increasing the current through the Ioffe coil the field minimum and thus the trap center is shifted as shown in Figure 3.12 and transforms the quadrupole trap into a harmonic trapping potential. To reduce drifts due to thermal effects the coil is kept small to reduce the thermal load. To stabilize the temperature the holder is thermally coupled to the water cooled holder of the quadrupole trap as shown in Figure 3.11. To load the atoms into the QUIC-trap

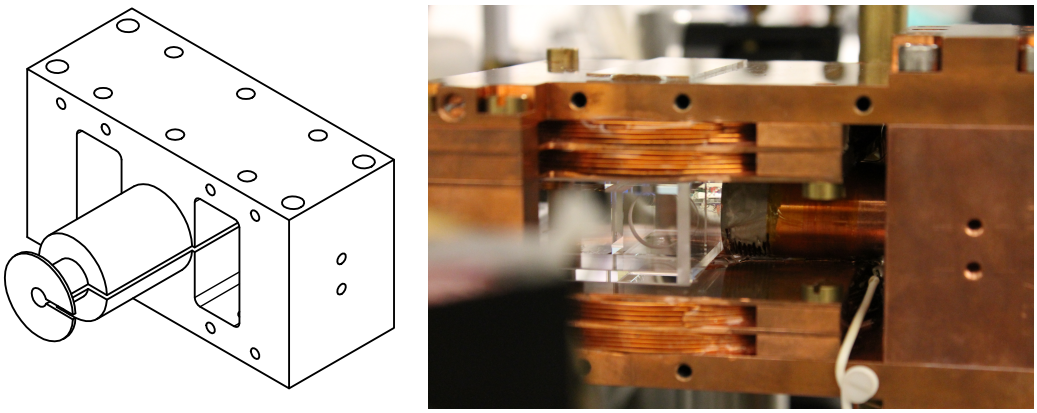

Figure 3.11.: Drawing and image of the QUIC magnetic trap.

the current through the Ioffe coil is increased within 1.4 s to 12.85 A while the

current through the quadrupole coils is held constant at 25 A. The magnetic field in the trapping region is shown in Figure 3.12 providing an offset magnetic field in the trap center of 1 G at the final current.

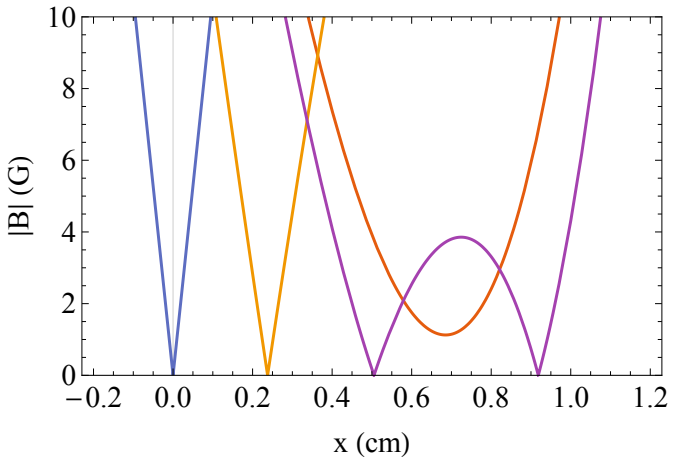

Figure 3.12.: Magnetic field along the axis of the Ioffe-coil. Fields are shown for different values of the current through the Ioffe-coil with $I_I = 0$A (blue), $I_I = 8$A (yellow), $I_I = 12$A (purple) and $I_I = 12.85$A (orange). The current through the quadrupole coils is kept constant at $I_{QP} = 25$A.

The magnetic potential has a center shifted by approximately 6.5 mm compared to the center of the quadrupole trap and provides axial and radial trapping frequencies of $\nu_a = 17.4$ Hz and $\nu_r = 195$ Hz for ^{87}Rb and $\nu_a = 26$ Hz (25 Hz) and $\nu_r = 291$ Hz (284 Hz) for ^{39}K (^{41}K). These frequencies can be measured by displacing the trapped cloud from its equilibrium position and recording the position after a certain hold time. An example is given for ^{39}K in an expanded trap is given in Figure 3.13.

Helmholtz and Stern-Gerlach configuration

To address magnetic Feshbach resonances and to supply a homogeneous magnetic field for state preparation, the inner coils of the magnetic trap can also be used in a Helmholtz configuration as shown in Figure 3.10. This produces a homogeneous field with a strength of 9.51 G/A. To produce an inhomogeneous field only one coil can be addressed. Thus it is possible to conduct Stern-Gerlach type experiments during time-of-flight to distinguish the different m_F components of the sample.

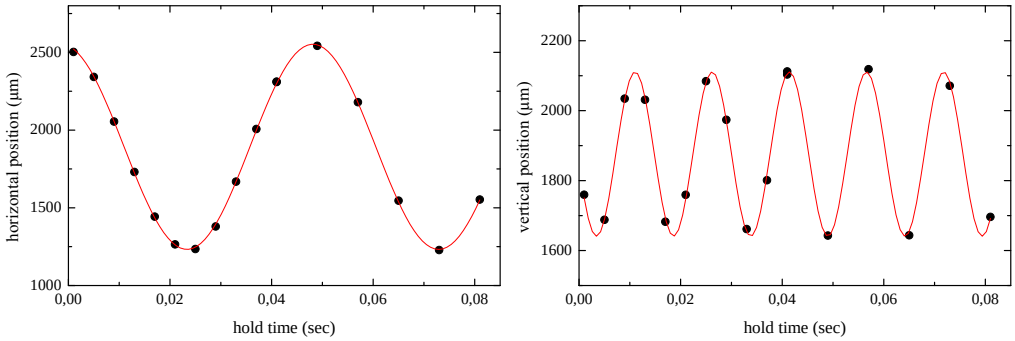

Figure 3.13.: Trapping frequency measurement of the QUIC trap

3.3.4. High stability current supply

To supply the current to produce the necessary magnetic fields two different power supplies are used. Figure 3.14 shows the schematic to switch between the two. For magnetic trapping a line powered high stability power supply (*UCS 65A/25V* from *High Finesse*) is used. This low noise power supply suffered from long term drifts. These drifts are compensated by an additional servo loop measuring the output current with a high precision current transducer (*Danfysik*) and regulating the setpoint accordingly. To achieve an even better magnetic field stability during our

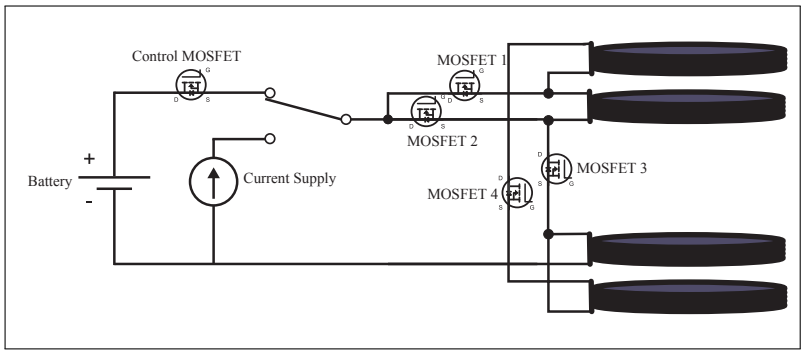

Figure 3.14.: Switching circuit used to switch between the high precision current supply and the battery supplied high precision current supply.

experiments a battery powered power supply was built. This solution avoids the 50 Hz noise typicaly obtained after rectification of the line current. The current is delivered from three car batteries in series, measured by a high precision current transducer (*IT 200-S ULTRASTAB* from *LEM*) and regulated with a MOSFET. The schematics for the controlling servo loop are given in the Appendix in A.2. We

measure the magnetic field fluctuations at the position of the atoms by determining the spectroscopic width of the $|1,-1\rangle \rightarrow |1,0\rangle$ transition at 117.45 G. The result is shown in Figure 3.15. A fit with a Gaussian distribution to the transfered fraction yields a full width at half maximum of 2.85 kHz. Since the transition frequency varies with 700 kHz/G the corresponding magnetic field stability is 4.1 mG. This measurement was performed with pulse lengths of 250 µs thus leading to a Fourier limit of the frequency resolution of 4 kHz thus the upper limit for the magnetic field fluctuation at 117.45 G is 5 mG.

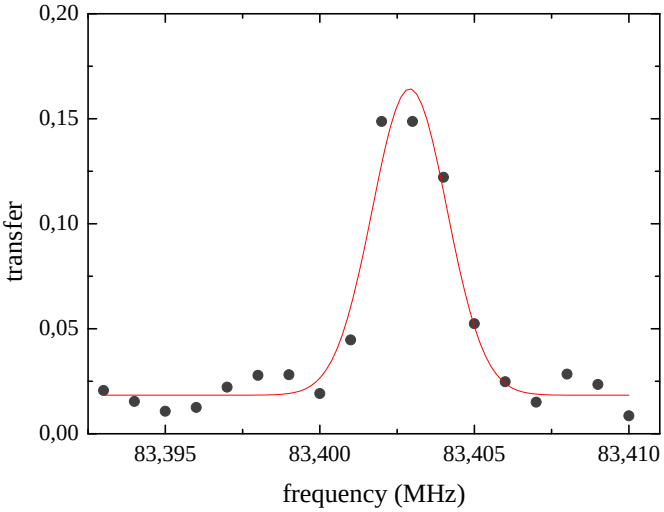

Figure 3.15.: Transfered fraction after spectroscopy on the $|1,-1\rangle \rightarrow |1,0\rangle$ transition as a function the pulse frequency for a magnetic field of 117.45 G. The width of the feature determines the maximum magnetic field fluctuations.

3.3.5. Magnetic field stabilization

The experiment table is surrounded by three large coils to compensate for the background magnetic field. These coils provide a compensated field in the region of the MOT cell. Initially these coils were regulated to compensate the magnetic field also in the science cell. However, due to the large size of the coils they affected the magnetic field in a neighboring laboratory. To compensate the magnetic field around the science cell a smaller set of coils was therefore implemented. Since these are smaller, the current in the coils can be switched during an experimental run without influencing other experiments. Besides an overall static compensation,

the magnetic field is actively stabilized in the vertical direction. A magnetic field sensor (*Mag-03* from *Bartington*) constantly measures the magnetic field close to the science chamber. A servo loop on a field-programmable gate array (*LabVIEW RIO Evaluation Kit* from *National Instruments*) is used to control the current through two rectangular coils in Helmholtz configuration. This provides a field with an opposite phase and thus reduces magnetic field fluctuations. The remaining short term background magnetic field noise close to the science chamber measured with an external Hallprobe is 0.5 mG while day to day drifts can be mostly neglected.

3.4. Sympathetic cooling of potassium in a magnetic trap

The sympathetic cooling of potassium is performed in two steps. The first step is done in the quadrupole trap to make use of the high rethermalization rates [103] in this configuration. Cooling to quantum degeneracy is however not possible since Majorana spin flips near the magnetic field zero lead to losses [131].

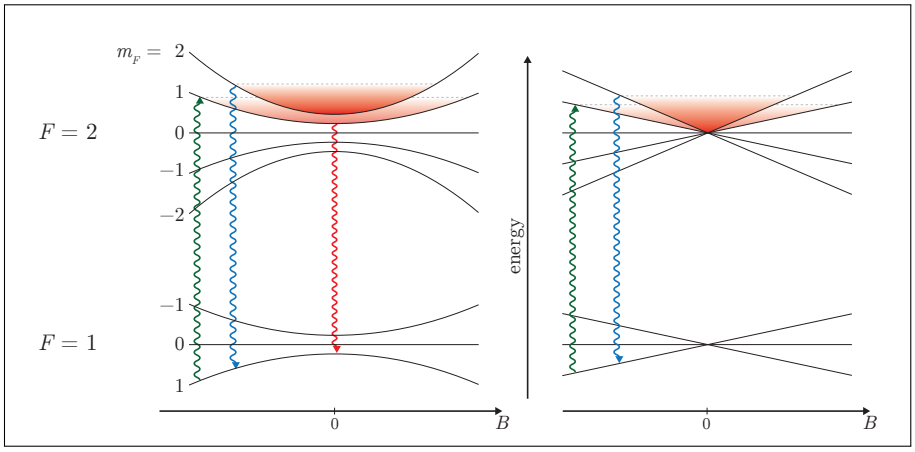

Figure 3.16.: Magnetic field dependent energy levels and the evaporative cooling transition (blue), the reexcitation transition into the $|2,1\rangle$ state (green) and the removal transition (red) for the QUIC trap (left) and the quadrupole trap (right). Adopted from [110].

The evaporation is achieved by driving transitions from the $|2,2\rangle$ state to the $|1,1\rangle$ state as shown in Figure 3.16. The drawback is the production of hot atoms in the $|2,1\rangle$ state due to transitions further away from the center of the

trap [25, 26, 132], which can lead to heating of the potassium sample [110]. This ultimately prevents the loading of sufficient atoms in the dipole trap to produce BEC. Hence further cooling is realized in a harmonic magnetic potential, where losses due to atoms in the $|2,1\rangle$ state can be suppressed by driving transitions from the $|2,1\rangle$ state to the $|1,1\rangle$ state in the trap center and hereby removing the atoms in the wrong state [26, 121, 132, 133].

Sympathetic cooling of potassium in a quadrupole trap

The rubidium atoms are evaporatively cooled by using a microwave field which transfers them from the trapped $|2,2\rangle$ state to the untrapped $|1,1\rangle$ state as shown in Figure 3.16. Radio frequency transitions to untrapped m_F states would also remove potassium atoms since both species have the same Zeeman splitting. Due to the spatial overlap of the two clouds, this leads to sympathetic cooling of the ^{39}K atoms. In the experiment the microwave frequency is ramped from $\nu_0 + 135$ MHz to $\nu_0 + 30$ MHz within 5 s, where ν_0 is the frequency of the unperturbed hyperfine splitting in ^{87}Rb. The quadrupole gradient is simultaneously reduced to 220 G/cm. At this point losses due to collisions with rubidium atoms in the $|2,1\rangle$ state become detrimental and the evaporation is stopped.

	Sequence	N	PSD	T (K)
^{87}Rb	MOT/Molasses	2.7×10^9	-	35×10^{-6}
	QP trap initially	6×10^8	$\approx 9.5 \times 10^{-7}$	$\approx 3.7 \times 10^{-4}$
	QP trap end	2.2×10^8	4.6×10^{-5}	1×10^{-4}
	QUIC initially	2×10^8	2.6×10^{-5}	8.3×10^{-5}
	QUIC end	5×10^6	0.76	7.9×10^{-7}
^{39}K	MOT/Molasses	7×10^7	-	117×10^{-6}
	QP trap initially	2.3×10^6	$\approx 1.2 \times 10^{-8}$	$\approx 3.7 \times 10^{-4}$
	QP trap end	1.5×10^6	1.1×10^{-6}	1×10^{-4}
	QUIC initially	1.5×10^6	4.5×10^{-7}	8.3×10^{-5}
	QUIC end	7×10^5	0.24	7.9×10^{-7}

Table 3.1.: Overview of the number of atoms, temperatures and PSD of ^{39}K and ^{87}Rb in different phases of the experiment.

Sympathetic cooling of potassium in a QUIC trap

Further microwave evaporative cooling is performed for 28 s by ramping the microwave frequency from $\nu_0 + 30\,\mathrm{MHz}$ to $\nu_0 + 2.54\,\mathrm{MHz}$. Atoms accidentally transferred into the $|2,1\rangle$ state are removed by a second microwave as shown in Figure 3.16 making use of the non zero offset magnetic field in the center of the trap. This microwave is resonant to the $|2,1\rangle \rightarrow |1,1\rangle$ transition at 1 G and thus removes the atoms from the center of the trap. The evaporation is stopped before losses due to the negative background scattering length of ^{39}K become relevant.

An overview of the achieved temperatures, number of atoms and the corresponding PSD is given in Table 3.1 for mixtures of ^{39}K and ^{87}Rb and in Table 3.2 for mixtures of ^{41}K and ^{87}Rb.

	Sequence	N	PSD	T (K)
^{87}Rb	QUIC initially	2.5×10^7	5×10^{-5}	3.3×10^{-5}
	QUIC end	2.6×10^6	0.056	1.5×10^{-6}
^{41}K	QUIC end	4.5×10^5	0.025	1.5×10^{-6}

Table 3.2.: Overview of the number of atoms, temperatures and PSD of ^{41}K and ^{87}Rb in different phases of the experiment.

Problems with evaporative cooling in magnetic traps

While the first experiments with ^{87}Rb on the described apparatus [63, 134] used a hybrid trap configuration [135], this road is not feasible for the mixture of potassium and rubidium. Figure 3.16 shows the magnetic field dependent energy levels in the QUIC and QP trap. Microwave radiation is used to drive the $|2,2\rangle \rightarrow |1,1\rangle$ transition to remove the atoms with the highest potential energy from the trap (blue). While transversing outwards, the same microwave radiation becomes resonant to the $|1,1\rangle \rightarrow |2,1\rangle$ transition (green) and will be transfered back into the trapped $|2,1\rangle$ state. This process is especially harmful since the atoms gain kinetic energy while moving outwards. While in a QP these atoms cannot be removed, the magnetic offset in the trap center of a QUIC trap allows to apply a second microwave resonant to the $|2,1\rangle \rightarrow |1,1\rangle$ transition (red) and thus remove atoms in the $|2,1\rangle$-state from the trap [136–138]. Figure 3.17 shows two results when evaporating a ^{87}Rb sample in the QP and QUIC trap below the critical temperature for BEC. When the second microwave is applied to clean the sample, no residual atoms in the $|2,1\rangle$-state can

be detected. If the same experiment is conducted without the cleaning microwave we detect up to 10 % of the total number of atoms in the $|2,1\rangle$-state at the end of the evaporation.

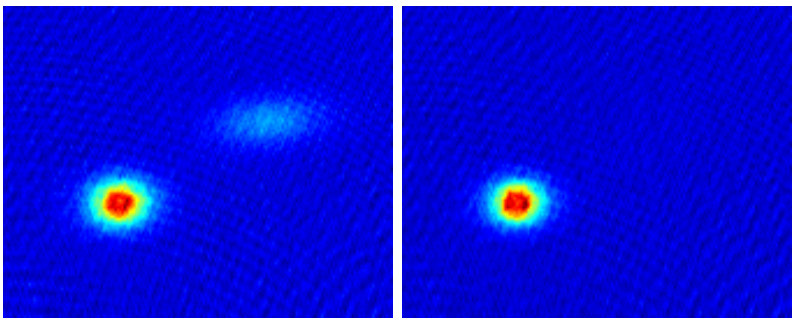

(a) without 2nd microwave (b) with 2nd microwave

Figure 3.17.: ^{87}Rb BEC after release from the QUIC trap. The different spin components are separated by an inhomogenious field while turning off the trap. (a) both $|2,2\rangle$ and $|2,1\rangle$-component visible. (b) same as (a) but a second microwave frequency resonant to the $|2,1\rangle \rightarrow |1,1\rangle$ transition is applied during evaporation in the QUIC trap removing the $|2,1\rangle$-component.

By using a hybrid trap in single species experiments working with ^{87}Rb this effect does not cause difficulties [63, 134, 135, 139], since the evaporation in the quadrupole trap is shorter and thus fewer atoms in the $|2,1\rangle$-state are produced. Moreover the loading process from the QP into the hybrid trap removes atoms in the wrong state by compensating the gravity by the magnetic field gradient for atoms in the $|2,2\rangle$-state while atoms in other states are not trapped in the vertical direction. Lowering the magnetic gradient of the trap during evaporative cooling, to make use of this effect, was evaluated but was not feasible since the collision rate in a relaxed trap was too low for efficient rethermalization.

However the situation is different for dual species experiments since spin changing collisions between the components can lead to additional losses [140, 141] and limits the efficiency of evaporation and sympathetic cooling [140–143].

In the presented apparatus, this ultimately prevented the production of potassium BECs since the temperatures that were possible to reach in the QP trap were not sufficiently low to transfer the sample into the dipole trap. The effect of this process in this apparatus is shown in Figure 3.18. We prepare a sample of ^{87}Rb and ^{39}K in the QP trap and hold the samples for variable times after the evaporation, while

fixing the temperature of the ^{87}Rb sample by leaving the microwave radiation on at the end frequency of the evaporation. We record the temperature of the sample after different times. The temperature of the ^{39}K rises and a full rethermalization does not take place. For comparison the same time series is recorded for ^{39}K after removing the ^{87}Rb sample by a resonant light pulse showing a strongly suppressed heating. To exclude the effects of inelastic heteronuclear three-body recombination in this experiment, the microwave is turned off and the temperature of the potassium sample is recorded in the presence of rubidium.

It shows that a great part of the observed heating must be accounted to the interaction of the ^{87}Rb sample with the microwave, since one observes a lower heating although the temperature of the rubidium sample is not kept constant and thus a great part of the heating must be accounted to the production of atoms in the $|2,1\rangle$-state.

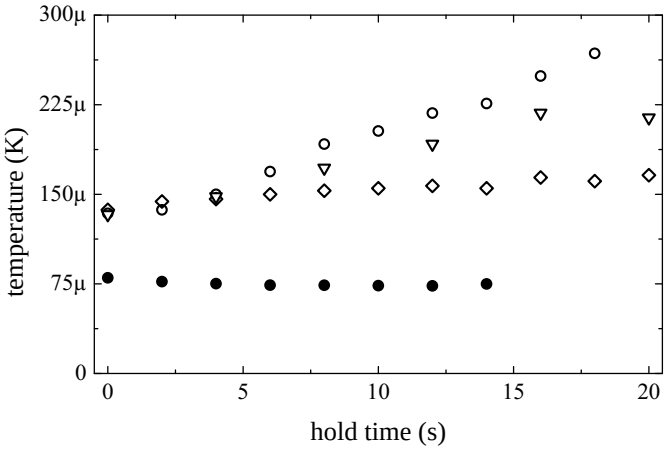

Figure 3.18.: Heating of ^{39}K due to ^{87}Rb in the $|2,1\rangle$ state in the quadrupole trap. The microwave radiation used for evaporation of ^{87}Rb is kept on to hold the temperature of the ^{87}Rb sample constant (filled circles), while the temperature rises in the ^{39}K sample (open circles). If the microwave radiation is not applied the ^{39}K sample is heated less (triangles). By completely removing the ^{87}Rb sample the heating in ^{39}K is strongly suppressed (diamonds).

3.5. Detection of atomic gases

The detection system used for imaging the cloud is shown in Figure 3.19. After release from the trap the expanding atoms are illuminated by a resonant light beam. The maximum time of flight after release in this apparatus can range up to 30 ms. The light beam is afterwards expanded by an f=100 mm and an f=300 mm lens with 400 mm distance to each other, resulting in a 3 times magnification of the beam which is imaged onto a CCD camera (*Luca* from *Andor*). To increase the field of view a 1:2 demagnification telescope can be inserted into the beam path.

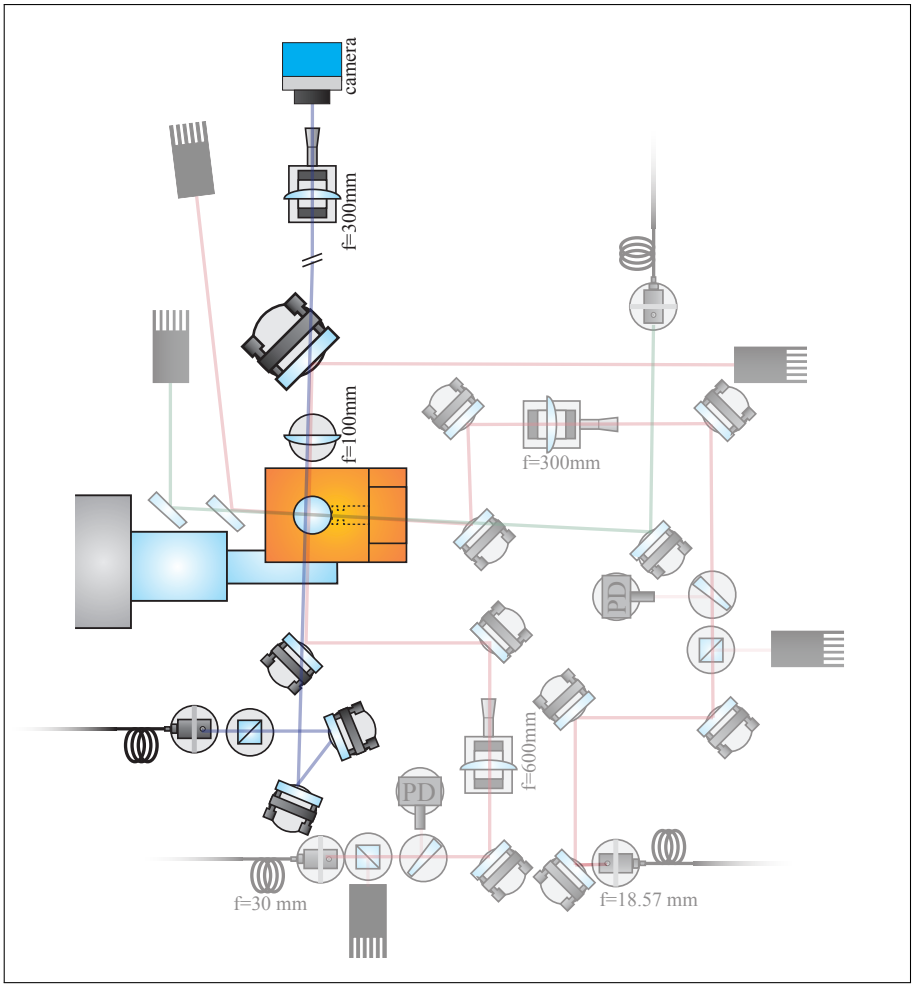

Figure 3.19.: Overview of the science cell. The parts relevant for the imaging are highlighted.

The intention is to determine the integrated atom column density $\tilde{n}(x,y)$ of an

atomic cloud. The attenuation of the incoming beam is given by

$$I(x,y) = I_0(x,y) \cdot e^{-\tilde{n}(x,y)\sigma}, \tag{3.4}$$

where the effective scattering cross section in terms of the resonants cross section σ_0 is defined as [90]

$$\sigma = \frac{\sigma_0}{1 + 2I/I_{sat} + (\frac{4\Delta^2}{\gamma^2})}. \tag{3.5}$$

In the experiment we take an image of the beam with the absorbing atoms and one without corresponding to measuring the intensities I_A and I_B. From this the optical density can be determined to

$$D = \ln I_B(x,y) - \ln I_A(x,y). \tag{3.6}$$

Figure 3.20 shows an example of this method for a ^{39}K and a ^{87}Rb sample demonstrating the strong noise suppression of this method. Since the area of a camera pixel in the imaging plane and the conversion efficiency of the camera are known, the number of atoms can be calculated.

To improve the precision of the calculated number of atoms we take the scattering properties of the atoms into account and calibrate the imaging system with a method developed in the group of D. Guéry-Odelin [144]. This procedure introduces a factor α to compensate for these deviations and thus the number of atoms is determined by

$$n = \left(\log I_B - \log I_A + \frac{I_B - I_A}{\alpha I_{sat}}\right) \frac{\alpha}{\sigma_0}, \tag{3.7}$$

where the scattering cross section for ^{87}Rb is $\sigma_{0,Rb} = 2.907 \times 10^{-9}\, cm^2$ and $I_{sat,Rb} = 1.669\, mW/cm^2$ [71] and for ^{39}K and ^{41}K the parameters are $\sigma_{0,K} = 2.807 \times 10^{-9}\, cm^2$ and $I_{sat,Rb} = 1.75\, mW/cm^2$ [70]. The correction factor α was determined experimentally to $\alpha_{Rb} = 1.88$ for ^{87}Rb, $\alpha_{K39} = 1.11$ for ^{39}K and $\alpha_{K41} = 1.24$ for ^{41}K.

In practice absorption images of both species are taken after free expansion at the end of every experimental run with a detection pulse with a length of 38 µs and circular polarization. To obtain information about both species, the absorption image of potassium is typically taken after a total time of flight of about 15 ms. This image is shifted into a covered area of the camera chip within 2 ms and then the image of ^{87}Rb is taken. The used light is in both cases resonant to the $|2\rangle$ to $|3'\rangle$ transition. Since experiments with these species take place in the $|F = 1\rangle$ manifold, repumping light is applied 200 µs prior to the imaging light.

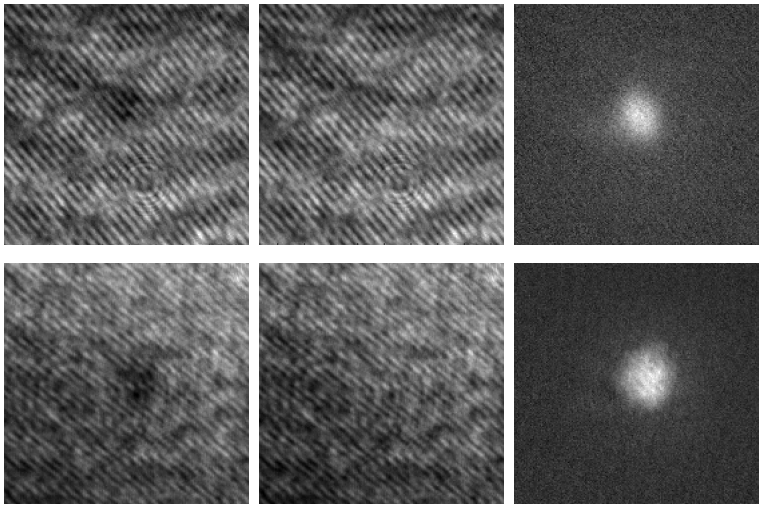

(a) Absorption (b) Beam (c) Processed

Figure 3.20.: Principle of the imaging sequence for ^{39}K in the upper and ^{87}Rb in the lower row. The beam (b) is subtracted from the absorption image (a) to calculate the optical density (c).

To determine the temperature T of the trapped cloud, we fit a Gaussian distribution to the column density of the image and determine the Gaussian width σ_i of the expanding cloud. The width of the cloud is given by

$$\sigma_i(t) = \sqrt{\sigma_0^2 + t^2 \frac{k_B T}{m}}. \tag{3.8}$$

Assuming a harmonic trap, the initial width of the cloud is given by

$$\sigma_0 = \sqrt{\frac{k_B T}{\omega_i m}}, \tag{3.9}$$

where ω_i is the trapping frequency of the harmonic potential and m the mass of the atom. Since the initial size and the expansion are inversely proportional to the mass, imaging of the lighter species first is favorable.

The state composition can be analyzed by turning on an inhomogeneous magnetic field generated by one of the coils (see Figure 3.10) in the first 5 ms of the expansion. This fully separates the different m_F-components and results in different cloud positions during imaging allowing for the detection of small admixtures in other states.

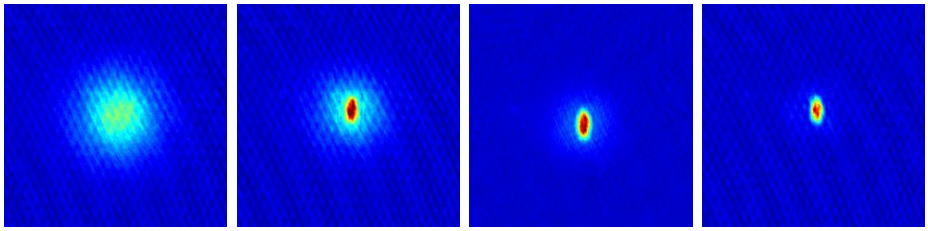

(a) $T \approx 340\,\mathrm{nK}$ (b) $T \approx 250\,\mathrm{nK}$ (c) $T \approx 120\,\mathrm{nK}$ (d) $T < 120\,\mathrm{nK}$

Figure 3.21.: Emerging of a ^{87}Rb-BEC from the thermal cloud while lowering the temperature. The images are taken 22 ms after release from the QUIC-trap and temperatures are given for the thermal component.

3.6. Experiment control

The experiment is controlled by a *LabVIEW* program controlling three output cards in real time. Details of the program can be found in [110]. The output cards supply 32 digital 5 V TTL level output channels (*DIO-32HS*), 16 analog output channels with a voltage range of ±10 V. These are divided into 8 channels with a resolution of 12 bit (*NI PCI-6713*) and 8 channels with 12 bit resolution (*NI PCI-6733*). The system supports the programming of multiple variable arrays, thus allowing for a continuous operation. This reduces the thermal fluctuations in the system between single experiments and allowed a large number of experiments during the night as needed for the experiments detailed in chapter 5.

3.7. ^{87}Rb BEC in the QUIC trap

In case only ^{87}Rb is used, further evaporation in the QUIC trap allows the production of almost pure ^{87}Rb BECs. The phase space density as a function of the atom number during the evaporation is shown in Figure 3.22.

The efficiency of the evaporation can be characterized by the ratio of gain in phase space density ρ to number of evaporated atoms N as

$$\gamma = \frac{d \ln \rho}{d \ln N}. \tag{3.10}$$

The efficiencies obtained from linear fits in Figure 3.22 are $\gamma = 2.4$ in the quadrupole trap and $\gamma = 3.2$ in the QUIC trap showing the positive effect of avoided Majorana losses and avoided colissions with atoms in the $|2,1\rangle$ state. Figure 3.21 shows the

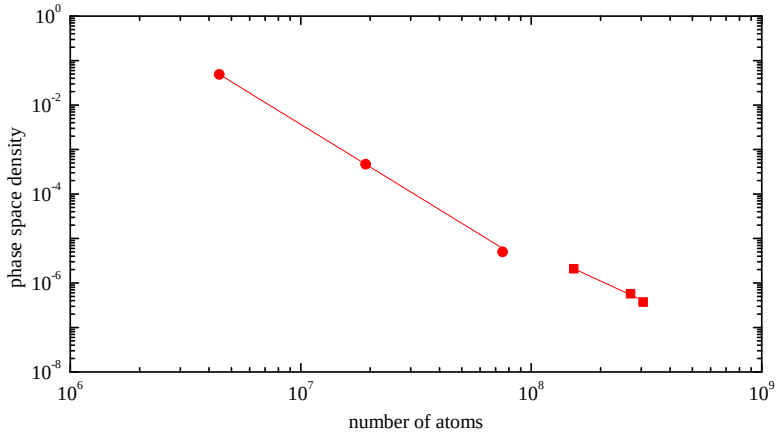

Figure 3.22.: Phase space density vs. number of atoms for ^{87}Rb in the quadrupole trap (diamonds) and QUIC trap (circles).

transition from a thermal cloud to an almost pure BEC. The number of atoms in the pure BECs are about 5×10^5.

4 Tunable dual-species Bose-Einstein condensates

The production of quantum gases with tunable interaction includes a number of peculiarities. This chapter focuses on the experimental methods used to solve these and to demonstrate the production and control of single and dual species BECs with tunable inter- and intraspecies interaction.

The chapter is structured as followed. In section 4.1 the production of BECs in optical potentials is discussed. The utilized dipole trap system is introduced and the production of ^{87}Rb in these is demonstrated. The methods to control the internal states of the atoms are introduced in section 4.2. The general work and characterization of Feshbach resonaces is explained in section 4.3. This leads the presentation of the production of ^{39}K BECs (see section 4.4), ^{39}K-^{87}Rb dual BECs (see section 4.5) and ^{41}K-^{87}Rb BEC (see section 4.6) mixtures. The chapter finishes with a demonstration of the control of the inter- and intraspecies interaction in section 4.7. The results of parts of this chapter have been included in a parallel publication [114].

4.1. Trapping in an optical potential

In order to tune the interaction strength magnetic Feshbach resonances will be exploited and thus the atoms have to be transfered from a magnetic trap into an optical dipole potential. The overall effective potential of the confining dipole trap can be written as

$$U(\mathbf{r}) = U_{dip} - mgz, \tag{4.1}$$

where U_{dip} is the dipole potential, m is the mass of the atom, z is the vertical coordinate and g the gravitational acceleration. For a dipole trap the potential is

given by [145]

$$U_{Dip}(\mathbf{r}) = \frac{3\pi c^2}{2\omega_0^3}\left(\frac{\Gamma}{\omega_0 - \omega} + \frac{\Gamma}{\omega_0 + \omega}\right) I(\mathbf{r}), \tag{4.2}$$

where c denotes the speed of light in vacuum, ω_0 the frequency of a nearby transition, ω the frequency of the trapping laser and I the local intensity of the trapping laser beam.

4.1.1. Dipole laser system

The dipole trap is constructed as a far red-detuned, crossed-beam dipole trap at a wavelength of 1064 nm offering minimal absorption. The light is generated by a narrow bandwidth monolithic ring laser (*Coherent Mephisto*) and amplified by a fiber amplifier (*Nufern PSFA-1064-50mW-50W-0*) as shown in Figure 4.1. The beam is split up into two beam paths, where each is sent through an acousto-optic modulators (AOM) providing a 220 MHz frequency difference between the beams. Servo loops are used to stabilize the output power of the beams by modulating the RF power supplied to the AOMs. The two dipole laser beams are delivered to the experiment by high-power optical fibers (*PMC-1060-10-NA008-3-APC-300-P* from *NKT Photonics* and *PMC-1060-10-NA008-3-APC-300-P* from *Schäfter und Kirchhoff*).

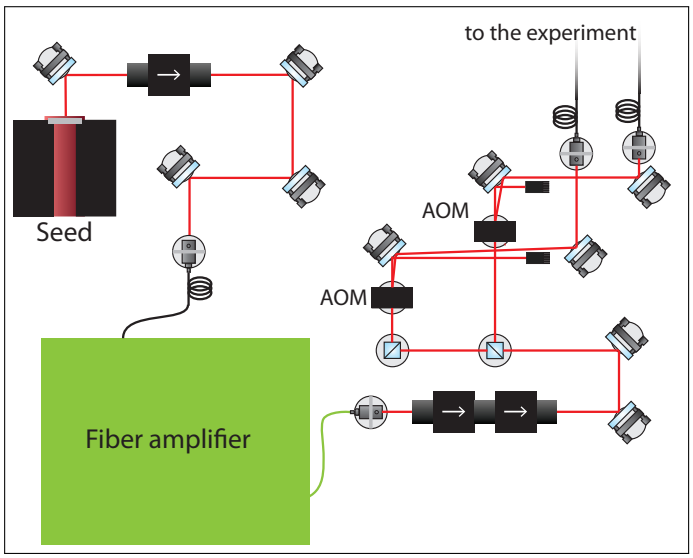

Figure 4.1.: Overview of the laser system to produce and regulate the light used for the dipole trap. Adopted from [110].

4.1.2. Recycled crossed dipole trap

The first dipole trap system is shown in Figure 4.2. It was designed to offer the widest possible temperature range of sympathetic cooling with the available dipole trap power. The light of the dipole trap beam was recycled to achieve the maximum possible trap depth. Table 4.2 shows the an overview of the system. The light is

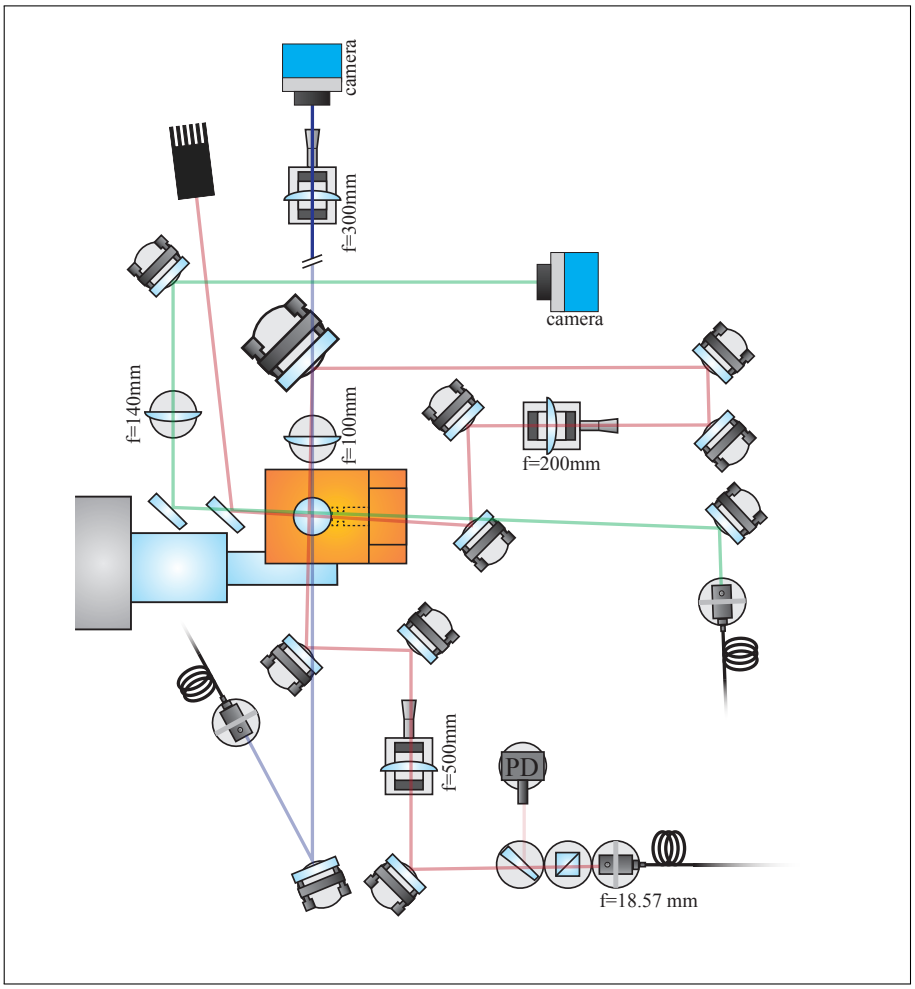

Figure 4.2.: Overview of the recycled crossed dipole trap. Shown is the dipole trapping beam in red, the main imaging beam in purple and the secondary imaging path in green. Adopted from [110].

delivered by an optical fiber and collimated by a lens with 18.57 mm focal length. A polarizing beam splitter is used as a polarization filter. A small part of the beam is directed onto a photodiode to regulate the trapping power via a servo loop and

the AOMs described in subsection 4.1.1. A lens with a focal length of 500 mm is used to focus the beam down to a waist of 168 µm. The beam is collimated on the other side of the chamber by a lens with a focal length of 100 mm and directed another time through the science chamber, perpendicular to the axis of the first beam. The polarization is turned with a half-wave plate by 90 degrees to avoid self-interference effects before the beam is focused with a lens with 200 mm focal length to a waist of 176 µm at the intersection.

The atoms are loaded into the dipole trap as follows. The QUIC trap (Ioffe coil) is decompressed in 1.2 s by ramping the current through the quadrupole coils to 15 (9) A, which moves the cloud about 1 mm further to the center of the cell. Then, the current in the trap coils is turned off over a period of 0.1 s, while the power in the dipole beams is ramped up to 6 W.

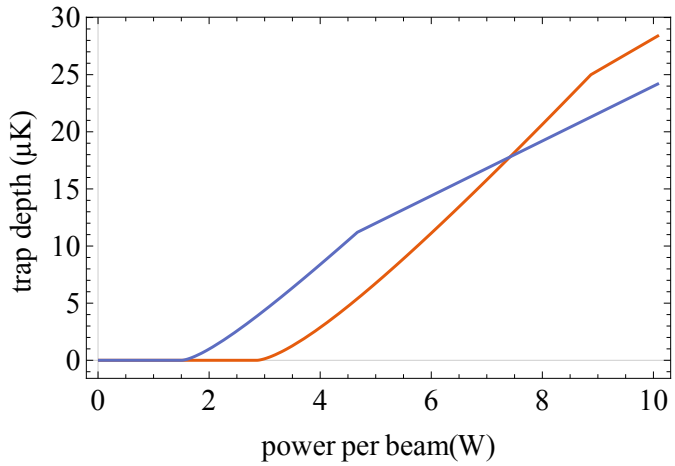

Figure 4.3.: Trap depth for ^{39}K (^{87}Rb) as blue (red) as a function of the power dipole trap beam.

The measured trapping frequencies of this trap agree with our simulations for a waist of $w_0 \approx 189$ µm and the corresponding power dependent trap depth is plotted in Figure 4.3. The discrepancy can be accounted to the beam shape after the fiber. The hexagonal structure is imprinted into the beam profile and deviates from the assumed Gaussian beam.

To achieve efficient sympathetic cooling in a dipole trap, the trap depth for the coolant has to be smaller than for the other species. In this experiment the trap depth for ^{87}Rb is smaller for powers lower than 7 W. The trap depth at this point is about 18 µK allowing for an efficient loading of the sample of up to about 2 µK. The two beam paths were overlapped using imaging systems which simplified the

Species	$\omega_{r,d}/2\pi\frac{1}{s}$	$\omega_{z,d}/2\pi\frac{1}{s}$
^{39}K	152	214
^{87}Rb	108	152

Table 4.1.: Overview of the trapping frequencies for the different species in the recycled dipole trap at a power of 16 W for a waist of 189 µm.

process significantly. A dichroic mirror that is transparent for the imaging light was used to split the imaging light it from the trapping light. Lens L_2 is simultaneously part of the imaging system.

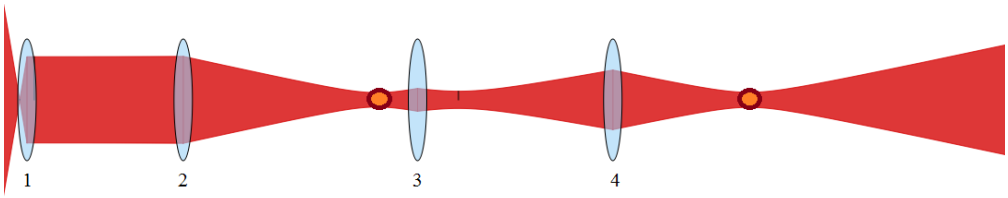

Element	Inc. Beam	L_1	L_2	L_3	L_4
Position (mm)	0	18.57	418.57	1018.57	1518.57
Focal length (mm)	–	18.57	500	100	200
Waist (µm)	6.25	1006	168	201	176
Waist Position (cm)	0	37.14	915	1123	1868

Table 4.2.: Schematic of the beam profile (top) and calculated data for the beam waists (bottom) for the recycled dipole trap. The position of the atoms is marked with orange circles.

The performance for sympathetic cooling is shown in Figure 4.4. The dual species sample was prepared and the trap depth was lowered by ramping down the dipole trap power resulting in an evaporative cooling of rubidium. The temperature of the two species was determined after rethermalization in time-of-flight. The temperature of the ^{39}K sample follows the temperature of the ^{87}Rb for a wide range. At a power of 3.5 W the samples stop being in thermal equilibrium due to a vertical displacement of the samples in the trap caused by gravity. This differential gravitational sag ultimately prevented the achievement of dual condensation in this trap. However it was possible to obtain the results in subsection 4.1.4 and section 4.4.

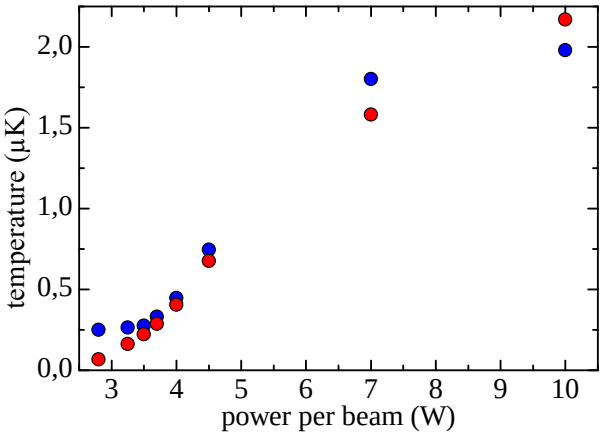

Figure 4.4.: Temperature of ^{39}K (blue) and ^{87}Rb (red) as a function of the dipole trap power.

4.1.3. Two beam crossed dipole trap

The design of the recycled dipole trap did not allow for a dual condensation due to insufficient rethermalization caused by the gravitational sag. By decreasing the waist of the trapping beams the overlap can be increased but at the same time the range for efficient sympathetic cooling seen in Figure 4.3 and Figure 4.6 becomes smaller since the point of equal trapping depths for ^{39}K and ^{87}Rb scales with $U_{Cross}/w = 0.091\,\frac{\mu K}{\mu m}$ [133]. To simplify the design and operation, the trap design consists of two independent beams as illustrated in Figure 4.5.

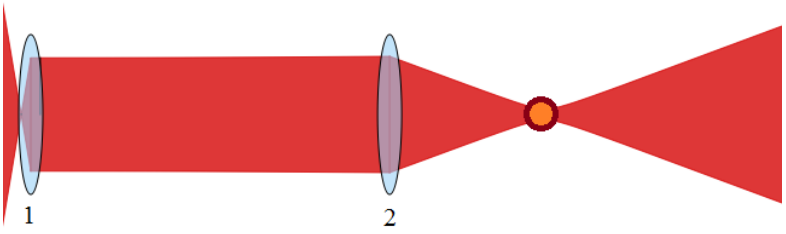

	MFD (µm)	f_1(mm)	f_2 (mm)	waist (µm)
1st axis	13.5	18.57	300	100
2nd axis	10	30	600	100

Table 4.3.: Schematic of the beam profile (top) and calculated data for the beam waists (bottom) for the two beam dipole trap. The position of the atoms is marked with an orange circle.

The first beam is delivered by a high power fiber (*PMC-1060-10-NA008-3-APC-300-P* from *Schäfter und Kirchhoff*) focused by a lens with a focal length of 600 mm. The light for the second beam is delivered by a high power fiber (*PMC-1060-10-NA008-3-APC-300-P* from *Schäfter und Kirchhoff*) and a lens with 300 mm focal length to focus the beam. The two beams are aligned perpendicular to each other in the horizontal plane and are both focused to waists of 100 µm at the location of the atoms.

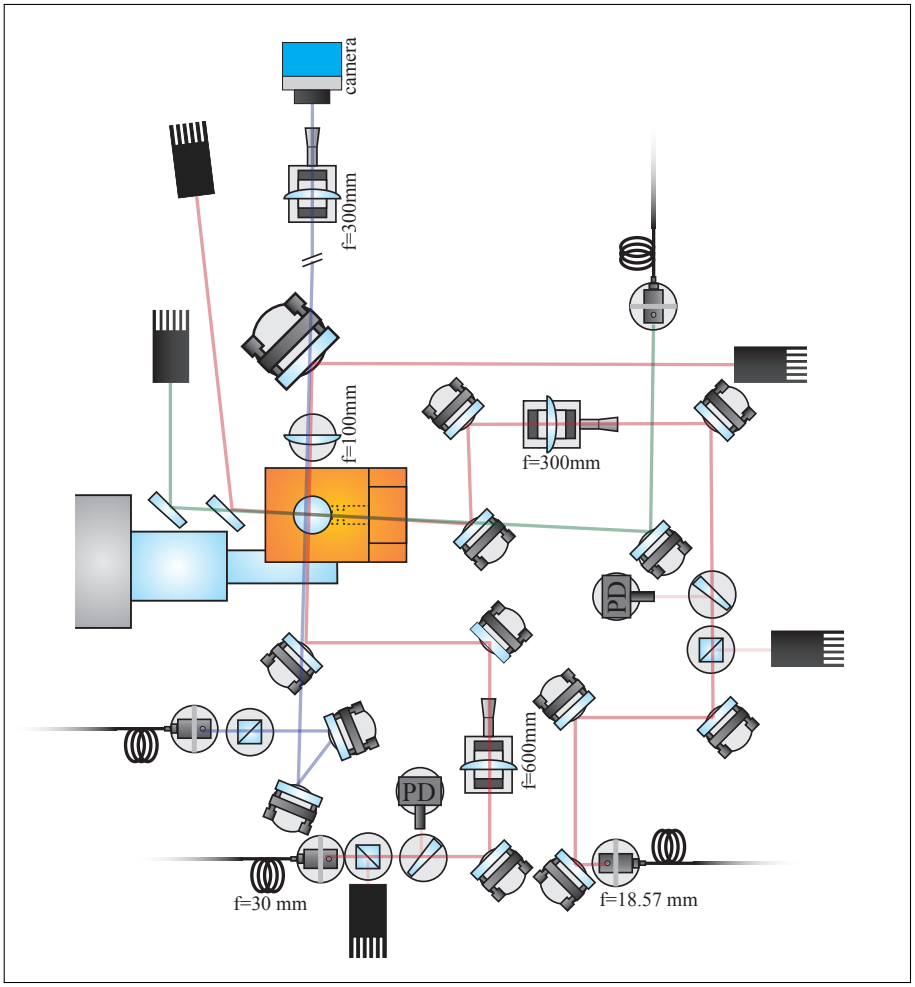

Figure 4.5.: Overview of the two beam crossed dipole trap. Shown is the dipole trapping beam in red, the imaging beam in purple and the secondary imaging path in green. Adopted from [110].

Figure 4.6 shows the depth of the dipole trap depending on the beam power. Assuming a rethermalized ensemble, a number of 200 000 ^{39}K atoms and an $\eta = 3$,

where η denotes the ratio of the trap depth to the sample temperature of ^{87}Rb, the point for the formation of a ^{39}K BEC is corresponding to a dipole beam power of 0.55 W and is marked by the vertical dashed line. Here, the immersion is defined by the Bhattacharyya distance of two Gaussian distributions representing the density function of the two species. The waist was chosen such that the immersion of ^{39}K in ^{87}Rb is sufficient to ensure thermalization at this point.

The crossing point between the depths for ^{39}K and ^{87}Rb at 10 µK allows for efficient loading of atomic samples at temperatures up to 1 µK. Compared to the recycled dipole trap, evaporation above 1.1 W primarily leads to loss of the minority species, since the trap depth is smaller for potassium than for rubidium, which is contrary to the aim of sympathetic cooling. Below 1.1 W sympathetic cooling of potassium with ^{87}Rb can work efficiently.

The atoms are loaded into the dipole trap as follows. First the QUIC trap is decompressed in 1.2 s by ramping the current through the quadrupole coils to 15 A and the Ioffe coil to 9 A. The cloud moves about 1 mm further to the center of the cell and cools to a temperature of 400 nK. Then, the current in the trap coils is linearly turned off over 1 s, while the power in the two dipole beams is ramped up to 0.9 W.

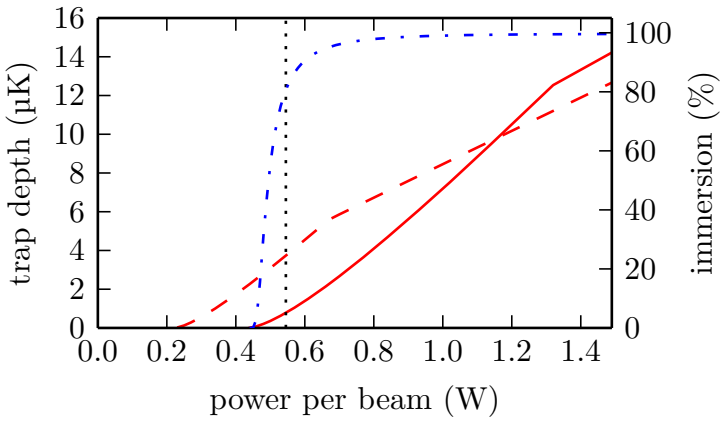

Figure 4.6.: Trap depth for ^{39}K (^{87}Rb) as red dashed (straight) dependence on beam power. In blue the calculated immersion of the ^{39}K into the ^{87}Rb coolant. The vertical black line shows the calculated critical trap depth for condensation of potassium with $N = 200\,000$ atoms and $\eta = 3$

At the end, 4×10^5 ^{39}K atoms and 4×10^6 ^{87}Rb atoms with a temperature of 1 µK are loaded into the dipole trap, corresponding to a phase-space density of 0.1

and 0.5 respectively (see Figure 4.20).

Considering a mixture of ^{41}K and ^{87}Rb the general overlap problem is similar but smaller due to the lower mass difference. Using this scheme about 2.5×10^5 ^{41}K atoms and 4×10^6 ^{87}Rb atoms at a temperature of 1.5 µK can be loaded into the dipole trap corresponding to a phase space density of $3{\times}10^{-2}$ and $5.5{\times}10^{-3}$ (see Figure 4.22).

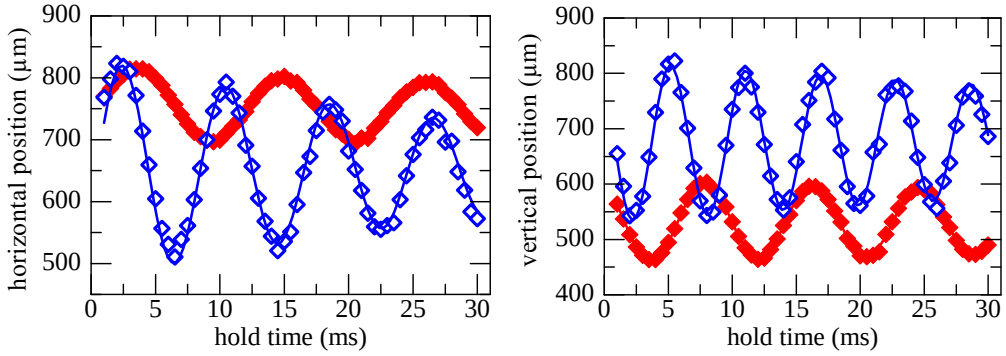

Figure 4.7.: Measurement of the trapping frequencies of the two beam dipole trap for a power of 900 mW per beam for ^{87}Rb (closed) and ^{41}K (open). The measured trapping frequencies are $\omega_r/2\pi = 89.4\ (124)$ 1/s and $\omega_z/2\pi = 119\ (170.5)$ 1/s for ^{87}Rb (^{41}K). The difference in position is caused by a different time of flight.

Species	$\omega_{a,Q}/2\pi\frac{1}{s}$	$\omega_{r,Q}/2\pi\frac{1}{s}$	$\omega_{h,d}/2\pi\frac{1}{s}$	$\omega_{z,d}/2\pi\frac{1}{s}$
^{39}K	20.2	65.9	142	199
^{41}K	19.7	64.4	138	194
^{87}Rb	13.5	44.1	102	139

Table 4.4.: Overview for the different species of the trapping frequencies in the expanded QUIC ω_Q and for a dipole trap at a power of 1.1 W ω_d.

4.1.4. ^{87}Rb BEC in the crossed dipole trap

To produce a ^{87}Rb BEC in an optical potential the cloud is pre-cooled in the magnetic trap. The evaporation in the QUIC trap is stopped at a temperature of around 1.5 µK before loading the atoms into the recycled crossed dipole at a power of 10 W. The evaporation is performed by ramping down the dipole trap

power in three linear ramps to 2.9 W in 8.2 sec. At this point condensation sets in and almost pure condensates can be produced as shown in Figure 4.8.

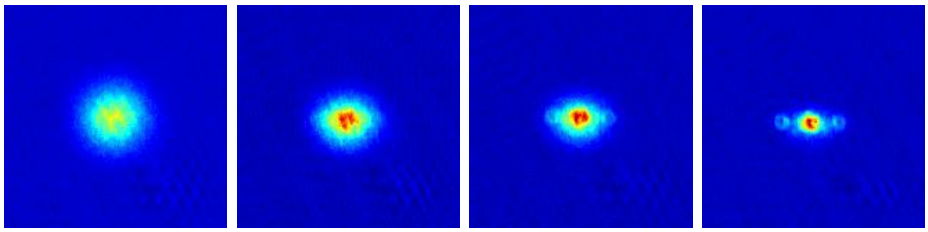

(a) $T \approx 110\,\mathrm{nK}$ (b) $T \approx 65\,\mathrm{nK}$ (c) $T \approx 35\,\mathrm{nK}$ (d) $T \approx 20\,\mathrm{nK}$

Figure 4.8.: Emergence of a ^{87}Rb-BEC from the thermal cloud while lowering the temperature. The images are taken after release from the recycled dipole-trap and temperatures are given for the thermal component.

The performance of the whole evaporative cooling process is shown in Figure 4.9 and the efficiency of the evaporation corresponding to the definitions in Equation (3.10) is found to be $\gamma \approx 2.79$. The BEC contains more than 5×10^4 atoms, which is lower than in the following dual species experiments. It can be accounted to the low trapping frequencies and thus with an inefficent rethermalization during the evaporation. As shown in Figure 4.8 the images of the coldest clouds feature two side maxima. These can be accounted to an unwanted reflection in the optical beam path. The reflection forms a standing wave in the trap corresponding to a weak one dimensional optical lattice. This effect is unwanted and one of the reasons this trap was replaced.

4.2. State preparation

To the control the internal states of the samples, microwave (MW) and radio-frequency (RF) radiation is used. As explained in section 3.4, MW radiation is used to drive the transitions from the $|2,2\rangle$ to the $|1,1\rangle$ state in ^{87}Rb. The required frequency is roughly equal to the hyperfine splitting of ^{87}Rb and thus around 6835 MHz [71]. To prepare the hyper fine state in potassium frequencies of about 461.7 MHz for ^{39}K and 254.0 MHz for ^{41}K are needed [70]. The magnetic sub-states have a field dependence of 700 kHz/G and thus require RF-radiation in the range of 1-150 MHz to address transitions between them.

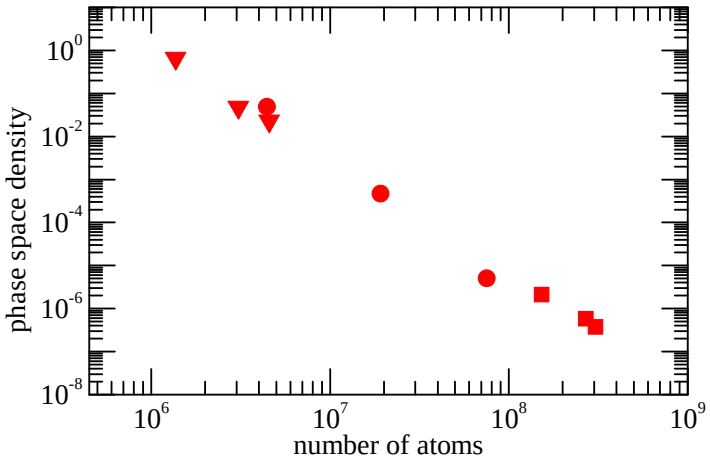

Figure 4.9.: Phase space density during the cooling process as a function of the number of atoms for ^{87}Rb in the quadrupole trap (squares), QUIC trap (circles) and the dipole trap (triangles).

4.2.1. Radio frequency system

The system to generate RF-radiation is shown in Figure 4.10. For the frequency range of 1-150 MHz the signal is generated by an arbitrary function generator (*VFG 150* from *Toptica photonics*). This arbitrary function generator allows for the generation of short pulses as well as longer sweeps. Since the wavelength of a signal with 10 MHz is about 30 m, an antenna with a length close to the wavelength is not feasible. Instead a smaller loop antenna is used which is driven by an amplifier delivering up to 15 W of RF power. For the manipulation of potassium the signal is generated by a frequency synthesizer (*2024* from *Marconi*). The signal is amplified to 25 W by a power amplifier (*KU PA 041050-25A* from *Kuhne electronic*). To reduce the effects of an impedance mismatch of the antenna, the loop antenna was tuned to a resonant frequency of 470 MHz. The amplifier is protected from backwards reflections by a circulator (*B112FFF* from *Microwave Technology Corporation*) directing the reflected power into a 50 Ω terminator.

4.2.2. Microwave system

The microwave system is more complex than the radio frequency system since two frequencies have to be available at the same time in the QUIC and the generation of frequencies in the region of 6.8 GHz is not trivial. For slow frequency sweeps, needed for the evaporation and adiabatic passages, the arbitrary function generator from

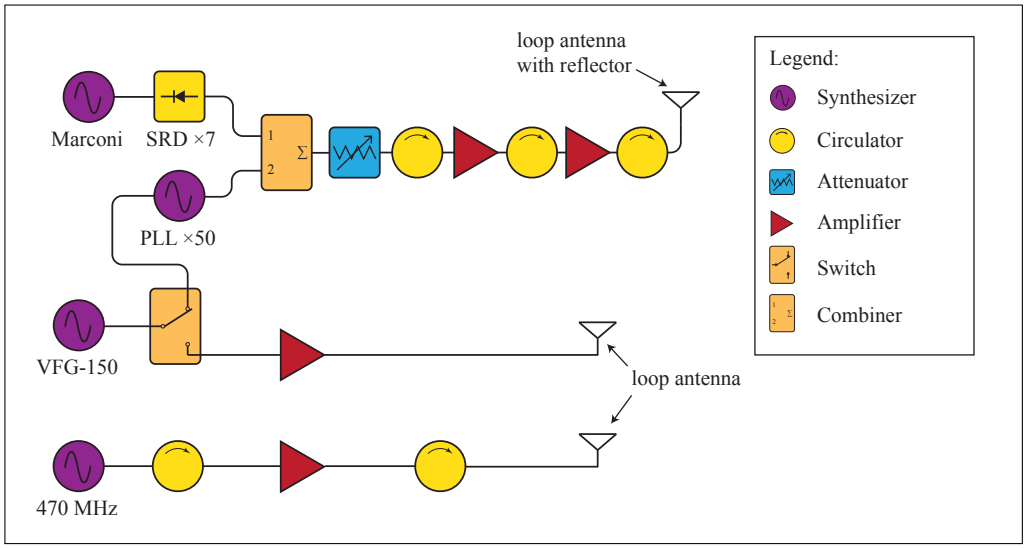

Figure 4.10.: Schematic of the MW- and RF-generation systems. Filters and On/Off-switches are not shown. Adopted from [110].

the radio frequency system (*VFG 150*) is connected to a phase locked loop (*BCO-135-145-06950-4-15P* from *Miteq*). This circuit generates the 50th harmonic of the input signal. The second signal needed to remove unwanted atoms in the wrong state during the evaporation in the QUIC is generated by driving a step recovery diode with a frequency of 1 GHz. It generates higher harmonics from which the 7th is picked using a narrow band pass filter. The driving signal is produced by a high power synthesizer (*2024* from *Marconi*). The combined signal can be regulated in power using a variable attenuator (*AT-E000-HV* from *Telemeter Electronic*). Afterwards it is amplified by a 1 W pre-amplifier and a power amplifier (*KU PA 6800 C* from *Kuhne electronic*). Both amplifiers are protected against back reflected power by circulators (*H119FFF* from *Microwave Technology Corporation*), which directs the reflected power into an 50 Ω terminator. The antenna used is an open loop with a free floating back reflector.

Methods

To address the Feshbach resonances shown in Figure 4.13 for ^{39}K and ^{87}Rb, both species have to be transferred from the $|2,2\rangle$ to the $|1,-1\rangle$ state. This is done by first transferring the samples simultaneously into the $|2,-2\rangle$ state with a rapid adiabatic passage and afterwards individually into the $|1,-1\rangle$ state. Experimentally this is done by sweeping a radio frequency from 6.0 MHz to 8.2 MHz in 2 ms at a

homogeneous background magnetic field of 10 G. The difference in the quadratic Zeeman splitting between ^{39}K and ^{87}Rb is sufficiently small at this low field. Afterwards a magnetic field of 1.8 G is applied and the ^{87}Rb atoms are transfered into the lower $|1,-1\rangle$ state using a single resonant microwave π-pulse with a duration of 6 µs. As the last step another rapid adiabatic passage transfers the ^{39}K atoms to the $|1,-1\rangle$ state by sweeping the background field from 15 G to 3.5 G while irradiating the sample with a radio frequency of 450 MHz. The different techniques for each step originate from differences in available power, frequency tunability and polarization.

For ^{41}K and ^{87}Rb the process is simplified since the $|1,1\rangle$ state for the Feshbach resonance shown in Figure 4.14 is used and thus no RF sweep is needed. First a single resonant microwave π-pulse with a frequency of 6838.5265 MHz and a duration of 6.8 µs is applied at a field of 1.8 G. To transfer the ^{41}K sample a magnetic field sweep from 85.4 G to 94.9 G within 10 ms is used. The high field leads to a larger splitting of the involved energy levels and thus a frequency of 472.33 MHz which is similar to the case of ^{39}K is used.

Magnetic field calibration

To calibrate the magnetic field strength at the position of the atoms, the transition frequency of a magnetic field dependent transition was determined. This can e.g. be an m_F changing transition such as $|1,1\rangle \rightarrow |1,0\rangle$ or hyperfine transitions such as $|1,1\rangle \rightarrow |2,2\rangle$. To determinde the field the following experiment was conducted. A cold sample of ^{87}Rb is prepared in the optical dipole trap in the $|2,2\rangle$ state. The magnetic field is ramped to a certain field and a short MW pulse close to the $|2,2\rangle \rightarrow |1,1\rangle$ transition is applied. An inhomogeneous magnetic field pulse during expansion separates the two spin components and the relative transfer is determined. This is repeated for different frequencies. A typical result is shown in Figure 4.11. After determining the center frequency of the transfer feature the corresponding magnetic field can be determined using the Breit-Rabi-formula.

Figure 4.11 shows the results for different magnetic fields. The fitted line yields a current depending slope of the magnetic field of 9.51 G/A with an offset of -0.21 G. The overall uncertainty of this procedure arising from the fits is better than 10 mG.

4.2.3. Hyperfine changing collisions

It is important to transfer the rubidium sample to the lower manifold first, as severe losses occur when potassium is transfered first. Figure 4.12 illustrates this

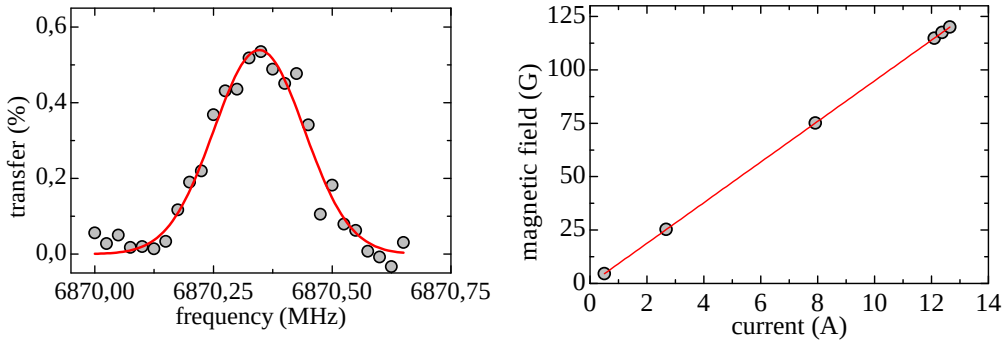

Figure 4.11.: (left) Typical spectroscopic signal used for the magnetic field calibration. (right) Magnetic field as a function of the applied current through the quadrupole coils in Feshbach configuration.

effect. When transferring ^{87}Rb before ^{39}K to the $|1,-1\rangle$ state, lifetimes on the order of 40 sec are observed. This is sufficient for the production of BECs in the dipoletrap. However if only ^{87}Rb is transfered to the target states the lifetime is reduced to 20 ms. This lifetime is similar to the time needed for the transfer of the atoms into the ground state and thus the cooling to quantum degeneracy is not possible as relevant losses set in before the atoms can be transfered.

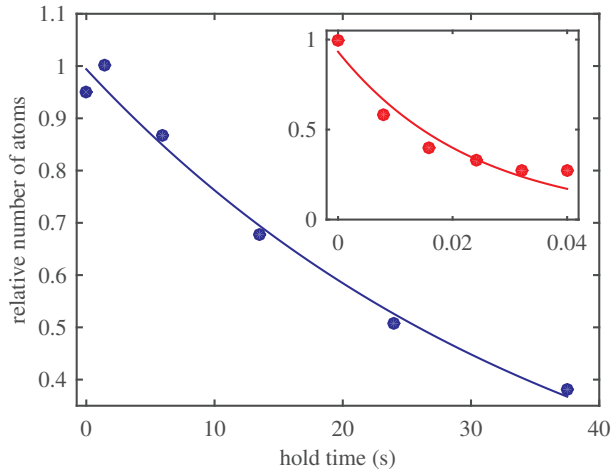

Figure 4.12.: Decay of ^{39}K in the dipole trap together with ^{87}Rb in the $|F=1,-1\rangle(|F=2,-2\rangle)$ state (inset).

This loss can be attributed to hyperfine state changing collisions between the different samples where ^{39}K and ^{87}Rb exchange the spin state and thus release the difference energy in the hyperfine energy as kinetic energy. In the case of ^{39}K and

^{87}Rb this corresponds to a temperature increase for one particle by about 0.3 K, which is not trapped anymore. In the case of transferring ^{87}Rb first this process is energetically forbidden and hence sufficiently long lifetimes for the final evaporation to produce dual-species BECs are observed. The same process holds true for a mixture of ^{41}K and ^{87}Rb and was observed in a similar experiment [27].

4.3. Tuning of the inter- and intraspecies interactions

The mixture of ^{87}Rb with either ^{39}K or ^{41}K offers a broad spectrum of accessible interspecies magnetic Feshbach resonances to tune the interaction. Besides the heteronuclear resonances ^{39}K offers multiple very broad resonances making it possible to precisely tune the intraspecies interaction of the sample. An overview of the most important available Feshbach resonances is given in Table A.1.

4.3.1. Feshbach resonances in ^{39}K

The rich Feshbach resonance structure in ^{39}K makes it an ideal candidate for experiments which require the tuning of the interaction. Especially very precise tuning capabilites are offered due to multiple broad and experimentally easy available resonances. The most important resonances for this work are in the $|1,-1\rangle$ state and shown in Figure 4.13. The resonances at 32.6 G and 162.8 G form a broad region with a positive scattering length making it possible to produce ^{39}K BECs at relatively low magnetic field strengths. Another very favorable resonance with a width of 52 G is located at 403.4 G in the $|1,1\rangle$ state [146]. Currently this resonance is not available for experiments with BECs in this experiment since the mount for the coils producing the magnetic field is made of copper. Fast switching induces Eddy-currents and thus make the fast field tuning needed to image the atoms in time-of-flight impossible. A solution would be to image at higher field with a detuned laser or the rebuild of the mount of a non conducting material.

4.3.2. Interspecies Feshbach resonances

For interspecies Feshbach resonances between ^{87}Rb and potassium the situation is different for the two different isotopes of potassium. Originally ^{39}K does not lend itself for heteronuclear experiments with tunable interactions since a magnetic

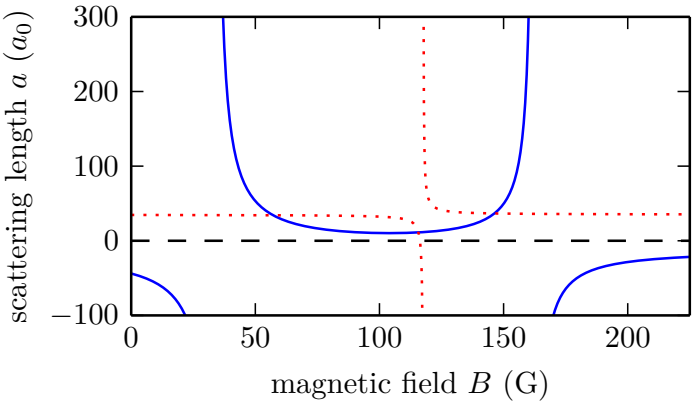

Figure 4.13.: Scattering length depending on the magnetic field for ^{39}K (blue) and between ^{39}K and ^{87}Rb (red dotted) in the $|F = 1, m_f = -1\rangle$ state.

Feshbach resonance is needed to stabilize the condensate due to the negative background scattering length. However the situation in the $|1, -1\rangle$ state allows for experiments by employing three Feshbach resonances simultaneously. Figure 4.13 shows the magnetic field dependent inter- and intraspecies scattering length. The intraspecies Feshbach resonance at 117 G [77] lies in a region where two intraspecies Feshbach resonances tune the scattering to positive values and can be assumed to be low and constant. In addition to that, this structure allows the tuning of the ^{39}K scattering while keeping the scattering length of the second component constant.

The magnetic field dependent scattering length for a mixture of ^{41}K and ^{87}Rb for the $|1,1\rangle$ state is shown in Figure 4.14 [27]. Since ^{41}K has a positive background scattering length, magnetic tuning is not required. The broad resonance at 35.2 G allows for precise tuning of the interspecies scatter length. Unfortunately the scattering length at this Feshbach resonance can not be tuned between $0\,a_0$ and about $600\,a_0$. Another Feshbach resonance at 78.6 G closes this gap.

Characterisation of a heteronuclear Feshbach resonance

Most experiments on heteronuclear mixtures rely on the precise tuning of the interspecies interaction strength. The experiments described in subsection 4.7.2 and chapter 5 rely on the precise knowledge of the ^{39}K-^{87}Rb interspecies scattering length in the vicinity of the interspecies Feshbach resonance shown in Figure 4.13. This resonance was extensively studied within a larger survey of Feshbach resonances [77].

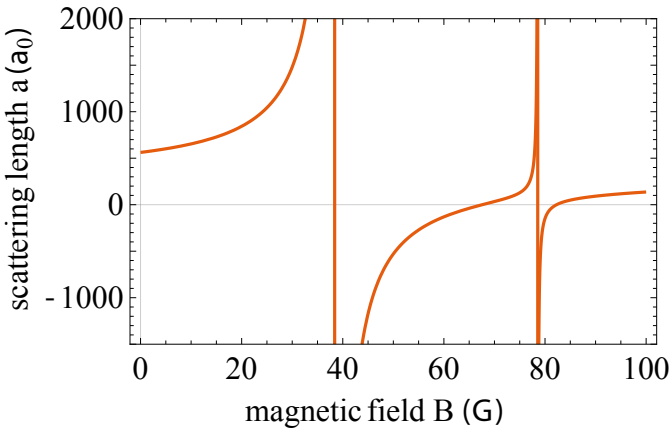

Figure 4.14.: Scattering length depending on the magnetic field for ^{41}K and ^{87}Rb in the $|F = 1, m_f = 1\rangle$ state.

However, the precision of the resonance position was not sufficient and the width was only known from theoretical calculations. Hence a precise measurement of the Feshbach resonance parameters is required.

To determine the position of the center of the Feshbach resonance, the three-body loss coefficient α was recorded around the center of the Feshbach resonance. This method has previously been used and shown a higher precision than simple loss measurements [55]. Here mixed samples with temperatures of about 150 nK and 1×10^5 ^{87}Rb and 2×10^4 ^{39}K atoms were used. The general concept of three-body losses is described in subsection 2.2.2. While a simplified analysis for the performed experiments of determining the Feshbach resonance position is sufficient here, a more elaborated method is described in chapter 5. Since the absolute precision of the value of α_{RbRbK} is not relevant in first order a simpler procedure than the one in chapter 5 is used. We consider only processes where two ^{87}Rb and one ^{39}K atom is lost and neglect all others. Thus we can describe the loss process by the following three coupled differential equations.

$$\frac{dN_{Rb}}{dt} = -\frac{2}{3}\alpha_{RbRbK}\eta_{RbRbK}N_{Rb}^2 N_K, \tag{4.3}$$

$$\frac{dN_K}{dt} = -\frac{1}{3}\alpha_{RbRbK}\eta_{RbRbK}N_{Rb}^2 N_K, \tag{4.4}$$

$$\frac{dT}{dt} = \frac{1}{3}\frac{\alpha_{RbRbK}}{N_{Rb}+N_K}\eta_{RbRbK}N_{Rb}^2 N_K T, \tag{4.5}$$

with α_{RbRbK} being the three-body loss coefficient [38, 55, 91, 147]. The dual species

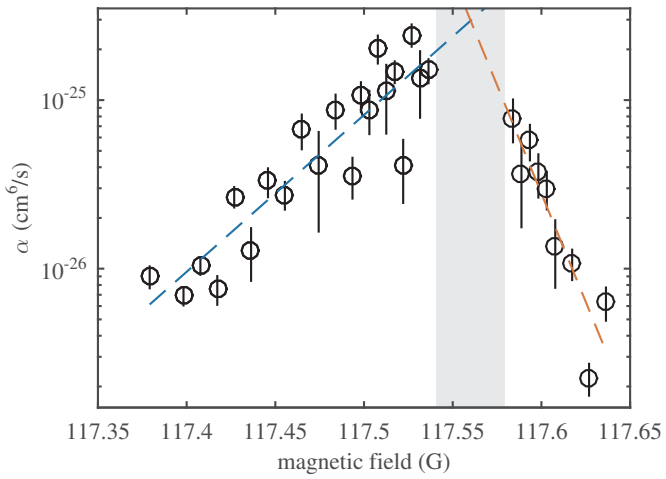

Figure 4.15.: Three-body recombination rate close to the Feshbach resonance at 117.56 G, with fits to either side of the data. A region of fast decay in the center of the resonance was excluded.

pre-factor η_{RbRbK} is defined as

$$\begin{aligned}\eta_{RbRbK} &= \int n_{Rb}^2 n_K dr \\ &= \left(\frac{\pi k_B}{T_{Rb}^2 T_K}\right)^{3/2} \gamma_{Rb}^2 \gamma_K \\ &\cdot \left(\frac{m_{Rb}\omega_{x,Rb}^2}{T_{Rb}} + \frac{m_K \omega_{x,K}^2}{2T_K}\right)^{-1/2} \\ &\cdot \left(\frac{m_{Rb}\omega_{y,Rb}^2}{T_{Rb}} + \frac{m_K \omega_{y,K}^2}{2T_K}\right)^{-1/2} \\ &\cdot \left(\frac{m_{Rb}\omega_{z,Rb}^2}{T_{Rb}} + \frac{m_K \omega_{z,K}^2}{2T_K}\right)^{-1/2}\end{aligned} \tag{4.6}$$

with $\gamma_{Rb} = \left(\frac{m_{Rb}\bar{\omega}_{Rb}^2}{2\pi k_B}\right)^{3/2}$ and for potassium retrospectively. It describes the density dependent overlap of two Gaussian distributions centered at the same position. Since the samples are trapped in a dipole trap with different gravitational sags this is a simplification only valid if the size of the cloud is much larger than the gravitational sag.

We fit the resulting time dependent decay numerically to these coupled differential equations. The result is shown in Figure 4.15. A region of extremely high losses close

to the center of the resonance is excluded. Exponential functions as shown in the figure are fitted to the data and the crossing is determined. The Feshbach resonance position is thus measured as 117.56±0.02 G, where the uncertainty corresponds to the region of fast decay.

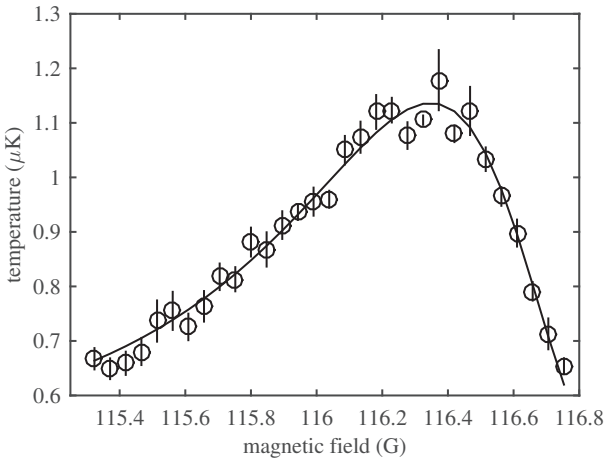

Figure 4.16.: Temperature of ^{39}K after sympathetic cooling with ^{87}Rb near the zero crossing of the interspecies scattering length and fit to the data as described in the text.

To determine the zero crossing of the Feshbach resonance a mixed sample is prepared in the dipole trap and the efficiency of the sympathetic cooling is measured. Directly after the state preparation procedure the magnetic field is set to the target value close to the zero crossing and evaporation on primarily ^{87}Rb is performed. The evaporation is stopped at 650 mW and the temperature of the ^{39}K sample is measured in time-of-flight.

Since this sample is not in a thermal equilibrium the temperature of the ^{39}K decreases exponentially depending on the interspecies cross section [148, 149]. The resulting temperature as a function of the scattering cross-section has the form

$$T(B) = T_{eq} + \Delta T e^{-\eta a_{KRb}^2}, \tag{4.7}$$

with T_{eq} being the equilibration temperature, ΔT the temperature difference between the samples, η the efficiency of the rethermalisation and a_{KRb} the interspecies scattering length [27].

Assuming the scattering length as a function of the magnetic field as in Equa-

tion (2.27) Equation (4.7) yields

$$T(B) = T_{eq} + \Delta T e^{-\eta\left(a_{bg}\left(1-\frac{\Delta}{B-B_0}\right)\right)^2}. \tag{4.8}$$

The resulting temperatures are shown in Figure 4.16. Equation (4.8) is fitted with T_{eq}, ΔT, η and Δ as free parameters. The position of the zero crossing was determined to 116.35 ± 0.025 G and the resulting width to 1.21 ± 0.045 G which is in agreement with the previous theoretical results [77].

4.3.3. Higher order Feshbach resonances

We observed multiple loss features in the ultracold mixtures of ^{41}K and ^{87}Rb in the $|1,1\rangle$ state. These were clearly separated from the expected major s-wave Feshbach resonances at 35.2 G and 78.6 G. The positions of these higher resonances are recorded by preparing a mixture of about 2×10^6 atoms of both species at a temperature of 700 nK. The magnetic field is ramped to the corresponding field and the sample and hold there for 600 ms. The samples are released from the trap and the number of the remaining atoms is determined. An overview of the position of the measured loss features is given in Table 4.5.

assignment	B_{th} (G)	B_{exp} (G)
(331)/(202)	48	48.07
(321)	52	51.67(51.76)
(112)	65	64.73
(102)	73	72.74

Table 4.5.: Overview of the observed and predicted Feshbach resonances ^{41}K and ^{87}Rb. Assignments of the quantum numbers $(fm_f l')$ are taken from [150].

These features can be accounted to higher order Feshbach resonances. The coupling between open and closed channel described in subsection 2.2.1 can be accounted to dipolar relaxation and spin exchange [79]. Incoming atom pairs with a non vanishing angular momentum l have been neglected in the discussion so far. This is due to the fact that for $l > 0$ this gives rise to a centrifugal barrier with a height proportional $l(l+1)$ and higher order partial waves are suppressed (see Equation (2.22)). Taking these collisions into account gives rise to new resonances characterized by the closed channel bound state orbital angular

momentum quantum number l_c. Similar to the naming of atomic orbitals, the resonances with $l_c = 0$ are called s-wave resonances, while resonances with $l_c = 1$ are p-wave and $l_c = 2$ d-wave resonances respectively. The position of the observed features have been theoretically predicted and partially observed [150]. However the features at 51.7 G, 65 G and 73 G have not been observed before. The loss feature around 51.7 G is shown in Figure 4.17 and shows the characteristic double structure of a p-wave resonance [151].

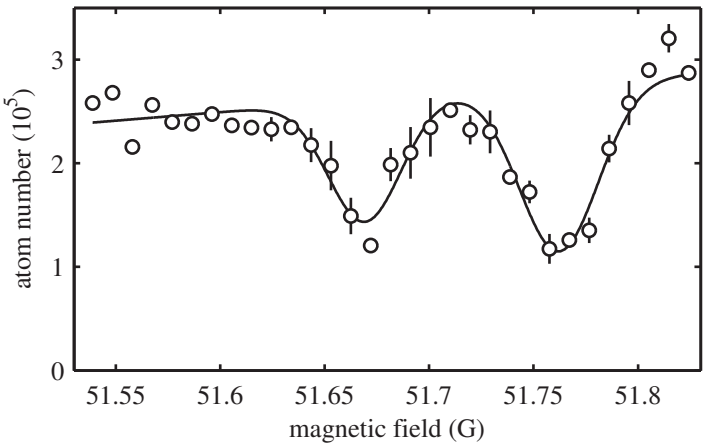

Figure 4.17.: Example of the double structure of a p-wave Feshbach resonance between ^{41}K and ^{87}Rb.

4.4. ^{39}K BEC in the recycled optical dipole trap

The production of quantum degenerate samples of ^{39}K is mmore complex than the production of ^{87}Rb BECs described in subsection 4.1.4. The experiments in this section have been performed without the positive effects of the dark-spot MOT. We start with a mixture of approximately $3 \cdot 10^8$ ^{87}Rb and $2 \cdot 10^7$ ^{39}K atoms loaded into the quadrupole trap and perform initial sympathetic cooling by evaporation of ^{87}Rb. The cooling is continued after loading into the QUIC trap to remove ^{87}Rb atoms in the $|2,1\rangle$ state (see section 3.4). To make the largest possible use of the efficient sympathetic cooling in the QUIC trap, all rubidium atoms are sacrificed in order to cool potassium. Thus all rubidium is evaporated such that we end up with a pure potassium sample containing approximately 10^6 atoms at a phase space density of 0.1 .

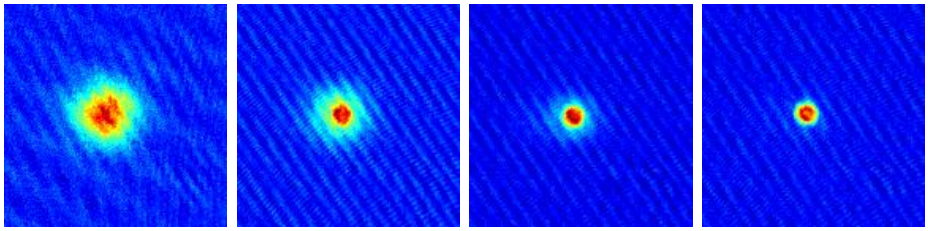

(a) $T \approx 90\,\mathrm{nK}$ (b) $T \approx 60\,\mathrm{nK}$ (c) $T \approx 30\,\mathrm{nK}$ (d) $T \approx 15\,\mathrm{nK}$

Figure 4.18.: Emergence of a ^{39}K-BEC from the thermal cloud while lowering the temperature. The images are taken 13 ms after release from the recycled dipole-trap and temperatures are given for the thermal component.

The ^{39}K sample is transfered into the recycled dipole trap (see subsection 4.1.2), which due to the large waist is highly efficient. Thus the sample stays at a constant phase space density and with no loss of atoms as shown in Figure 4.19.

Since the background scattering length of ^{39}K is negative a magnetic Feshbach resonance as shown in Figure 4.13 have to be employed. Hence the atoms are transfered to the $|1,1\rangle$ state with the methods described in section 4.2. Immediately afterwards the magnetic field strength is ramped from 40 to 60 G, corresponding to a scattering length of $100\,a_0$ to $250\,a_0$. The evaporation is done by ramping down the power in the dipole trap from 6 W to 1.8 W in 23.5 sec. Depending on the chosen value of a the evaporation length of the evaporation has to be adjusted.

Figure 4.19 shows the phase space density as a function of the number of atoms. According to Equation (3.10) the efficiency of the evaporative cooling in the dipole trap is $\gamma = 2.8$. The performance of the sympathetic cooling is analyzed in greater detail section 4.5. The transition from a thermal cloud to an almost pure BEC is shown in Figure 4.18, where we detect condensates containing more than 2×10^4 atoms. Due to insufficient repumping, while this experiment was performed, this value is very likely too low. Comparison of the detection efficiency yielded a mismatch of a factor of about two, thus the number of atoms in th BEC is approximately 4×10^4 atoms.

4.5. ^{39}K -^{87}Rb dual-BEC in the optical dipole trap

Since ^{39}K has a negative background scattering length it needs to be tuned in the final evaporation steps before dual condensation by employing magnetic Feshbach

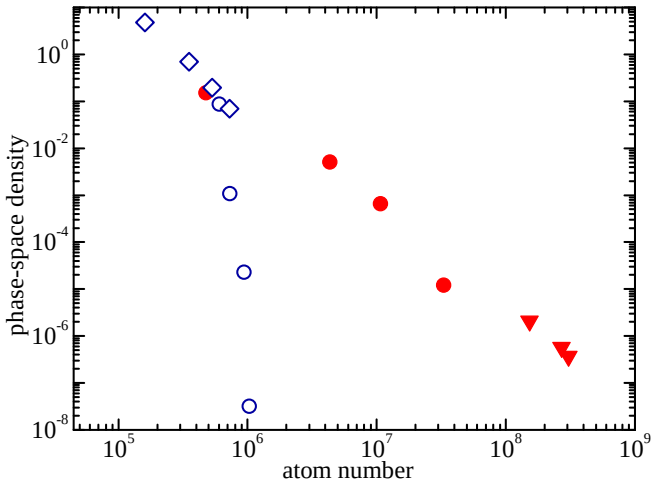

Figure 4.19.: Phase space density during the cooling process as a function of the number of atoms for ^{39}K (^{87}Rb) in blue (red) in the quadrupole trap (triangles), QUIC trap (circles) and the dipole trap (diamonds).

resonances. Figure 4.13 shows the magnetic field dependent scattering length. Stable ^{39}K condensates have been produced in the entire region between the two intraspecies Feshbach resonances. For practical purposes it is favorable not to chose a field close to the interspecies Feshbach resonance at 117.56 G. The experimental adjustments for the change in scattering length proofed to be minor. A typical sequence produces dual-species BECs at 142.5 G to increase the collision rates which allows to shorten the evaporation sequence.

After pre-cooling in the QUIC-trap the final sympathetic cooling sequence is performed in the two beam optical dipole trap. After loading into the trap the magnetic field is raised to 142.5 G. At this point 4×10^6 ^{87}Rb and 4×10^5 ^{39}K atoms at a temperature of 1 µK corresponding to a phase space density of 0.5 and 0.1 are available. The evaporation is done by simultaneously decreasing the intensity in both dipole beams from 0.9 W to 480 mW in four linear ramps within 27 s. By this ^{87}Rb is evaporatively cooled while ^{39}K stays rethermalized. Figure 4.21 shows typical images of the crossing of the critical temperature. We observe the emergence of a BEC first for ^{39}K while ^{87}Rb condenses shortly afterwards. The produced BECs contain typically 4×10^4 ^{39}K and 1×10^5 ^{87}Rb atoms.

The efficiency of the evaporation is characterized according to Equation (3.10). Figure 4.20 shows the measured phase space density as a function of the number of atoms for the whole sympathetic cooling process. For the evaporation of ^{87}Rb

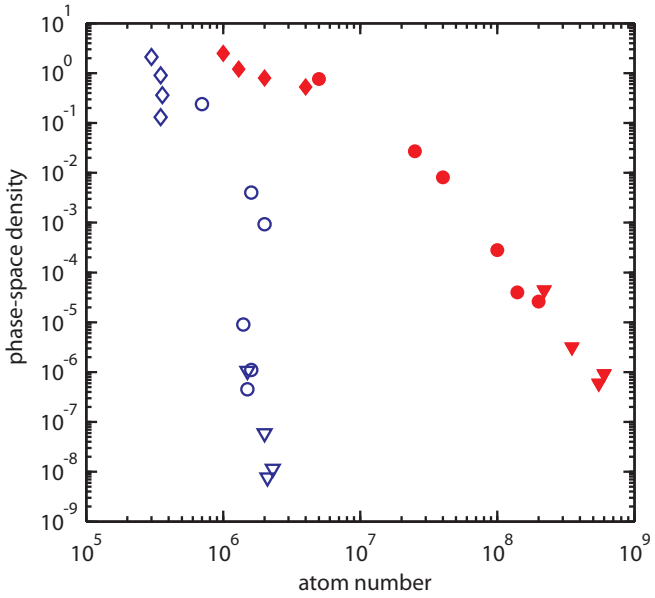

Figure 4.20.: Phase space density during the cooling process as a function of the number of atoms for ^{39}K (^{87}Rb) in blue (red) in the quadrupole trap (triangles), QUIC trap (circles) and the dipole trap (diamonds).

in the magnetic trap this yields an efficiency of $\gamma = 3.15$. For the sympathetic cooling of ^{39}K $\gamma = 18$ is measured, which demonstrates the efficiency of sympathetic cooling in the absence of strong losses. The evaporation efficiency of ^{87}Rb in the dipole trap is $\gamma = 1.5$ and for ^{39}K it is determined to $\gamma = 5.4$, which can be accounted to two reasons. The number of atoms of the different species becomes comparable and thus the sympathetic cooling with one coolant is less efficient and at the same time the temperatures close to condensation might lead to enhanced inellastic three-body collisions inducing heating and losses. However only a very small part of the evaporation is carried out in these conditions before reaching dual condensation.

The same procedure allows also for the production of pure ^{39}K BECs by removing ^{87}Rb. When the power per beam is lowered below 0.4 W, ^{87}Rb is not trapped anymore leading to a single species ^{39}K BEC.

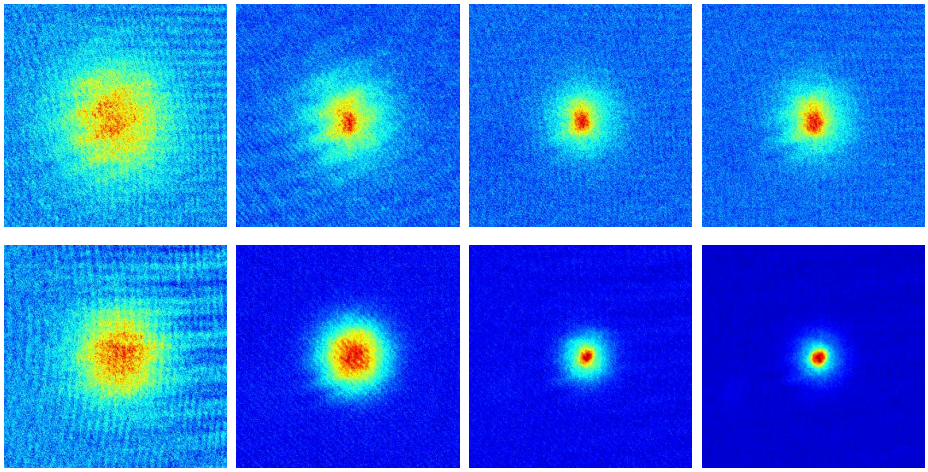

(a) $T \approx 400\,\mathrm{nK}$ (b) $T \approx 215\,\mathrm{nK}$ (c) $T \approx 100\,\mathrm{nK}$ (d) $T \approx 85\,\mathrm{nK}$

Figure 4.21.: Emergence of ^{39}K (top) and ^{87}Rb (bottom) BECs from their thermal clouds while lowering the temperature. The images are taken 14 (16) ms for ^{39}K (^{87}Rb) after release from the recycled dipole-trap and temperatures are given for the thermal component. Note that the pictures of the different species are from the same experimental run.

4.6. ^{41}K -^{87}Rb dual-BEC in the optical dipole trap

The production of ^{41}K BECs does not require the tuning of the background scattering length due to its positive value. However we start with a smaller number of atoms since we do not use enriched atom sources and the natural abundance of ^{41}K is only about 6.7 % [70]. This makes the sample susceptible to even minor loss processes. After loading the pre-cooled sample from the magnetic trap into the two beam optical dipole potential a total number of 2×10^6 ^{87}Rb and 2×10^5 ^{41}K atoms at a temperature of 2 µK corresponding to a phase space density of 0.032 and 0.007 are available. The sympathetic cooling is performed by decreasing the intensity of both beams of the two beam dipole trap simultaneously in 4 steps with a total length of 10 sec reducing the power per beam from 1.1 W to 0.43 W.

Figure 4.22 shows the emergence of the BECs from the thermal clouds. As expected the condensation of ^{41}K is observed first followed by ^{87}Rb. The produced dual species BECs contain about 4.3×10^4 ^{41}K and 3.8×10^4 ^{87}Rb atoms. Figure 4.23 shows the phase space density as a function of the number of atoms. The evaporation efficiency in the dipole trap according to Equation (3.10) yields for ^{87}Rb $\gamma = 1.9$ and for ^{39}K $\gamma = 17.5$. The higher efficiency of the evaporation can be accounted to

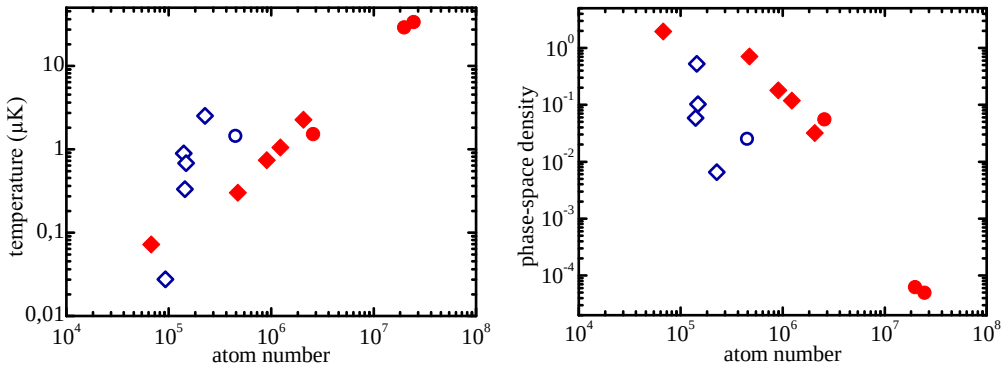

Figure 4.22.: Characterization of the sympathetic cooling in ^{41}K (blue) and ^{87}Rb (red) in the QUIC trap (circles) and the dipole trap (diamonds). (left) Phase-space density as a function of the number of atoms during evaporative cooling. (right) Temperature as a function the number of atoms.

the lower relative number of ^{41}K atoms compared to the ^{87}Rb sample.

4.7. Influence of the interaction

As seen in section 2.3 the tuning of the interaction influences the ground state and expansion behaviour of single species as well as dual species BEC mixtures in fundamental ways. The creation of ^{39}K single species BECs enable the investigation of the influence of the interaction onto the expansion dynamics, while the possibility of changing the scattering of BEC mixtures of ^{39}K and ^{87}Rb enables the observation of miscible and immiscible quantum phases.

4.7.1. Expansion dynamics

Changing the scattering length corresponds to a change of the release energy when observed in time-of-flight experiments. For the given experimental parameters, the Thomas-Fermi approximation can be used to calculate the size of the BEC σ after a long time of flight t by

$$\sigma(t) = \sqrt{\frac{2\mu}{m}}\frac{1}{\omega}, \tag{4.9}$$

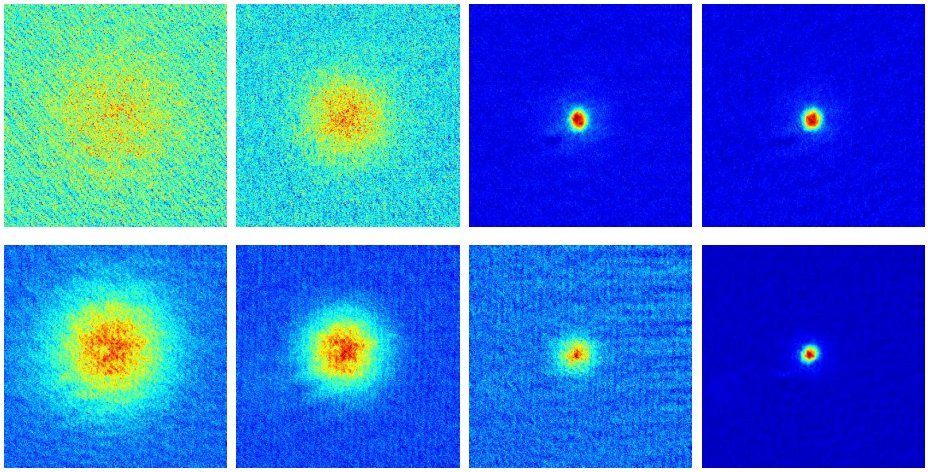

(a) $T \approx 600\,\mathrm{nK}$ (b) $T \approx 250\,\mathrm{nK}$ (c) $T \approx 80\,\mathrm{nK}$ (d) $T \approx 60\,\mathrm{nK}$

Figure 4.23.: Emergence of ^{41}K (top) and ^{87}Rb (bottom) BECs from their thermal clouds while lowering the temperature. The images are taken 14 (16) ms for ^{41}K (^{87}Rb) after release from the recycled dipole-trap and temperatures are given for the thermal component. Note that the pictures of the different species are from the same experimental run.

with m being the mass of the atoms and ω the trapping frequency [90]. The chemical potential μ is given by

$$\mu = \frac{\hbar\bar{\omega}}{2}\left(\frac{15Na}{a_{ho}}\right)^{2/5}, \tag{4.10}$$

where N is the number of atoms, a the scattering length and $\bar{\omega} = (\omega_x\omega_y\omega_z)^{1/3}$ the geometric mean of the trapping frequencies and $a_{ho} = \left(\frac{\hbar}{m\bar{\omega}}\right)^{1/2}$ the harmonic oscillator length [101].

To measure the size of the BEC as a function of the scattering length in expansion, a ^{39}K BEC was created as described in section 4.4. Afterwards the magnetic field was ramped to the target field within 1 sec in order to tune the scattering length a. The BEC was released from the trap and an absorption image was taken after 18 ms of expansion. Due to the high density of the cloud at the beginning of the expansion, the interaction will influence the dynamics. Thus the field was kept constant during the first 5 ms of time of flight. Then the magnetic field was switched of rapidly to take an absorption image. The result of this experiment is shown in Figure 4.24. The data shows good agreement with the theoretical curve (black line) following from Equation (4.10).

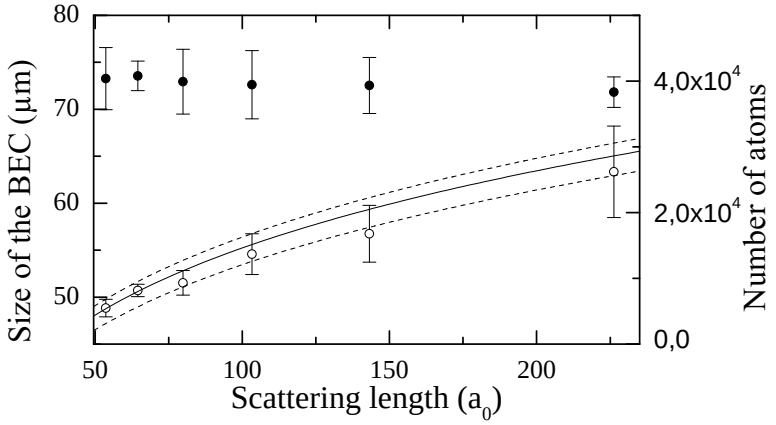

Figure 4.24.: Size of the expanded BEC depending on the scattering length (open circles) and corresponding number of atoms (closed circles). The solid line shows the theoretical expected values with the expected error due to atom number fluctuations (dashed).

4.7.2. Miscible and immiscible phases

Dual species condensates with tunable interactions allow for the investigation of interaction induced quantum phase transitions e.g. from the miscible to the immiscible phase. This transition has previously been observed in heteronuclear mixtures e.g. in ^{87}Rb-^{133}Cs [28], different spin states [152, 153], different rubidium isotopes [19] and in Bose-Fermi mixtures [154, 155]. Theoretical description of this effect has been gained [105–107] and led the development of new models to include all possible interactions within dual species samples containing thermal and condensed fractions [156].

The transition can be characterized by the miscibility parameter

$$\Delta = \frac{g_{ii}g_{jj}}{g_{ij}^2} - 1, \tag{4.11}$$

where $g_{ij} = 2\pi\hbar^2 a_{ij}(m_i + m_j)/(m_i m_j)$ is the interaction strength. The indices denote the two species with mass m and the scattering length a (see Equation 2.3.3). The phase-transition occurs at $\Delta = 0$, while negative values lead to an immiscible and positive to a miscible mixtures. The expected behavior is shown in Figure 4.25.

To characterize this behavior a dual BEC was created as described in section 4.5 on the high field side of the interspecies Feshbach resonance characterized in subsubsection 4.3.2. Afterwards the dipole trap power was ramped up to 1 W in 200 ms to compress the atomic clouds and the field was ramped to the final value

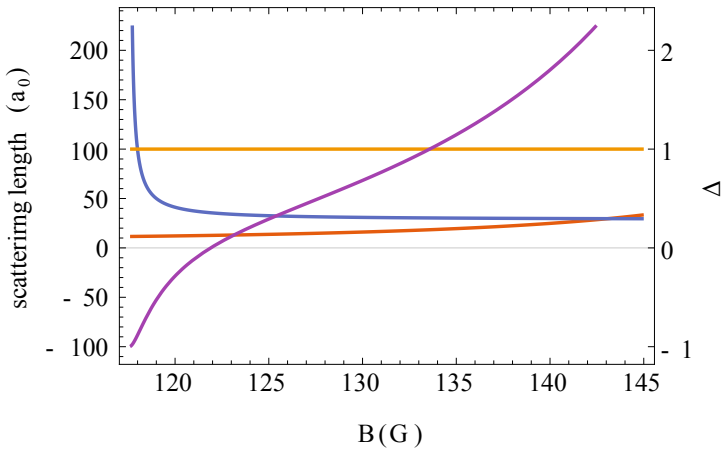

Figure 4.25.: Scattering lengths between ^{39}K-^{87}Rb (blue), ^{39}K-^{39}K (orange), ^{87}Rb-^{87}Rb (yellow) and the miscibility parameter Δ (purple) around the phase transition point. The plot assumes a background scattering length for collisions of ^{39}K and ^{87}Rb of 28.37 a_0.

in the miscible or immiscible region within 300 ms. After a hold time the sample was released and imaged after 15 (17) ms time of flight for ^{39}K (^{87}Rb). Similar to the experiments in subsection 4.7.1 the magnetic field was kept on for the first 6 ms of expansion.

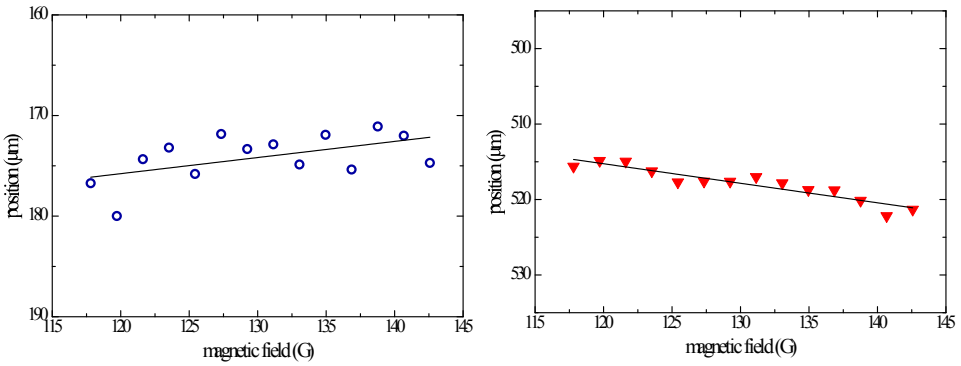

Figure 4.26.: Single species position after time-of-flight depending on the magnetic field for potassium (left) and rubidium (right). The direction of gravity in both cases is downwards.

In the miscible region density distributions, as expected for the self similar expansion from a harmonic trap, are observed. This is shown in the upper part of Figure 4.29. In the strongly immiscible case crescend-shaped density profiles are

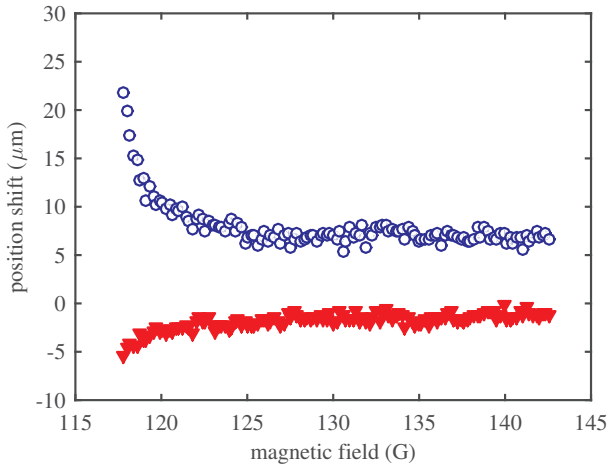

Figure 4.27.: Distance after time-of-flight of the miscible to immiscible transition for potassium (circles) and rubidium (triangles)

observed. This is shown in in the lower part of Figure 4.29, where ^{39}K gets clearly displaced above and ^{87}Rb below the initial position.

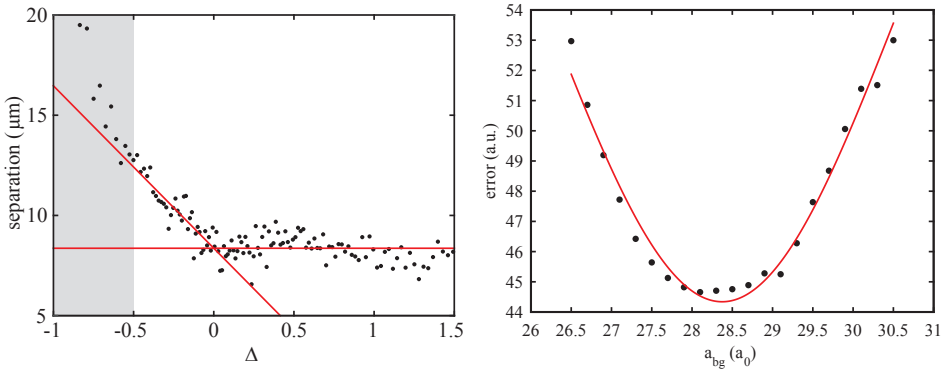

Figure 4.28.: (left) separation as a function of the miscibillity parameter Δ. Linear fits for $-0.5 < \Delta < 0$ and $\Delta > 0$. (right) Fitting error of the two linear fits depending on the value of the background scattering length a_{bg}.

To quantify this displacement the center-of-mass of the two clouds was determined according to $\mathbf{R} = \frac{1}{M}\sum_{n=1}^{i} m_i \mathbf{r}_i$. To account for shifts in position due to the different magnetic fields these results were related to the positions acquired in single species experiments shown in Figure 4.26.

Figure 4.27 shows the resulting shift in position. A clear opposite vertical shift of the position for the two species can be seen. However this shift cannot be explained by an in-trap displacement. The Thomas-Fermi radius of the two condensates are about 5.84 (6.2) µm, while the differential gravitational sag is on the order of 6.47 µm. Thus the effect must be accounted to an in-flight interaction during the expansion and a full analysis is an ongoing project.

The position of the phase-transition point can be used for a novel method to determine the interspecies background scattering length. For different trial a_{bg} the separation of the two lines is fitted versus δ. Linear dependencies are fitted to the data for $\Delta < 0$ and $\Delta > 0$. The fit error as shown on the right side in Figure 4.27 is minimized resulting in fits shown on the left side. This determines the background scattering length to be $a_{bg} = 28.37\, a_0$. This is comparable with the value predicted for the absolute magnetic ground state [77].

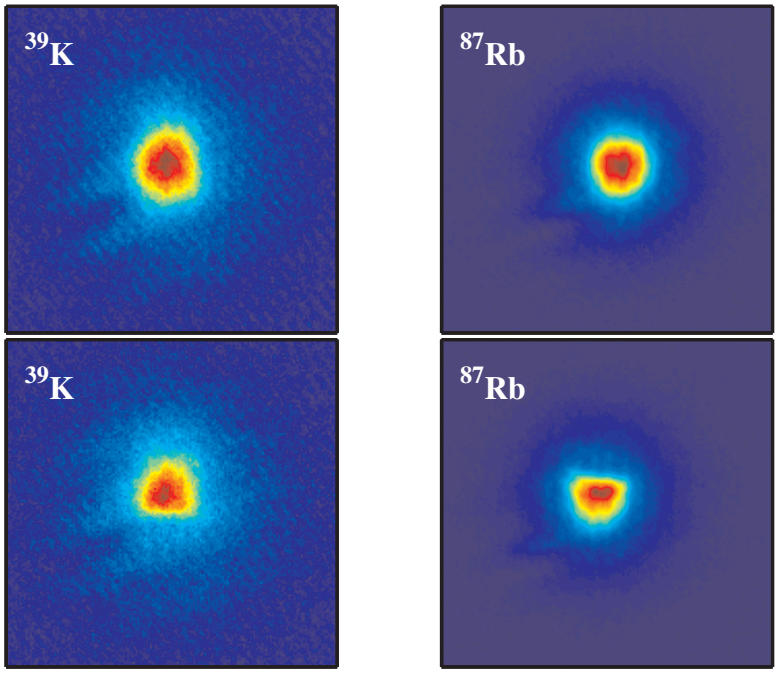

Figure 4.29.: Sample pictures of ^{39}K and ^{87}Rb (size 450 µm by 450 µm) after time-of-flight for the miscible (top) and the immiscible case (bottom).

5 Heteronuclear three-body physics

The previous chapters dealt with problems and effects that can mostly be well described and understood by means of a two body problem or with the help of a mean field approach. While a general understanding of the two body problem is widely achieved, the three-body problem offers many new effects and complications in the description despite its simplicity. A heteronuclear mixture of ultracold gases is particularly well suited for the study of effects introduced by a changing interaction due to the superior control with the help of Feschbach resonances. For this purpose intra- as well as interspecies Feshbach resonances can be employed. Especially the tuning of the interspecies interaction lends itself to the study of systems consisting of two identical and one distinguishable particle. One example from the manifold of arising effects is the Efimov effect, giving rise to three-body bound states that cannot be understood in terms of two body bound states.

In this chapter experiments on the Efimov effect in different isotope combinations of bosonic KRb mixtures are presented. It starts with a short introduction to the current dilemma of previous results and continues with a description of the data evaluation. The obtained results are presented in section 5.3 with a discussion of the limitations of the used methods in subsection 5.3.4 and a description of a more in depth analysis in subsection 5.3.5. The chapter is concluded with a discussion of the results and possible implications in section 5.4. The content of this chapter is included in a parallel manuscript [157].

5.1. Atomic Efimov resonances in ultracold gases

A classical problem in two body physics is the calculation of possible bound states. The Efimov effect predicts bound states of three atoms in parameter configurations where no two body bound state is present. This makes it an excellent example for the transition of two to few body physics.

The mixture of ^{39}K-^{87}Rb and ^{41}K-^{87}Rb offers one of the possible dream options for the theoretical analysis. It allows to study the influence of the different mass of the bosonic potassium atom on the bound states while the second species is in both cases the same rubidium isotope [32, 97].

5.2. Controversy in potassium-rubidium mixtures

While Efimov physics in mass imbalanced systems is of considerable interest for few body physics, hitherto only three different heteronuclear mixtures have been investigated. Initial experiments in a Bose-Bose mixture of ^{41}K-^{87}Rb observed both Rb-Rb-K and K-K-Rb Efimov resonances [38]. This result was controversially discussed, since the observation of the K-K-Rb resonance at $a_- = -22\,000\,a_0$ was not expected at a sample temperature of 300 nK, since this temperature corresponds to an approximate upper limit for the application of universal physics in terms of recombination rates of $a_- = -3219\,a_0$ [158]. The reported positions moreover disagreed with estimations of the three-body parameter [159] and the position of the atom-dimer resonance $a_* = 667\,a_0$ showed an unexpected scaling to the observed position of the Efimov resonance position $a_- = 246\,a_0$ of $\frac{a_*}{|a_-|} = 2.7$ while theory predicted a value of 0.52 [97]. Moreover the reported three-body recombination coefficient for a background value and on the resonance [38, 97] differed by one order of magnitude from the theoretical analysis [97]. This triggered further experiments in the Bose-Fermi mixture of ^{40}K-^{87}Rb [56, 57]. However these experiments observed no Efimov resonance and the position of the atom dimer resonance $a_* = 230\,a_0$ differed by a surprisingly large value considering the same Rb isotope and the small mass difference between the two involved K isotopes. Later experiments with the extreme mass imbalanced case of ^{6}Li-^{133}Cs allowed for the clear observation of multiple Efimov resonances and the scaling between the states [51, 52], confirming the predicted geometric scaling between the states.

Thus the case of Efimov physics in potassium and rubidium mixtures stayed

inconclusive. To date no other experimental results of Efimov physics in heteronuclear mixtures than the three mentioned are available and prompted our investigation of the ^{39}K-^{87}Rb mixture. Since these measurement yielded no sign of an observable Efimov resonance and the first experimental study of ^{41}K-^{87}Rb provided only measurements for the three-body recombination coefficient for two points, a full comparison to theoretical predictions, like the determination of the width of the resonance, was not possible and thus initiated our measurements in this isotope combination.

5.3. Experiments on Efimov resonances

The existence of an Efimov resonance is most easily detected by an increase of the three-body recombination rate α for a certain interaction strength in an ultracold gas. In ultracold atomic systems this quantity can by changed by employing Feshbach resonances and thus tuning the scattering length a. In the absence of Efimov resonances α is expected to scale with an a^4 dependence in the region of intermediate interaction strength where Efimov resonances are expected to occur. The resonances are expected to show up as an increase in α for $a < 0$ and for $a > 0$ as either an loss interference minimum or increased losses for collisions between atoms and dimers (see subsection 2.2.3). Thus we prepared a mixture of ultracold potassium and rubidium atoms, measured the remaining number of atoms and temperature of the sample for certain points in time, and calculated from the other known parameters the corresponding three-body loss coefficient α. We performed loss measurements in ultracold mixtures of ^{39}K-^{87}Rb and ^{41}K-^{87}Rb. While the measurements in ^{39}K-^{87}Rb could be performed solely on one Feshbach resonance, the measurements in ^{41}K-^{87}Rb had to be performed on two resonances to gain access to the region of $0 - 640\,a_0$.

5.3.1. Data evaluation

A typical dataset for the number of atoms and temperature is shown in Figure 5.1. We analyze the data with regard to the loss processes and heating described in Equation (2.36). We make use of the fact that three-body losses are dominated by two heavy and one light atom as predicted from theory [99, 159] and observed in ^{41}K-^{87}Rb mixtures [57]. We thus can neglect processes with two potassium and one rubidium atom and Equations (2.36) become

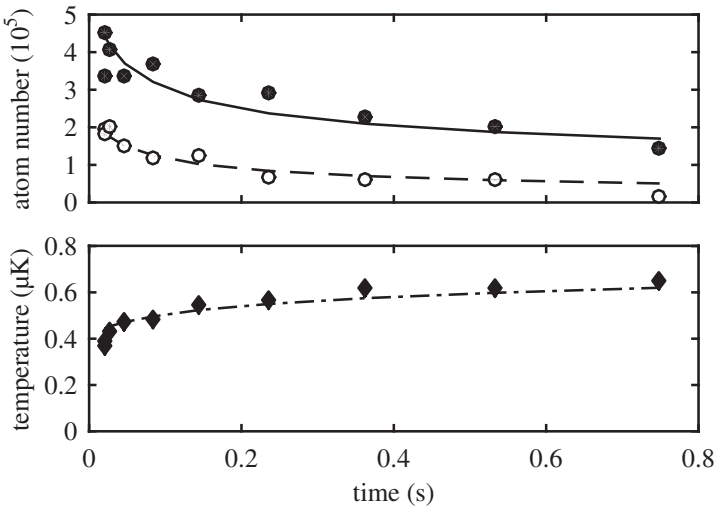

Figure 5.1.: Overview of the recorded atomic decays and heating during the hold time in ^{41}K-^{87}Rb mixtures.

$$\begin{aligned}
\dot{N_{Rb}} =& -\frac{2}{3}\alpha_{RbRbK}\,\eta_{RbRbK} N_K N_{Rb}^2 - \frac{K_{3,RbRbRb} N_{Rb}^3}{T^3} - \frac{N_{Rb}}{\tau},\\
\dot{N_K} =& -\frac{1}{3}\alpha_{RbRbK}\,\eta_{RbRbK} N_K N_{Rb}^2 - \frac{K_{3,KKK} N_K^3}{T^3} - \frac{N_K}{\tau},\\
\dot{T} =& \frac{\beta_{heat}}{3}\frac{\alpha_{RbRbK}\,\eta_{RbRbK} N_K N_{Rb}^2 T}{N_R b + N_K} + \frac{K_{3,RbRbRb} N_{Rb}^3}{3(N_{Rb}+N_K)T^2} + \frac{K_{3,KKK} N_K^3}{3(N_{Rb}+N_K)T^2}. \quad (5.1)
\end{aligned}$$

We replaced the density dependent integrals by the total number of atoms N, adjusted by a prefactor η. This takes the density dependent overlap into account to change from the density to the total number of atoms dependent rate equation. For the rise in temperature, we include the two single species and the K-Rb-Rb heating processes. Eliminating the effect of K-K-Rb processes in the interspecies term allows for the replacement of $\beta_{heat} = 3/2k_BT - \beta_{RbRbK}$. The single species processes have been extensively studied and thus the density dependent three-body rates α for ^{41}K are α_{41} =4×10^{-29} cm^6/s [121], for ^{39}K α_{39} ≈1×10^{-29} cm^6/s [49] and for ^{87}Rb α_{Rb} =3.2×10^{-29} cm^6/s [160]. The conversion factor to the atom dependent three-body factor is given by $K_{3,KKK} = \alpha_{KKK}\frac{m\bar{\omega}^2}{2\pi k_B\sqrt{27}}$ [49]. We assume the single particle losses on the order of the single species sample lifetime without enhanced interaction which was determined to τ ≈100 s. Note that each of these processes has loss rates which are at least by one order of magnitude smaller than the measured rates and thus these do not have a significant contribution to the final result.

These assumptions reduce the coupled differential equation to the fit variables α_{KRbRb}, the start temperature of the sample T_0 and the number of atoms for $t = 0$ for rubidium $N_{0,Rb}$ and potassium $N_{0,K}$, which are obtained by numerically fitting the loss curves with the equations given in Equations (5.1).

5.3.2. Loss coefficient measurements in ^{39}K -^{87}Rb

To measure the three-body loss coefficient in mixtures of ^{39}K and ^{87}Rb the time dependent decay for different scattering lengths is recorded. The interaction is controlled by exploiting the s-wave Feshbach resonance at B_0= 117.56 G in the $|1, -1\rangle$ state shown in Figure 4.13. The preparation of the samples follows the procedure described in section 4.5 for the production of BEC mixtures. For addressing the low field side of the Feshbach resonance the preparation takes place at 76 G and for the high field side at 142 G.

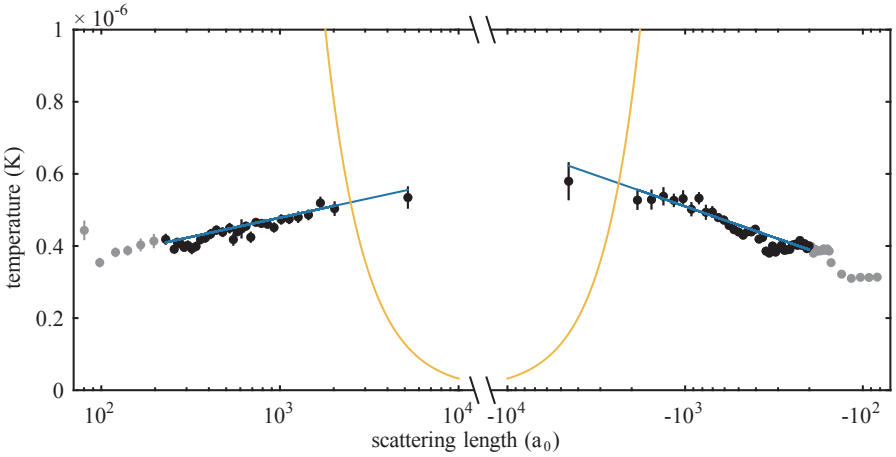

Figure 5.2.: Sample temperatures for different scattering lengths in ^{39}K-^{87}Rb (black and grey). Linear fit (blue) of the average temperatures for $|a| > 200a_0$ (black) and maximum temperature to observe an Efimov resonance (yellow).

Since non quantum degenerated samples are needed, the evaporation is stopped at a dipole trap power of 570 mW. Afterwards the trapping beams are ramped back up to a power of 800 mW per beam in 200 ms to increase the overlap corresponding to trapping frequencies of $\omega_\rho = 2\pi \times 120$ (85) Hz and $\omega_z = 2\pi \times 168$ (114) Hz for ^{39}K (^{87}Rb). We hold the samples for 500 ms before conducting the experiment to avoid effects from the compression. The produced mixtures typically containing 1.5×10^5 (4×10^5) ^{39}K (^{87}Rb) atoms at temperatures shown in Figure 5.2.

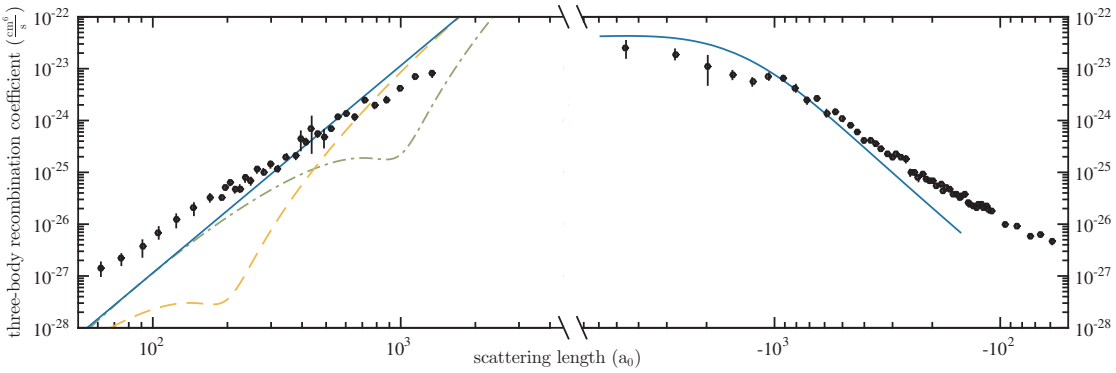

Figure 5.3.: Measured three-body recombination coefficient in ^{39}K-^{87}Rb samples. Results from the optical model [99] are shown for no observable Efimov resonances for $a < 0$ (blue). For $a > 0$ the expected a^4 dependence (blue) and possible resonance positions at $a_+ = 200\,a_0$ (yellow dashed) and $a_+ = 1000\,a_0$ (green dashed dotted) are shown.

We then abruptly change the magnetic field to the according field and wait for a variable time to record the time dependent decay. The hold times are adapted to the timescale of the decay process for different scattering lengths. Temperature and number of atoms are recorded after 14 (16) ms expansion, where we keep the target field on for the first 6 ms of expansion. The resulting curves are fitted with the procedure described in subsection 5.3.1 and the results are shown in Figure 5.3 showing no increased losses apart from the expected a^4-dependence.

5.3.3. Loss coefficient measurements in ^{41}K -^{87}Rb

The interaction dependent three-body loss coefficient in mixtures of ^{41}K and ^{87}Rb was determined on two different Feshbach resonances in the $|1,1\rangle$ state at 38 G and 79 G shown in Figure 4.14. To determine the scattering length from the magnetic field a full coupled-channel theory calculation was used [161].

We follow the preparation procedure described in section 4.6, where the evaporation in the dipole trap is performed at a field of 76 G and stopped at a power of 480 to 505 mW per beam. Afterwards the power is ramped up to 900 mW per beam corresponding to trapping frequencies of $\omega_\rho = 2\pi \times 124$ (89) Hz and $\omega_z = 2\pi \times 119$ (170) Hz for ^{41}K (^{87}Rb). For measurements on the narrow resonance at 79 G the magnetic field is at the same time ramped to a value of 66 G. Before the measurement is performed the sample is held for another 500 ms. Typical samples contain 7.5×10^4 (1.5×10^5) atoms with temperatures shown in Figure 5.4 and

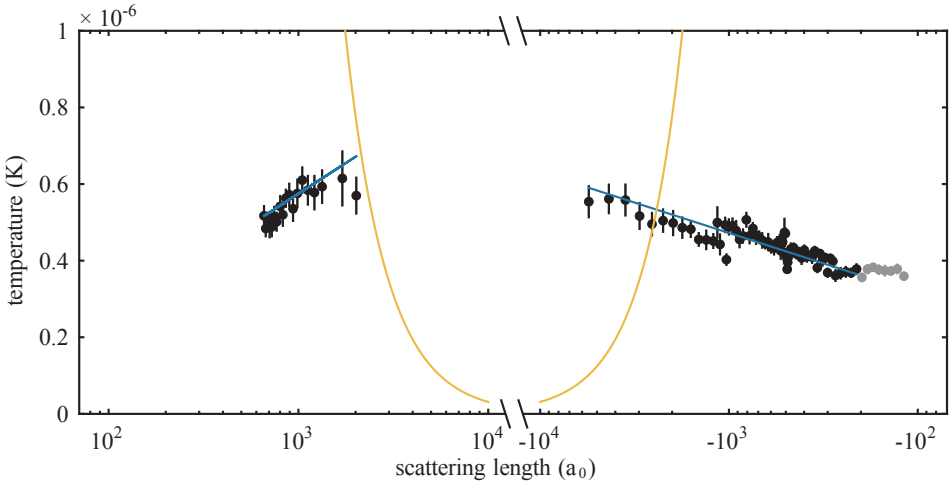

Figure 5.4.: Sample temperatures for different scattering lengths in ^{41}K-^{87}Rb around the broad resonance (black and grey). Linear fit (blue) of the average temperatures for $|a| > 200a_0$ (black) and maximum temperature to observe an Efimov resonance (yellow).

Figure 5.5. The magnetic field is then abruptly changed to the target field, where the sample is held for variable times. We adapt the hold times to the different timescales of the interaction dependent decay processes. The temperature and number of atoms are recorded after 14 (16) ms expansion, while we keep the target field on for the first 6 ms of expansion.

The obtained results are fitted with the procedure described in subsection 5.3.1 and the resulting loss coefficient is shown in Figure 5.6. We observe a prominent loss peak at around 500 a_0, which we account to a predicted p-wave Feshbach resonance [150]. As shown in subsection 4.3.3, the collisional spectroscopy around this feature (see Figure 4.17) resolves clearly the double structure associated with this type of resonances. In the course of these measurements additional collisional loss spectroscopy was performed to exclude the effect of other higher order Feshbach resonances in the results (see subsection 4.3.3).

5.3.4. Limits of detection

The range for the detection of Efimov resonances is limited by the applicability of universal physics and the unitary limit. The condition that the use of universal physics is valid for our sample, the scattering length must be larger than the physical range of interactions arising from the details of the shape of the scattering

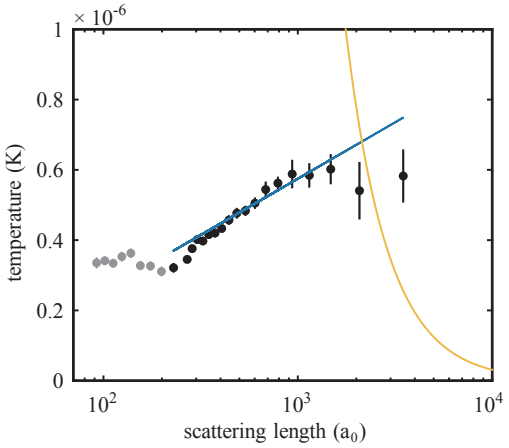

Figure 5.5.: Sample temperatures for different scattering lengths in ^{41}K-^{87}Rb around the narrow resonance (grey and black). Linear fit (blue) to the average temperatures for $|a| > 200\,a_0$ (black) and maximum temperature to observe an Efimov resonance (yellow).

potential. This range is expressed by the interatomic potential and thus the van der Waals radius R_{vdW} is a good measure. For the used mixtures of potassium and rubidium the van der Waals radius is approximately $72\,a_0$ [77, 79] and thus the lower limit is determined by $2R_{vdW} \approx 144\,\mathrm{a_0}$.

The maximal detectable loss coefficient in the unitary regime is limited by finite temperature effects. The corresponding quantity is the thermal wave vector $k = \sqrt{2\mu k_B T}/\hbar$ defining the maximum scattering length for universal physics as $k = 1/a$ [158], with μ as the reduced mass and the temperature T.

Figure 5.2 shows the scattering dependent starting temperatures recorded at the beginning of the loss measurements. A linear function is fitted to the data to take the heating during ramping to higher scattering lengths into account. The crossing point to the limit of universal physics lies for positive and negative scattering length above $2000\,a_0$ and as such only affects the two data points at highest and lowest a.

The same procedure is applied to the data of mixtures of ^{41}K and ^{87}Rb. The corresponding data is shown in Figure 5.4 for the broad resonance and in Figure 5.5 for the narrow one (see Figure 4.14). The thermal limit in these mixtures is thus determined to be above $2000\,a_0$ and thus has only an effect on the highest data point on the narrow resonance and for the datapoints well below -2500 a_0.

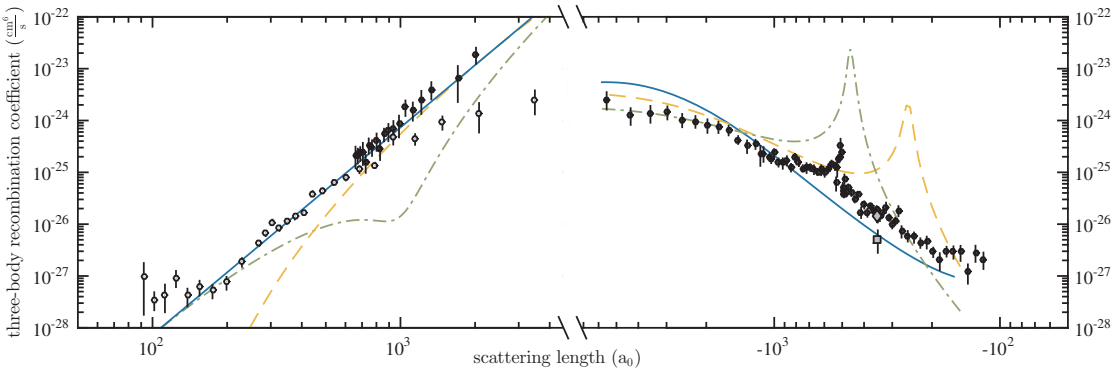

Figure 5.6.: Measured three-body recombination coefficient in ^{41}K-^{87}Rb samples. Results from the optical model [99] are shown for no observable Efimov resonances (blue) and Efimov resonances positions of $a_- = -450\,a_0$ (green dashed dotted) and $a_- = -246\,a_0$ (yellow dashed) for $a < 0$. For $a > 0$ the expected a^4 dependence (blue) and possible resonance positions at $a_+ = 200\,a_0$ (yellow dashed) and $a_+ = 1000\,a_0$ (green dashed dotted) are shown. For $a = -350\,a_0$ the measured coefficients for α_{KRbRb} (grey diamond) and α_{KKRb}(grey square) are shown.

5.3.5. Loss channel analysis

We measure the relative strength of the three-body loss coefficient by preparing more ^{41}K atoms than ^{87}Rb atoms to favor K-K-Rb losses and record the loss at an interspecies scattering length of $a = -350\,a_0$. We fit α_{KKRb} and α_{KRbRb} numerically to the model of Equation (2.36). The resulting three-body parameters are $\alpha_{KRbRb} = (1.5 \pm 0.4) \times 10^{-26}\mathrm{cm}^6\mathrm{s}^{-1}$ and $\alpha_{KKRb} = (0.5 \pm 0.2) \times 10^{-26}\mathrm{cm}^6\mathrm{s}^{-1}$, shown as grey data points in Figure 5.6, confirming the assumption from subsection 5.3.1.

Moreover we analyze the ratio of lost potassium atoms to rubidium atoms in our evaluation. The described analysis in subsection 5.3.1 relies on the assumption, that all three-body loss processes except for the K-Rb-Rb one are negligible, but since the single species recombination rates are known to good precision we only neglect the K-K-Rb recombination. This enhances certain processes during the evaluation and might suppress features showing up in a change of the ratio of lost rubidium and potassium atoms [162]. Hence Equation (5.1) is modified to allow

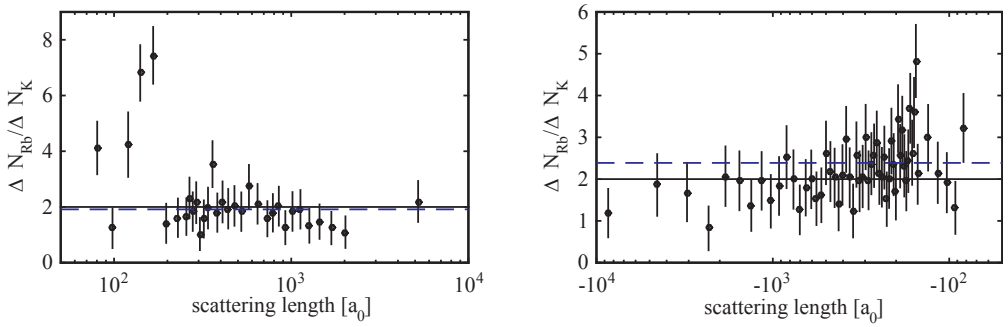

Figure 5.7.: Loss ratio different scattering lengths for samples of ^{39}K-^{87}Rb. The lines denote the expected (straight) and the measured average atom loss ratio of 1.91 for positive and 2.39 for negative scattering lengths (dashed).

for a variable ratio characterized by the loss ratio Λ and becomes

$$\dot{N_{Rb}} = -\Lambda\, \alpha_{RbKK}\, \eta_{KRb} N_K N_{Rb}^2 - \frac{K_{3,RbRbRb} N_{Rb}^3}{T^3} - \frac{N_{Rb}}{\tau}, \tag{5.2}$$

$$\dot{N_K} = -(1-\Lambda)\, \alpha_{KRbRb}\, \eta_{KRb} N_K N_{Rb}^2 - \frac{K_{3,KKK} N_K^3}{T^3} - \frac{N_K}{\tau}, \tag{5.3}$$

$$\dot{T} = \frac{\beta_{heat}}{3} \frac{\alpha_{KRbRb}\, \eta N_K N_{Rb}^2 T}{N_{Rb}+N_K} + \frac{K_{3,RbRbRb} N_{Rb}^3}{3(N_{Rb}+N_K)T^2} + \frac{K_{3,KKK} N_K^3}{3(N_{Rb}+N_K)T^2}. \tag{5.4}$$

The results for the ratio of lost atoms in the different species $\frac{\Delta N_{Rb}}{\Delta N_K} = \frac{\Lambda}{1-\Lambda}$ of the numerical fits is shown for ^{39}K-^{87}Rb is shown in Figure 5.7. The average value for positive scattering lengths is 1.91 and 2.39 for negative scattering lengths corresponding to an overall ratio of 2.15 . Except for low scattering lengths around $2R_{vdW}$ and below and thus in the relevant region it is close to the expected value of 2.

Figure 5.8 shows the loss ratio at different scattering lengths for a mixture of ^{41}K and ^{87}Rb on the broad resonance and Figure 5.9 on the narrow one respectively. The loss ratio for negative scattering lengths is determined to 1.86 and for positive scattering lengths to 2.37 on the broad resonance and 2.31 on the narrow one. This corresponds to an average loss ratio of 2.18 ^{87}Rb atoms per lost ^{41}K atom confirming the results of the previous measurement also in this isotope combination.

Although it allows for differing loss ratios, it is not useful to determine the loss coefficient with this method. The quadratic dependence on the rubidium density versus the linear dependence for the potassium density is only modified by the factor Λ, which does not describe the physical reality. However, the results are

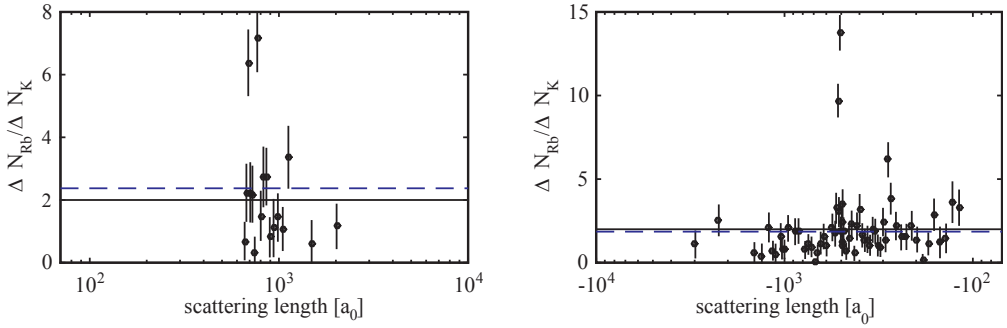

Figure 5.8.: Loss ratio for different scattering lengths for samples of ^{41}K-^{87}Rb on the broad resonance. The lines denote the expected (straight) value of 2 and the measured average atom loss ratio of 2.37 for positive and 1.86 for negative scattering lengths (dashed).

very close to the expected ratio of two and thus support the assumption of the predominant loss channels of loosing two heavy and one light atom, making further analysis in this direction obsolete.

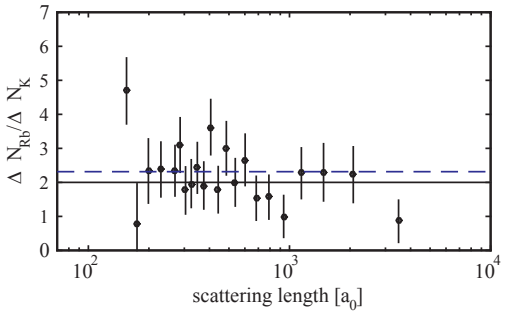

Figure 5.9.: Loss ratio for different scattering lengths for samples of ^{41}K-^{87}Rb on the narrow resonance. The lines denote the expected (straight) value of 2 and the measured average atom loss ratio of 2.31 (dashed).

5.4. Implications

We determined the three-body loss coefficient in ^{39}K-^{87}Rb and ^{41}K-^{87}Rb mixture over three to four orders of magnitude for intermediate scattering lengths. Both systems showed surprisingly no sign of an observable Efimov resonance.

Figure 5.3 shows the resulting loss coefficient as a function of the scattering length for the ^{39}K-^{87}Rb mixture. No significant deviation from the expected a^4

dependence are observed. We apply the theoretical framework from the optical model [99] to our data for negative scattering lengths for no observable Efimov resonances and to an a^4 dependence for positive scattering lengths (blue curve). The model gives the absolute value of the three-body parameter without rescaling from the input parameters and the temperature of the sample. From the good agreement with the theoretical prediction we estimate an upper limit of the overall relative uncertainty of the three-body parameter of 50 %. For positive scattering lengths the data shows good agreement to the expected a^4 dependence and no increase of the recombination coefficient connected to an atom-dimer resonance is observed. Interference minima are plotted for $a_+ = 200\,a_0$ (yellow dashed) and $a_+ = 2000\,a_0$ (green dashed dotted) and comparison shows no agreement and thus we exclude observable Efimov resonances between $2R_{vdW} = 144\,a_0$ and $1000\,a_0$ for positive and negative scattering lengths.

We determine the average loss ratio between the two species to be $\Delta N_{Rb}/\Delta N_K = 2.15$, supporting the assignment of the main loss channels in subsection 5.3.5. Moreover the loss ratio between the species shown in Figure 5.7 does not show any large systematic increase from the expected value of 2 as predicted by theory in presence of an Efimov resonance [162].

In the results for a mixture of ^{41}K and ^{87}Rb as shown in Figure 5.6 we observe a prominent peak in the scattering dependent loss coefficient at around -500 a_0 caused by a p-wave resonance. We apply the same optical model to the data as for ^{39}K with adjusted parameters and temperature for negative scattering lengths for no observable Efimov resonances and an a^4 dependence for positive scattering lengths (blue curve). From the agreement we deduce a relative uncertainty of the absolute value of the measured loss coefficient of less than 50 %. We show the same model for possible Efimov resonances at a_- =-450 a_0 as suggested by the work in ^{40}K-^{87}Rb mixtures [56]. The observed peak structure is in disagreement with the expected resonance shape of an Efimov resonance supporting the assignment of the p-wave resonance. Moreover a possible Efimov resonance peak at the earlier reported position [147] at a_- = -246 a_0 is shown. The measured loss coefficients is in disagreement with this peak. For positive scattering lengths α clearly follows the expected a^4 dependence, which was measured for scattering lengths $a > 600\,a_0$ an two different Feshbach resonances. Assumed loss minima at $a_+ = 200\,a_0$ and $a_+ = 1000\,a_0$ show no agreement and thus an Efimov loss minimum can be excluded in this region. Moreover we do not observe increased losses due to an atom-dimer resonance for any positive scattering length disagreeing with the reported position of a_* =667 a_0 [147].

The measured three-body loss coefficients differ slightly between the narrow and the broad resonance. This can be accounted for by the different preparation procedures leading to different temperatures for larger scattering lengths, thus measuring a higher three-body recombination coefficient.

The significant difference in the recombination coefficient between the different combination channels for $a = -350\,a_0$ allows to assign the main loss mechanism to events involving two rubidium atoms and one potassium atom. This is furthermore confirmed by the results from subsection 5.3.5 determining a loss ratio between the different species of $\frac{\Delta N_{Rb}}{\Delta N_K} = 2.18$ not varying significantly between the two Feshbach resonances.

In conclusion, we do not observe any increased losses at intermediate scattering lengths connected with an Efimov resonance, both in mixtures of ^{39}K-^{87}Rb as well as ^{41}K-^{87}Rb. The data shows good agreement with the predicted behavior from the optical model [99] and the results in both mixtures support the findings from the investigations done in ^{40}K-^{87}Rb [56], where no Efimov resonance was observed. From their observation of the atom-dimer resonance at $a_*^{(n)} = 230\,a_0$ universal scaling predicts the position of the Efimov resonance at $a_-^{(n)} = -55000\,a_0$ which is at a scattering length not observable for us [97]. A lower lying resonance due to universal scaling would ly at $a_-^{(n-1)} = -450\,a_0$ and was not observed and thus the observed resonance can be probably be accounted as the ground state, unless the observance of the resonance at $a_-^{(0)}$ is suppressed [163].

This possible position is close to the observed p-wave resonance peak in ^{41}K-^{87}Rb at $a = -500\,a_0$ and thus special attention was paid to excluding this option. Moreover no increase in the loss of potassium atoms was observed for the investigated region except for the p-wave resonance similar to the studies in ^{40}K-^{87}Rb [57, 162]. Our findings disagree with earlier work in ^{41}K-^{87}Rb where two resonances were found and an indication for an atom-dimer resonance was seen [147].

These results show that Efimov resonances are not observable at intermediate scattering lengths in ultracold potassium rubidium mixtures. This finding is supported by a similar unpublished experiment in mixtures of ^{41}K-^{87}Rb not observing any increased losses due to an Efimov resonance and determining the position of the atom-dimer resonance to $a_+^{(n)} = 360\,a_0$ [164].

Our findings are surprising since one would have expected an observation at similar positions than the first investigation in ^{41}K-^{87}Rb. All investigated mixtures share the same rubidium isotope and the masses only differ by a few percent for the potassium isotope [159]. Although we cannot exclude extremely narrow resonances the absence can have different reasons. The upper limit for Efimov

resonances for ^{40}K-^{87}Rb-^{87}Rb recombinations was calculated to $a_-^{(0)} < -3 \times 10^4\, a_0$ and for recombinations of ^{41}K-^{41}K-^{87}Rb to $a_-^{(0)} < -1 \times 10^6\, a_0$, which is above the investigated range [159]. Another reason could be the positive scattering length of ^{87}Rb. It was seen in experiments of ^{6}Li-^{133}Cs that in cases where the intraspecies scattering length of the heavier component was positive, the occurrence of the lowest Efimov resonance was suppressed by short range dimer states, while higher resonances were still visible [163].

6 Conclusion and Outlook

Within this thesis the first dual species BEC mixtures of ^{39}K-^{87}Rb were realized. To enable a high number of atoms in the ^{39}K condensate two intraspecies Feshbach resonances were employed to produce dual species BECs in an optical dipole trap. The position and the width of a third interspecies resonance were measured to high precision to $B_c = 117.56 \pm 0.02\,\mathrm{G}$ and $\Delta = 1.21 \pm 0.045\,\mathrm{G}$. This resonance was used to control the interspecies interaction and observe the quantum phase transition between miscible and immiscible BECs and to determine the interspecies background scattering length to $a_{bg} = 28.37\,a_0$. Moreover BEC mixtures of ^{41}K-^{87}Rb were produced and the tuning of the intra- and interspecies interaction was shown.

These mixtures were used for the investigation of few body physics with respect to Efimov physics to resolve outstanding questions of similar isotopic mixtures. The scattering dependent three-body recombination coefficient was recorded for positive and negative scattering lengths over 3 to 4 orders of magnitude for mixtures of ^{39}K-^{87}Rb and ^{41}K-^{87}Rb. Except for a peak that was assigned to a p-wave Feshbach resonance the measurements showed no sign of an Efimov resonance. The data for negative scattering length was compared to a theoretical model of the three-body loss process and showed good agreement, while the data for positive scattering lengths showed good agreement to the expected a^4 dependence. Thus it was shown that Efimov resonances are not observable in mixtures of ^{39}K-^{87}Rb and ^{41}K-^{87}Rb for intermediate scattering lengths, resolving a longstanding controversy in the field.

The reliable production of condensate mixtures as well as single species condensates with tunable intra- and interspecies interaction allow for a broad spectrum of

future experiments, some of which are presented in the following.

Few-body phyiscs

While the observation of Efimov resonances in potassium rubidium mixtures is not possible, a number of different questions can be addressed in the presented apparatus. Since multiple Efimov loss resonances on different Feshbach resonance have been observed in ^{39}K samples [49, 55] the position of the second loss resonance can be estimated to be $a_- < 22\,000 a_0$, which is experimentally accessible on various broad Feshbach resonances in ^{39}K.

Questions that could be addressed are the universal scaling between the two three-body states at different Feshbach resonances as well as the universal scaling between four and five body bound states associated to an Efimov loss resonance [46–48] by itself as well as across different Feshbach resonances.

The mixture of potassium and rubidium may be investigated further by using radio frequency association for the direct production of Efimov trimers. This is possible in homonuclear mixtures of fermions [44] and bosons [45, 165, 166] but has not been shown in heteronuclear mixtures. The direct determination of the trimer binding energy would allow for the test of theoretical predictions and indirectly provide the position of the Efimov loss resonance.

Another interesting area is three-body recombination in the non universal regime for $a \to 0$, where the interaction highly depends on the details of the scattering potential. First experiments for single species samples have been performed [167] and agree with theory [159]. However the heteronuclear case will be an interesting case to study.

Quantum gases at unitarity

The tuning of the scattering length allows for the realization of unitary quantum gases when the magnetic field is tuned to the center of a Feshbach resonance where the scattering length diverges. Thus the scattering length cannot be a characterizing quantity of the system and the sample properties solely depend on the density. Although extensively studied in fermionic gases, since the Pauli blocking suppresses losses, the bosonic case only recently attracted attention. Investigations of thermal samples of ^{39}K [168] and quantum degenerate samples of ^{85}Rb [169] showed surprisingly long lifetimes and the emergence of a steady state, since the decay was slower than the rethermalization. It would be interesting

to study if the sample can be stabilized on certain resonances in ^{39}K or by the admixture of a ^{87}Rb component.

Miscible and immiscible quantum phases

The experiments on miscible and immiscible quantum phases in this thesis provide a foundation for further investigations. The most simple experiment would be to excite a vertical oscillations of both condensates in the trap and determine the oscillation frequencies. These should show a large dependence on the miscible or immiscible behavior of the samples. Another approach is a quench through the transition between the two phases. When done nonadiabatic, interesting dynamics are expected [170]. However this might require the implementation of a quasi magic dipole trap [171] to increase the overlap of the two clouds and to compensate for the gravitational sag. At the moment a model to take all interactions between the condensed and the thermal part of the samples is under development and a collaboration is started to predict possible observations [156, 170].

Molecular physics

A wide range of experiments is possible with heteronuclear Feshbach molecules. In these experiments a Feshbach resonance is employed to associate atoms into the loosely bound dimer state [33]. These molecules are highly unstable under collisions but can be stabilized by loading them into an optical lattice to suppress collisions [172]. The reduced dimensionality would allow for a controlled study of reactive collisions with other molecules or atoms. A more elaborate investigation might aim for a transfer of these loosely bound molecules into more deeply bound states, since this give rise to a large electric dipole moment and a set of unconventional quantum phases in optical lattices is expected [173].

Impurity physics

By changing the ratio of the prepared number of atoms, one can create a small minority component in a condensate mixture acting as an impurity. The tunable interaction of the impurity with the surrounding atoms allows for the creation of polarons. This quasi particle is formed by the distortion of the surrounding medium and has been observed in ultracold Fermi gases [174, 175]. However it was not realized in Bose gases yet, though it represents a perfect model system for photons in optical media. The ability to precisely tune the scattering length

gives access to the strong coupling regime for attractive as well as for repulsive interaction. First experiments would aim to compare newly developed theories to describe the properties of this quasi particle with experimental results [176, 177]. Moreover an Efimov state, present at the same Feshbach resonance, should lead to a coupling between the two states and an avoided crossing is predicted [178].

The isotopic combinations of ^{39}K-^{87}Rb, ^{41}K-^{87}Rb and single species BECs with tunable interaction strengths are now reliably available in the presented apparatus, thus provide ideal conditions to approach these and other scientific questions in near future.

A Supplemental figures

Species a,b	$\|F_a,m_{F,a}\rangle$	$\|F_b,m_{F,b}\rangle$	B_c(G)	B_c(G)	reference
^{39}K,^{39}K	$\|1,1\rangle$	$\|1,1\rangle$	25.9	0.47	[146]
	$\|1,1\rangle$	$\|1,1\rangle$	402.4	52	[146]
	$\|1,0\rangle$	$\|1,0\rangle$	58.8	9.6	[146]
	$\|1,0\rangle$	$\|1,0\rangle$	65.6	7.9	[146]
	$\|1,0\rangle$	$\|1,0\rangle$	471	72	[146]
	$\|1,0\rangle$	$\|1,0\rangle$	490	5	[146]
	$\|1,-1\rangle$	$\|1,-1\rangle$	33.6	-55	[146]
	$\|1,-1\rangle$	$\|1,-1\rangle$	162.3	37	[146]
	$\|1,-1\rangle$	$\|1,-1\rangle$	560.7	5.6	[146]
^{39}K,^{87}Rb	$\|1,-1\rangle$	$\|1,-1\rangle$	117.56	1.21	-
	$\|1,1\rangle$	$\|1,1\rangle$	317.9	7.6	[77]
^{41}K,^{87}Rb	$\|1,1\rangle$	$\|1,1\rangle$	39	37	[27, 79]
	$\|1,1\rangle$	$\|1,1\rangle$	79	1.2	[27, 79]
	$\|1,1\rangle$	$\|1,1\rangle$	558.0	81	[77]

Table A.1.: Overview of most relevant s-wave Feshbach resonances in ^{41}K, ^{39}K and ^{87}Rb.

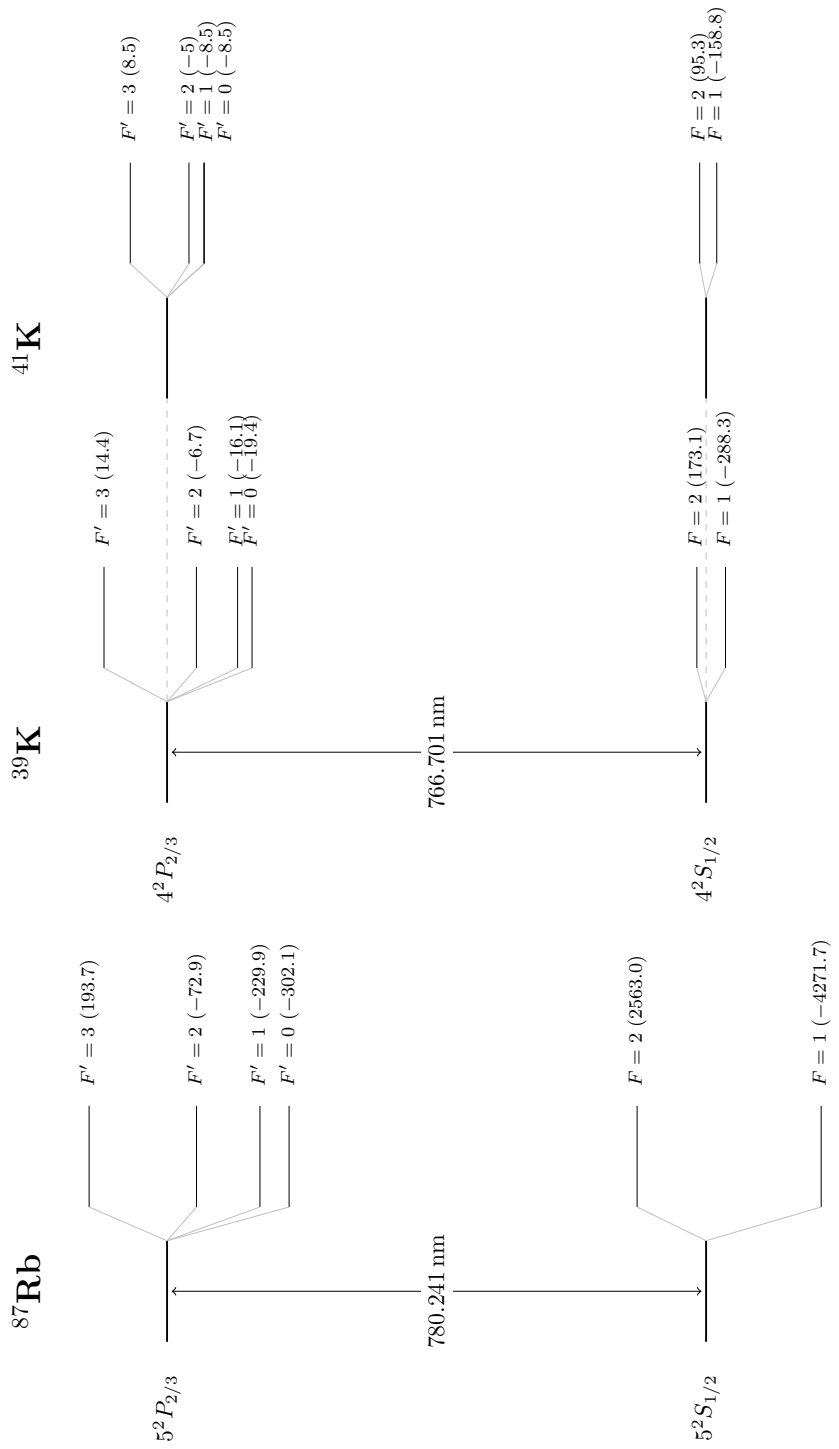

Figure A.1.: Level structure of the used alkali atoms. Adopted from [110] with data from [70, 71].

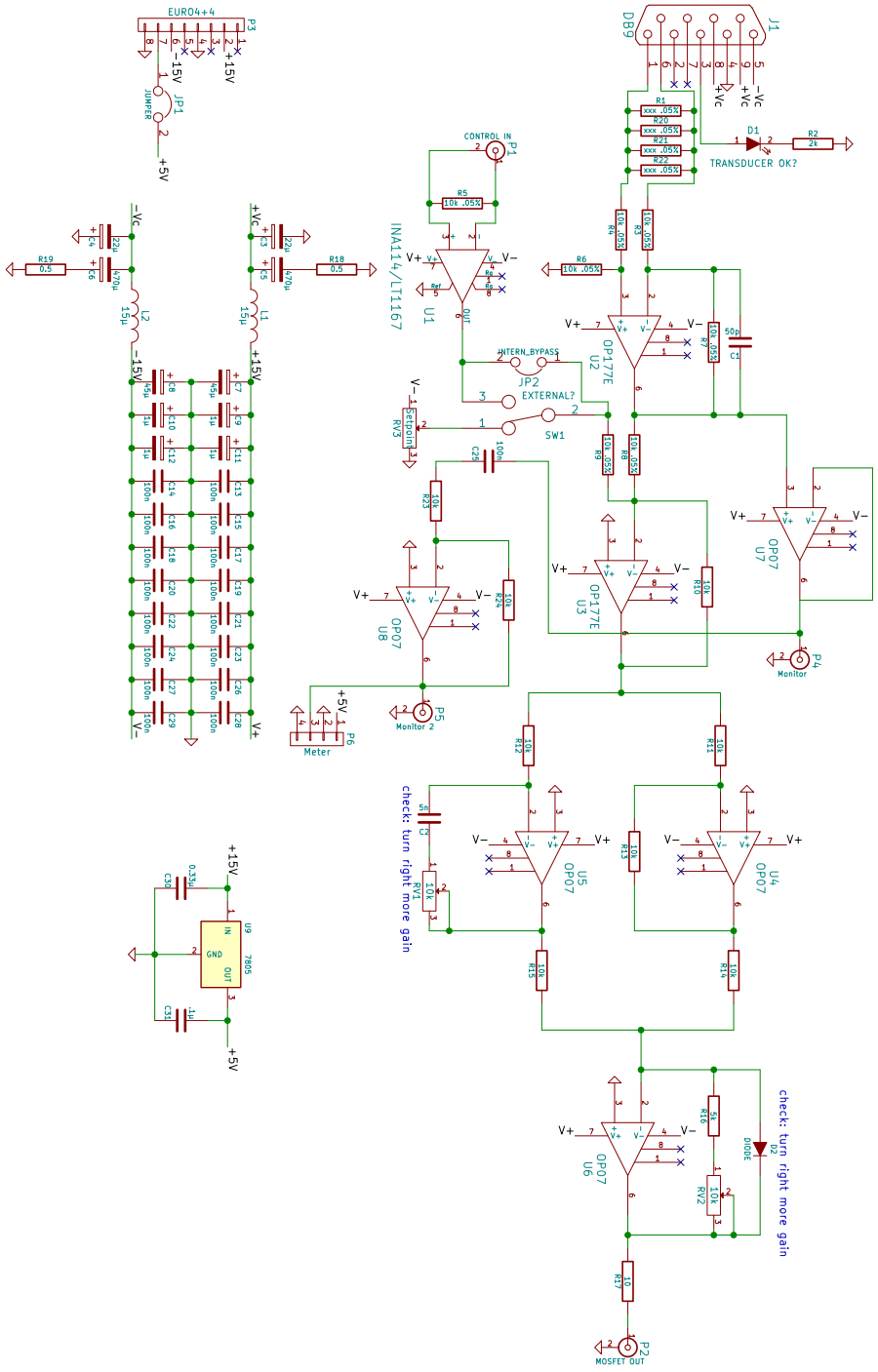

Figure A.2.: Schematic of the high stability battery powered current supply. Design by N. Winter.

Bibliography

[1] S. N. Bose. Plancks Gesetz und Lichtquantenhypothese. *Zeitschrift für Physik*, 26:178–181, 1924.

[2] A. Einstein. Quantentheorie des einatomigen idealen Gases II. *Sitzungsberichte der preussischen Akademie der Wissenschaften*, 1925.

[3] K. B. Davis, M.-O. Mewes, M. R. van Andrews, N. J. Van Druten, D. S. Durfee, D. M. Kurn, and W. Ketterle. Bose-Einstein condensation in a gas of sodium atoms. *Physical Review Letters*, 75(22):3969, 1995.

[4] M. H. Anderson, J. R. Ensher, M. R. Matthews, C. E. Wieman, and E. A. Cornell. Observation of Bose-Einstein condensation in a dilute atomic vapor. *Science*, 269(5221):198–201, 1995.

[5] H. Feshbach. Unified theory of nuclear reactions. *Annals of Physics*, 5(4): 357–390, 1958.

[6] S. Inouye, M. R. Andrews, J. Stenger, H.-J. Miesner, D. M. Stamper-Kurn, and W. Ketterle. Observation of Feshbach resonances in a Bose-Einstein condensate. *Nature*, 392(6672):151–154, 1998.

[7] L. D. Carr, D. DeMille, R. V. Krems, and J. Ye. Cold and ultracold molecules: science, technology and applications. *New Journal of Physics*, 11(5):055049, 2009.

[8] J. Catani, G. Lamporesi, D. Naik, M. Gring, M. Inguscio, F. Minardi, A. Kantian, and T. Giamarchi. Quantum dynamics of impurities in a one-dimensional Bose gas. *Physical Review A*, 85(2):023623, 2012.

[9] A. P. Chikkatur, A. Görlitz, D. M. Stamper-Kurn, S. Inouye, S. Gupta, and W. Ketterle. Suppression and enhancement of impurity scattering in a Bose-Einstein condensate. *Physical Review Letters*, 85(3):483–486, 2000.

[10] N. Spethmann, F. Kindermann, S. John, C. Weber, D. Meschede, and A. Widera. Dynamics of Single Neutral Impurity Atoms Immersed in an Ultracold Gas. *Physical Review Letters*, 109(23):235301, 2012.

[11] R. Scelle, T. Rentrop, A. Trautmann, T. Schuster, and M. K. Oberthaler. Motional Coherence of Fermions Immersed in a Bose Gas. *Physical Review Letters*, 111(7):070401, 2013.

[12] D. Schlippert, J. Hartwig, H. Albers, L. L. Richardson, C. Schubert, A. Roura, W. P. Schleich, W. Ertmer, and E. M. Rasel. Quantum Test of the Universality of Free Fall. *Physical Review Letters*, 112(20):203002, 2014.

[13] N. T. Zinner and A. S. Jensen. Comparing and contrasting nuclei and cold atomic gases. *Journal of Physics G: Nuclear and Particle Physics*, 40(5): 053101, 2013.

[14] N. T. Zinner. Few-Body Physics in a Many-Body World. *Few-Body Systems*, 55(8-10):599–604, 2014.

[15] I. Bloch, J. Dalibard, and W. Zwerger. Many-body physics with ultracold gases. *Reviews of Modern Physics*, 80(3):885–964, 2008.

[16] C. Myatt, E. Burt, R. Ghrist, E. Cornell, and C. Wieman. Production of Two Overlapping Bose-Einstein Condensates by Sympathetic Cooling. *Physical Review Letters*, 78(4):586–589, 1997.

[17] H. Schmaljohann, M. Erhard, J. Kronjäger, M. Kottke, S. van Staa, L. Cacciapuoti, J. J. Arlt, K. Bongs, and K. Sengstock. Dynamics of F=2 Spinor Bose-Einstein Condensates. *Physical Review Letters*, 92(4):040402, 2004.

[18] D. M. Stamper-Kurn and M. Ueda. Spinor Bose gases: Symmetries, magnetism, and quantum dynamics. *Reviews of Modern Physics*, 85(3):1191–1244, 2013.

[19] S. Papp, J. Pino, and C. Wieman. Tunable Miscibility in a Dual-Species Bose-Einstein Condensate. *Physical Review Letters*, 101(4):040402, 2008.

[20] S. Sugawa, R. Yamazaki, S. Taie, and Y. Takahashi. Bose-Einstein condensate in gases of rare atomic species. *Physical Review A*, 84(1):011610, 2011.

[21] K.-K. Ni, S. Ospelkaus, M. H. G. de Miranda, A. Pe'er, B. Neyenhuis, J. J. Zirbel, S. Kotochigova, P. S. Julienne, D. S. Jin, and J. Ye. A high phase-space-density gas of polar molecules. *Science*, 322(5899):231–5, 2008.

[22] S. Herrmann, H. Dittus, and C. Lämmerzahl. Testing the equivalence principle with atomic interferometry. *Classical and Quantum Gravity*, 29(18):184003, 2012.

[23] Miroslav Gajdacz, Tomáš Opatrný, and Kunal K. Das. An atomtronics transistor for quantum gates. *Physics Letters A*, 378(28-29):1919–1924, 2014.

[24] B. DeMarco and D.S. Jin. Onset of Fermi Degeneracy in a Trapped Atomic Gas. *Science*, 285(5434):1703–1706, 1999.

[25] G. Modugno, G. Ferrari, G. Roati, R. J. Brecha, A. Simoni, and M. Inguscio. Bose-Einstein condensation of potassium atoms by sympathetic cooling. *Science*, 294(5545):1320–1322, 2001.

[26] G. Modugno, M. Modugno, F. Riboli, G. Roati, and M. Inguscio. Two Atomic Species Superfluid. *Physical Review Letters*, 89(19):190404, 2002.

[27] G. Thalhammer, G. Barontini, L. De Sarlo, J. Catani, F. Minardi, and M. Inguscio. Double species Bose-Einstein condensate with tunable interspecies interactions. *Physical Review Letters*, 100(21):210402, 2008.

[28] D. J. McCarron, H. W. Cho, D. L. Jenkin, M. P. Köppinger, and S. L. Cornish. Dual-species Bose-Einstein condensate of ^{87}Rb and ^{133}Cs. *Physical Review A*, 84(1):11603, 2011.

[29] A. D. Lercher, T. Takekoshi, M. Debatin, B. Schuster, R. Rameshan, F. Ferlaino, R. Grimm, and H. C. Nägerl. Production of a dual-species Bose-Einstein condensate of Rb and Cs atoms. *The European Physical Journal D*, 65(1-2): 3–9, 2011.

[30] D. Xiong, X. Li, F. Wang, and D. Wang. A ^{23}Na and ^{87}Rb double Bose-Einstein condensate with tunable interactions. *arXiv preprint 1305.7091*, 2013.

[31] B. Pasquiou, A. Bayerle, S. M. Tzanova, S. Stellmer, J. Szczepkowski, M. Parigger, R. Grimm, and F. Schreck. Quantum degenerate mixtures of strontium and rubidium atoms. *Physical Review A*, 88(2):23601, 2013.

[32] E. Braaten and H. W. Hammer. Universality in few-body systems with large scattering length. *Physics Reports*, 428(5-6):259–390, 2006.

[33] C. Ospelkaus, S. Ospelkaus, L. Humbert, P. Ernst, K. Sengstock, and K. Bongs. Ultracold Heteronuclear Molecules in a 3D Optical Lattice. *Physical Review Letters*, 97(12):120402, 2006.

[34] V. Efimov. Energy levels arising from resonant two-body forces in a three-body system. *Physics Letters B*, 33(8):563–564, 1970.

[35] T. Kraemer, M. Mark, P. Waldburger, J. G. Danzl, C. Chin, B. Engeser, A. D. Lange, K. Pilch, A. Jaakkola, H.-C. Nägerl, and R. Grimm. Evidence for Efimov quantum states in an ultracold gas of caesium atoms. *Nature*, 440 (7082):315–318, 2006.

[36] S. Knoop, F. Ferlaino, M. Mark, M. Berninger, H. Schoebel, H. C. Naegerl, and R. Grimm. Observation of an Efimov-like resonance in ultracold atom-dimer scattering. *Nature Physics*, 5:227–230, 2009.

[37] N. Gross, Z. Shotan, S. Kokkelmans, and L. Khaykovich. Observation of universality in ultracold ^{7}Li three-body recombination. *Physical Review Letters*, 103(16):163202, 2009.

[38] G. Barontini, C. Weber, F. Rabatti, J. Catani, G. Thalhammer, M. Inguscio, and F. Minardi. Observation of Heteronuclear Atomic Efimov Resonances. *Physical Review Letters*, 103(4):043201, 2009.

[39] T. B. Ottenstein, T. Lompe, M. Kohnen, A. N. Wenz, and S. Jochim. Collisional Stability of a Three-Component Degenerate Fermi Gas. *Physical Review Letters*, 101(20):203202, 2008.

[40] J. H. Huckans, J. R. Williams, E. L. Hazlett, R. W. Stites, and K. M. O'Hara. Three-Body Recombination in a Three-State Fermi Gas with Widely Tunable Interactions. *Physical Review Letters*, 102(16):165302, 2009.

[41] J. R. Williams, E. L. Hazlett, J. H. Huckans, R. W. Stites, Y. Zhang, and K. M. O'Hara. Evidence for an Excited-State Efimov Trimer in a Three-Component Fermi Gas. *Physical Review Letters*, 103(13):130404, 2009.

[42] A. N. Wenz, T. Lompe, T. B. Ottenstein, F. Serwane, G. Zürn, and S. Jochim. Universal trimer in a three-component Fermi gas. *Physical Review A*, 80(4): 040702, 2009.

[43] T. Lompe, T. B. Ottenstein, F. Serwane, K. Viering, A. N. Wenz, G. Zürn, and S. Jochim. Atom-Dimer Scattering in a Three-Component Fermi Gas. *Physical Review Letters*, 105(10):103201, 2010.

[44] T. Lompe, T. B. Ottenstein, F. Serwane, A. N. Wenz, G. Zurn, and S. Jochim. Radio-Frequency Association of Efimov Trimers. *Science*, 330(6006):940–944, 2010.

[45] S. Nakajima, M. Horikoshi, T. Mukaiyama, P. Naidon, and M. Ueda. Measurement of an Efimov trimer binding energy in a three-component mixture of ^{6}Li. *Physical Review Letters*, 106(14):143201, 2011.

[46] F. Ferlaino, S. Knoop, M. Berninger, W. Harm, J. P. D'Incao, H.-C. Nägerl, and R. Grimm. Evidence for Universal Four-Body States Tied to an Efimov Trimer. *Physical Review Letters*, 102(14):140401, 2009.

[47] S. E. Pollack, D. Dries, and R. G. Hulet. Universality in three- and four-body bound states of ultracold atoms. *Science*, 326(5960):1683–1685, 2009.

[48] A. Zenesini, B. Huang, M. Berninger, S. Besler, H. C. Nägerl, F. Ferlaino, R. Grimm, C. H. Greene, and J. Von Stecher. Resonant five-body recombination in an ultracold gas of bosonic atoms. *New Journal of Physics*, 15(4): 043040, 2013.

[49] M. Zaccanti, B. Deissler, C. D'Errico, M. Fattori, M. Jona-Lasinio, S. Müller, G. Roati, M. Inguscio, and G. Modugno. Observation of an Efimov spectrum in an atomic system. *Nature Physics*, 5(8):586–591, 2009.

[50] B. Huang, L. A. Sidorenkov, R. Grimm, and J. M. Hutson. Observation of the Second Triatomic Resonance in Efimov's Scenario. *Physical Review Letters*, 112(19):190401, 2014.

[51] R. Pires, J. Ulmanis, S. Häfner, M. Repp, A. Arias, E. D. Kuhnle, and M. Weidemüller. Observation of Efimov Resonances in a Mixture with Extreme Mass Imbalance. *Physical Review Letters*, 112(25):250404, 2014.

[52] S.-K. Tung, K. Jiménez-García, J. Johansen, C. V. Parker, and C. Chin. Geometric Scaling of Efimov States in a ^{6}Li $-^{133}$ Cs Mixture. *Physical Review Letters*, 113(24):240402, 2014.

[53] C. Chin. Universal scaling of Efimov resonance positions in cold atom systems. *arXiv preprint 1111.1484*, (1):1–4, 2011.

[54] M. Berninger, A. Zenesini, B. Huang, W. Harm, H.-C. Nägerl, F. Ferlaino, R. Grimm, P. S. Julienne, and J. M. Hutson. Universality of the Three-Body Parameter for Efimov States in Ultracold Cesium. *Physical Review Letters*, 107(12):120401, 2011.

[55] S. Roy, M. Landini, A. Trenkwalder, G. Semeghini, G. Spagnolli, A. Simoni, M. Fattori, M. Inguscio, and G. Modugno. Test of the Universality of the Three-Body Efimov Parameter at Narrow Feshbach Resonances. *Physical Review Letters*, 111(5):053202, 2013.

[56] R. S. Bloom, M. G. Hu, T. D. Cumby, and D. S. Jin. Tests of Universal Three-Body Physics in an Ultracold Bose-Fermi Mixture. *Physical Review Letters*, 111(10):105301, 2013.

[57] M. G. Hu, R. S. Bloom, D. S. Jin, and J. M. Goldwin. Avalanche-mechanism loss at an atom-molecule Efimov resonance. *Physical Review A*, 90(1):013619, 2014.

[58] M. Fox. *Quantum Optics*. Oxford University Press, 2007. ISBN 978-0-19-856673-1.

[59] C. Gerry and P. Knight. *Introductory quantum optics*. Cambridge university press, 2005. ISBN 0-521-52735-x.

[60] J. Dalibard and C. Cohen-Tannoudji. Dressed-atom approach to atomic motion in laser light: the dipole force revisited. *Journal of the Optical Society of America B*, 2(11):1707, 1985.

[61] L. Allen and J.H. Eberly. *Optical Resonance and Two-Level Atoms.* Dover publications, 1975.

[62] H. J. Metcalf and P. der Straten. *Laser cooling and trapping*. Springer Verlag, 1999. ISBN 978-1-4612-1470-0.

[63] G. Kleine Büning, J. Will, W. Ertmer, E. Rasel, Jan Arlt, C. Klempt, F. Ramirez-Martinez, F. Piéchon, and P. Rosenbusch. Extended coherence time on the clock transition of optically trapped Rubidium. *Physical Review Letters*, 106(24):240801, 2011.

[64] M. Kasevich and S. Chu. Measurement of the gravitational acceleration of an atom with a light-pulse atom interferometer. *Applied Physics B Photophysics and Laser Chemistry*, 54(5):321–332, 1992.

[65] A. Peters, K.Y. Chung, and S. Chu. Measurement of gravitational acceleration by dropping atoms. *Nature*, 400:849–852, 1999.

[66] M. Takamoto, F.-L. Hong, R. Higashi, and H. Katori. An optical lattice clock. *Nature*, 435(7040):321–324, 2005.

[67] S. Kuhr, S. Gleyzes, C. Guerlin, J. Bernu, S. Deléglise, U. B. Hoff, M. Brune, J. M. Raimona, and S. Haroche. Quantum jumps of light recording the birth and death of a photon in a cavity. In *Conference on Lasers and Electro-Optics Europe - Technical Digest*, 2007. ISBN 1424409306.

[68] M. Brune, E. Hagley, J. Dreyer, X. Maître, A. Maali, C. Wunderlich, J. Raimond, and S. Haroche. Observing the Progressive Decoherence of the "Meter" in a Quantum Measurement. *Physical Review Letters*, 77(24):4887–4890, 1996.

[69] T. Mayer-Kuckuk. *Atomphysik*. B. G. Teubner, 1985. ISBN 3-519-23042-9.

[70] T. G. Tiecke. Properties of potassium. *Physics Department Harvard University*, 2011.

[71] D. A. Steck. Rubidium 87 D line data. Technical report, Los Alamos National Loratory, 2010.

[72] W. Nolting. *Grundkurs Theoretische Physik 5 Quantenmechanik: Teil 2: Methoden und Anwendungen.* Springer Fachverlag, 6 edition, 2006. ISBN 3-540-26035-8.

[73] Eric Braaten and H.-W. Hammer. Efimov physics in cold atoms. *Annals of Physics*, 322(1):120–163, 2007.

[74] Michael Fowler. More Scattering: the Partial Wave Expansion, 2008.

[75] Stephen Gasiorowicz. *Quantenphysik*. Oldenbourg, 4 edition, 1987.

[76] J. E. Jones. On the Determination of Molecular Fields. II. From the Equation of State of a Gas. *Proceedings of the Royal Society A: Mathematical, Physical and Engineering Sciences*, 106(738):463–477, 1924.

[77] A. Simoni, M. Zaccanti, C. D'Errico, M. Fattori, G. Roati, M. Inguscio, G. Modugno, C. D'Errico, M. Fattori, G. Roati, M. Inguscio, and G. Modugno. Near-threshold model for ultracold KRb dimers from interisotope Feshbach spectroscopy. *Physical Review A*, 77(5):052705, 2008.

[78] E. G. M. van Kempen, S. J. J. M. F. Kokkelmans, D. J. Heinzen, and B. J. Verhaar. Interisotope determination of ultracold rubidium interactions from three high-precision experiments. *Physical Review Letters*, 88(9):093201, 2002.

[79] C. Chin, R. Grimm, P. Julienne, and E. Tiesinga. Feshbach resonances in ultracold gases. *Rev. Mod. Phys.*, 82(2):1225–1286, 2010.

[80] A. J. Moerdijk, B. J. Verhaar, and A. Axelsson. Resonances in ultracold collisions of ^{6}Li, ^{7}Li, and ^{23}Na. *Physical Review A*, 51(6):4852–4861, 1995.

[81] E. A. Donley, N. R. Claussen, S. T. Thompson, and C. E. Wieman. Atom-molecule coherence in a Bose-Einstein condensate. *Nature*, 417(6888):529–533, 2002.

[82] J. Herbig, T. Kraemer, M. Mark, T. Weber, C. Chin, H.-C. Nägerl, and R. Grimm. Preparation of a pure molecular quantum gas. *Science*, 301(5639): 1510–1513, 2003.

[83] C. Weber, G. Barontini, J. Catani, G. Thalhammer, M. Inguscio, and F. Minardi. Association of ultracold double-species bosonic molecules. *Physical Review A*, 78(6):061601, 2008.

[84] C. Klempt, T. Henninger, O. Topic, M. Scherer, L. Kattner, E. Tiemann, W. Ertmer, and J. Arlt. Radio-frequency association of heteronuclear Feshbach molecules. *Physical Review A*, 78(6):061602, 2008.

[85] S. Stellmer, B. Pasquiou, R. Grimm, and F. Schreck. Creation of ultracold Sr_2 molecules in the electronic ground state. *Physical Review Letters*, 109 (11):115302, 2012.

[86] E. Kuznetsova, M. Gacesa, P. Pellegrini, S. F. Yelin, and R. Côté. Efficient formation of ground-state ultracold molecules via STIRAP from the continuum at a Feshbach resonance. *New Journal of Physics*, 11(5):055028, 2009.

[87] G. F. Gribakin and V. V. Flambaum. Calculation of the scattering length in atomic collisions using the semiclassical approximation. *Physical Review A*, 48(1):546–553, 1993.

[88] Martin Stoll and Thorsten Köhler. Production of three-body Efimov molecules in an optical lattice. *Physical Review A*, 72(2):022714, 2005.

[89] T. Köhler, K. Góral, and P. S. Julienne. Production of cold molecules via magnetically tunable Feshbach resonances. *Reviews of Modern Physics*, 78 (4):1311–1361, 2006.

[90] W. Ketterle, D. S. Durfee, and D. M. Stamper-Kurn. Making, probing and understanding Bose-Einstein condensates. *Proceedings of the 1998 Enrico Fermi summer school on Bose-Einstein condensation in Varenna, Italy*, 5: 1–87, 1999.

[91] T. Weber, J. Herbig, M. Mark, H.C. Nägerl, and R. Grimm. Three-Body Recombination at Large Scattering Lengths in an Ultracold Atomic Gas. *Physical Review Letters*, 91(12):123201, 2003.

[92] E. Nielsen. The three-body problem with short-range interactions. *Physics Reports*, 347(5):373–459, 2001.

[93] L.M. Delves. Tertiary and general-order collisions (II). *Nuclear Physics*, 20: 275–308, 1960.

[94] P. K. Sø rensen, D. V. Fedorov, and A. S. Jensen. Three-Body Recombination Rates Near a Feshbach Resonance within a Two-Channel Contact Interaction Model. *Few-Body Systems*, 54(5-6):579–590, 2013.

[95] J. Macek. Loosely bound states of three particles. *Zeitschrift für Physik D Atoms, Molecules and Clusters*, 3(1):31–37, 1986.

[96] D. V. Fedorov and A. S. Jensen. Regularization of a three-body problem with zero-range potentials. *Journal of Physics A: Mathematical and General*, 34(30):6003–6012, 2001.

[97] K. Helfrich, H.-W. Hammer, and D. S. Petrov. Three-body problem in heteronuclear mixtures with resonant interspecies interaction. *Physical Review A*, 81(4):042715, 2010.

[98] A. S. Jensen and D. V. Fedorov. Efimov states in asymmetric systems. *Europhysics Letters*, 62(3):7, 2003.

[99] M. Mikkelsen, A. S. Jensen, D. V. Fedorov, and N. T. Zinner. Three-body recombination of two-component cold atomic gases into deep dimers in an optical model. *Journal of Physics B*, 48(8):085301, 2015.

[100] C. J. Pethick and H. Smith. *Bose-Einstein condensation in dilute gases*. Cambridge university press, 2nd edition, 2008. ISBN 978-0-521-84651-6.

[101] F. Dalfovo, S. Giorgini, L. P. Pitaevskii, and S. Stringari. Theory of Bose-Einstein condensation in trapped gases. *Reviews of Modern Physics*, 71(3): 463–512, 1999.

[102] N. N. Bogoliubov. On the Theory of Superfluidity. *Journal of Physics*, 11(1): 23–32., 1947.

[103] W. Ketterle and N.J. Van Druten. Evaporative Cooling of Trapped Atoms. *Advances In Atomic, Molecular, and Optical Physics*, 37(C):181–236, 1996.

[104] T.-L. Ho and V. Shenoy. Binary Mixtures of Bose Condensates of Alkali Atoms. *Physical Review Letters*, 77(16):3276–3279, 1996.

[105] R. W. Pattinson, T. P. Billam, S. A. Gardiner, D. J. McCarron, H. W. Cho, S. L. Cornish, N. G. Parker, and N. P. Proukakis. Equilibrium solutions for immiscible two-species Bose-Einstein condensates in perturbed harmonic traps. *Physical Review A*, 87(1):013625, 2013.

[106] F. Riboli and M. Modugno. Topology of the ground state of two interacting Bose-Einstein condensates. *Physical Review A*, 65(6):063614, 2002.

[107] D. M. Jezek and P. Capuzzi. Interaction-driven effects on two-component Bose-Einstein condensates. *Physical Review A*, 66(015602):4, 2002.

[108] S. Falke, H. Knöckel, J. Friebe, M. Riedmann, E. Tiemann, and C. Lisdat. Potassium ground-state scattering parameters and Born-Oppenheimer potentials from molecular spectroscopy. *Physical Review A*, 78(1):012503, 2008.

[109] J. Will. *Symmetrieabhängige Frequenzverschiebungen in Atomuhren*. PhD thesis, University of Hanover, 2012.

[110] N. Winter. *Creation of* ^{39}K *Bose-Einstein condensates with tunable interaction*. Phd thesis, Aarhus University, 2013.

[111] G. Kleine-Büning. *Lange Kohärenzzeit optisch gefangener Ensembles*. PhD thesis, University of Hannover, 2011.

[112] W. Ketterle, K. B. Davis, M. A. Joffe, A. Martin, and D. E. Pritchard. High densities of cold atoms in a dark spontaneous-force optical trap. *Physical Review Letters*, 70(15):2253–2256, 1993.

[113] C. Klempt, T. van Zoest, T. Henninger, O. Topic, E. Rasel, W. Ertmer, and J. Arlt. Ultraviolet light-induced atom desorption for large rubidium and potassium magneto-optical traps. *Physical Review A*, 73(1):13410, 2006.

[114] L. Wacker, N. B. Jø rgensen, D. Birkmose, R. Horchani, W. Ertmer, C. Klempt, N. Winter, J. Sherson, and J. J. Arlt. Tunable dual-species Bose-Einstein condensates of ^{39}K and ^{87}Rb. *arXiv preprint 1505.07975*, 2015.

[115] K. Aikawa, J. Kobayashi, K. Oasa, T. Kishimoto, M. Ueda, and S. Inouye. Narrow-linewidth light source for a coherent Raman transfer of ultracold molecules. *Optics express*, 19(15):14479–86, 2011.

[116] X. Baillard, A. Gauguet, S. Bize, P. Lemonde, Ph Laurent, A. Clairon, and P. Rosenbusch. Interference-filter-stabilized external-cavity diode lasers. *Optics Communications*, 266(2):609–613, 2006.

[117] O. Schmidt, K. M. Knaak, R. Wynands, and D. Meschede. Cesium saturation spectroscopy revisited: How to reverse peaks and observe narrow resonances. *Applied Physics B Lasers and Optics*, 59(2):167–178, 1994.

[118] U. Schunemann, H. Engler, R. Grimm, M. Weidemuller, and M. Zielonkowski. Simple scheme for tunable frequency offset locking of two lasers. *Review Of Scientific Instruments*, 70(1):242–243, 1999.

[119] J. N. Walpole. Semiconductor amplifiers and lasers with tapered gain regions. *Optical and Quantum Electronics*, 28(6):623–645, 1996.

[120] B. Lücke. Aufbau und Planung einer Hybridfalle zur Erzeugung ultrakalter Quantengase. Diplomarbeit, University of Hannover, 2009.

[121] T. Kishimoto, J. Kobayashi, K. Noda, K. Aikawa, M. Ueda, and S. Inouye. Direct evaporative cooling of ^{41}K into a Bose-Einstein condensate. *Physical Review A*, 79(3):031602, 2009.

[122] M. Landini, S. Roy, L. Carcagni, D. Trypogeorgos, M. Fattori, M. Inguscio, and G. Modugno. Sub-Doppler laser cooling of potassium atoms. *Physical Review A*, 84(4):43432, 2011.

[123] V. Gokhroo, G. Rajalakshmi, R. K. Easwaran, and C. S. Unnikrishnan. Sub-Doppler deep-cooled bosonic and fermionic isotopes of potassium in a compact 2D+–3D MOT set-up. *Journal of Physics B*, 44(11):115307, 2011.

[124] M. Landini, S. Roy, G. Roati, A. Simoni, M. Inguscio, Gi. Modugno, and M. Fattori. Direct evaporative cooling of ^{39} K atoms to Bose-Einstein condensation. *Physical Review A*, 86(3):033421, 2012.

[125] L. G. Marcassa, G. D. Telles, S. R. Muniz, and V. S. Bagnato. Collisional losses in a K-Rb cold mixture. *Physical Review A*, 63(1):13413, 2000.

[126] S. Dutta, A. Altaf, J. Lorenz, D. S. Elliott, and Y. P. Chen. Interspecies collision-induced losses in a dual species ^{7} Li– ^{85} Rb magneto-optical trap. *Journal of Physics B*, 47(10):105301, 2014.

[127] M. H. Anderson, W. Petrich, J. R. Ensher, and E. A. Cornell. Reduction of light-assisted collisional loss rate from a low-pressure vapor-cell trap. *Physical Review A*, 50(5):R3597–R3600, 1994.

[128] C. G. Townsend, N. H. Edwards, K. P. Zetie, C. J. Cooper, J. Rink, and C. J. Foot. High-density trapping of cesium atoms in a dark magneto-optical trap. *Physical Review A*, 53(3):1702–1714, 1996.

[129] N. Radwell, G. Walker, and S. Franke-Arnold. Cold-atom densities of more than $10^{12}cm^{-3}$ in a holographically shaped dark spontaneous-force optical trap. *Physical Review A*, 88(4):43409, 2013.

[130] T. Esslinger, I. Bloch, and T. W. Hänsch. Bose-Einstein condensation in a quadrupole-Ioffe-configuration trap. *Physical Review A*, 58(4):R2664, 1998.

[131] D. M. Brink and C. V. Sukumar. Majorana spin-flip transitions in a magnetic trap. *Physical Review A*, 74(3):035401, 2006.

[132] G. Ferrari, M. Inguscio, W. Jastrzebski, G. Modugno, G. Roati, and A. Simoni. Collisional properties of ultracold K-Rb mixtures. *Physical Review Letters*, 89(5):053202, 2002.

[133] R. L. D. Campbell, R. P. Smith, N. Tammuz, S. Beattie, S. Moulder, and Z. Hadzibabic. Efficient Production of Large ^{39}K Bose-Einstein Condensates. *Physical Review A*, 82(6):7, 2010.

[134] G. Kleine Büning, J. Will, W. Ertmer, C. Klempt, and J. Arlt. A slow gravity compensated atom laser. *Applied Physics B*, 100(1):117–123, 2010.

[135] Y.-J. J. Lin, A. R. Perry, R. L. Compton, I. B. Spielman, and J. V. Porto. Rapid production of ^{87}Rb Bose-Einstein condensates in a combined magnetic and optical potential. *Physical Review A*, 79(6):063631, 2009.

[136] M. Haas, V. Leung, D. Frese, D. Haubrich, S. John, C. Weber, A. Rauschenbeutel, and D. Meschede. Species-selective microwave cooling of a mixture of rubidium and caesium atoms. *New Journal of Physics*, 9(5):147–147, 2007.

[137] D. Xiong, P. Wang, H. Chen, and J. Zhang. Evaporative cooling rubidium atoms with microwave radiation. *Chinese Optics Letters*, 8(4):351–353, 2010.

[138] P.-J. Wang, D.-Z. Xiong, Z.-K. Fu, and J. Zhang. K atoms with microwave and radio frequency radiation. *Chinese Physics B*, 20(1):016701, 2011.

[139] H. P. Mishra, A. S. Flores, W. Vassen, and S. Knoop. Efficient production of an ^{87}Rb $F = 2$, $m_F = 2$ Bose-Einstein condensate in a hybrid trap. *The European Physical Journal D*, 69(2):52, 2015.

[140] C. Silber, S. Günther, C. Marzok, B. Deh, Ph W. Courteille, and C. Zimmermann. Quantum-Degenerate Mixture of Fermionic Lithium and Bosonic Rubidium Gases. *Physical Review Letters*, 95(17):170408, 2005.

[141] C. Marzok, B. Deh, Ph. W. Courteille, and C. Zimmermann. Ultracold Thermalization of ^{7}Li and ^{87}Rb. *Physical Review A*, 76(5):052704, 2007.

[142] M. Taglieber, A. C. Voigt, T. Aoki, T. W. Hänsch, and K. Dieckmann. Quantum degenerate two-species fermi-fermi mixture coexisting with a Bose-Einstein condensate. *Physical Review Letters*, 100(1):10401, 2008.

[143] Z. Hadzibabic, S. Gupta, C. A. Stan, C. H. Schunck, M. W. Zwierlein, K. Dieckmann, and W. Ketterle. Fiftyfold improvement in the number of quantum degenerate fermionic atoms. *Physical Review Letters*, 91(16):160401, 2003.

[144] G. Reinaudi, T. Lahaye, Z. Wang, and D. Guéry-Odelin. Strong saturation absorption imaging of dense clouds of ultracold atoms. *Optics letters*, 32(21): 3143–3145, 2007.

[145] R. Grimm, M. Weidemüller, and Y. B. Ovchinnikov. Optical dipole traps for neutral atoms. *Advances in atomic, molecular, and optical physics*, 42: 95–170, 2000.

[146] C. D'Errico, M. Zaccanti, M. Fattori, G. Roati, M. Inguscio, G. Modugno, and A. Simoni. Feshbach resonances in ultracold ^{39}K. *New Journal of Physics*, 9(7):223–223, 2007.

[147] G. Barontini, C. Weber, F. Rabatti, J. Catani, G. Thalhammer, M. Inguscio, and F. Minardi. Observation of Heteronuclear Atomic Efimov Resonances. *Physical Review Letters*, 103(4):043201, 2009.

[148] M. Mudrich, S. Kraft, K. Singer, R. Grimm, A. Mosk, and M. Weidemüller. Sympathetic cooling with two atomic species in an optical trap. *Physical Review Letters*, 88(25 Pt 1):253001, 2002.

[149] M. Anderlini and D. Guéry-Odelin. Thermalization in mixtures of ultracold gases. *Physical Review A*, 73(3):032706, 2006.

[150] G. Thalhammer, G. Barontini, J. Catani, F. Rabatti, C. Weber, A. Simoni, F. Minardi, and M. Inguscio. Collisional and molecular spectroscopy in an ultracold Bose–Bose mixture. *New Journal of Physics*, 11(5):055044, 2009.

[151] C. Ticknor, C. A. Regal, D. S. Jin, and J. L. Bohn. Multiplet structure of Feshbach resonances in nonzero partial waves. *Physical Review A*, 69(4): 042712, 2004.

[152] S. Tojo, Y. Taguchi, Y. Masuyama, T. Hayashi, H. Saito, and T. Hirano. Controlling phase separation of binary Bose-Einstein condensates via mixed-spin-channel Feshbach resonance. *Physical Review A*, 82(3):33609, 2010.

[153] E. Nicklas, H. Strobel, T. Zibold, C. Gross, B. a. Malomed, P. G. Kevrekidis, and M. K. Oberthaler. Rabi Flopping Induces Spatial Demixing Dynamics. *Physical Review Letters*, 107(19):193001, 2011.

[154] S. Ospelkaus, C. Ospelkaus, L. Humbert, K. Sengstock, and K. Bongs. Tuning of Heteronuclear Interactions in a Degenerate Fermi-Bose Mixture. *Physical Review Letters*, 97(12):120403, 2006.

[155] M. Zaccanti, C. D'Errico, F. Ferlaino, G. Roati, M. Inguscio, and G. Modugno. Control of the interaction in a Fermi-Bose mixture. *Physical Review A*, 74 (4):5, 2006.

[156] M. J. Edmonds, K. L. Lee, and N. P. Proukakis. Kinetic model of trapped finite-temperature binary condensates. *Physical Review A*, 91(1):011602, 2015.

[157] L. Wacker, N. B. Jørgensen, M. Mikkelsen, D. Birkmose, N. Winter, E. Tiemann, J. Sherson, N .T. Zinner, and J. J. Arlt. Absence of observable Efimov resonances in ultra-cold KRb mixtures. *in preparation*, 2015.

[158] J. P. D'Incao, H. Suno, and B. D. Esry. Limits on Universality in Ultracold Three-Boson Recombination. *Physical Review Letters*, 93(12):123201, 2004.

[159] Yujun Wang, Jia Wang, J. P. D'Incao, and Chris H. Greene. Universal Three-Body Parameter in Heteronuclear Atomic Systems. *Physical Review Letters*, 109(24):243201, 2012.

[160] A. Marte, T. Volz, J. Schuster, S. Dürr, G. Rempe, E. van Kempen, and B. Verhaar. Feshbach Resonances in Rubidium 87: Precision Measurement and Analysis. *Physical Review Letters*, 89(28):283202, 2002.

[161] E. Tiemann. . *private communication*, 2015.

[162] O. Machtey, D. A. Kessler, and L. Khaykovich. Universal Dimer in a Collisionally Opaque Medium: Experimental Observables and Efimov Resonances. *Physical Review Letters*, 108(13):130403, 2012.

[163] Matthias Weidemüller. to be published. *private communication*, 2015.

[164] Kohei Kato. Study of ultracold heteronuclear Feshbach molecules. *PhD Thesis, The University of Tokyo*, 2015.

[165] O. Machtey, Z. Shotan, N. Gross, and L. Khaykovich. Association of Efimov Trimers from a Three-Atom Continuum. *Physical Review Letters*, 108(21): 210406, 2012.

[166] T. V. Tscherbul and S. T. Rittenhouse. Three-body radio-frequency association of Efimov trimers. *Physical Review A*, 84(6):062706, 2011.

[167] Z. Shotan, O. Machtey, S. Kokkelmans, and L. Khaykovich. Three-Body Recombination at Vanishing Scattering Lengths in an Ultracold Bose Gas. *Physical Review Letters*, 113(5):053202, 2014.

[168] R. J. Fletcher, A. L. Gaunt, N. Navon, R. P. Smith, and Z. Hadzibabic. Stability of a Unitary Bose Gas. *Physical Review Letters*, 111(12):125303, 2013.

[169] P. Makotyn, C. E. Klauss, D. L. Goldberger, E. A. Cornell, and D. S. Jin. Universal dynamics of a degenerate unitary Bose gas. *Nature Physics*, 10(2): 116–119, 2014.

[170] M. J. Edmonds, K. L. Lee, and N. P. Proukakis. A Non-Equilibrium Kinetic Theory for Trapped Binary Condensates. *arXiv preprint 1507.05078*, 2015.

[171] C. Ospelkaus and S. Ospelkaus. Heteronuclear quantum gas mixtures. *Journal of Physics B*, 41(20):203001, 2008.

[172] A. Chotia, B. Neyenhuis, S. a. Moses, B. Yan, J. P. Covey, M. Foss-Feig, A. M. Rey, D. S. Jin, and J. Ye. Long-Lived Dipolar Molecules and Feshbach Molecules in a 3D Optical Lattice. *Physical Review Letters*, 2012.

[173] K. Góral, L. Santos, and M. Lewenstein. Quantum phases of dipolar bosons in optical lattices. *Physical Review Letters*, 88(17):170406, 2002.

[174] C. Kohstall, M. Zaccanti, M. Jag, A. Trenkwalder, P. Massignan, G. M. Bruun, F. Schreck, and R. Grimm. Metastability and coherence of repulsive polarons in a strongly interacting Fermi mixture. *Nature*, 485(7400):615–8, 2012.

[175] M. Koschorreck, D. Pertot, E. Vogt, B. Fröhlich, M. Feld, and M. Köhl. Attractive and repulsive Fermi polarons in two dimensions. *Nature*, 485 (7400):619–22, 2012.

[176] S. P. Rath and R. Schmidt. Field-theoretical study of the Bose polaron. *Physical Review A*, 88(5):053632, 2013.

[177] R. Søgaard Christensen, J. Levinsen, and G. M. Bruun. Quasiparticle properties of a mobile impurity in a Bose-Einstein condensate. *arXiv preprint 1503.06979*, 2015.

[178] J. Levinsen, P. Massignan, and M. M. Parish. Efimov trimers under strong confinement. *Physical Review X*, 4(3):8, 2014.

List of Figures

List of Tables